Precision Microwave Spectroscopy of the Positronium $n = 2$ Fine Structure

Lokesh Gurung

A dissertation submitted in partial fulfillment
of the requirements for the degree of
Doctor of Philosophy
of
University College London.

Department of Physics and Astronomy
University College London

March 2021

I, Lokesh Gurung, confirm that the work presented in this thesis is my own. Where information has been derived from other sources, I confirm that this has been indicated in the work.

Nomenclature

Acronyms

BEC	Bose-Einstein Condensate.
FOSOF	Field Offset Separated Oscillatory Fields.
FWHM	Full Width at Half Maximum.
HFS	Hyperfine Structure.
HV	High Voltage.
IR	Infrared.
LYSO	Lutetium Yttrium Oxyorthosilicate.
MCP	Micro-Channel Plate.
QED	Quantum ElectroDynamics.
QI	Quantum Interference.
RW	Rotating Wall.
SMA	SubMiniature version A.
SOF	Separated Oscillatory Fields.
SSPALS	Single Shot Positronium Annihilation Lifetime Spectroscopy.
TE	Transverse Electric.
UV	Ultraviolet.

Particles

He	Helium.
H	Hydrogen.

Ps	Positronium.
e^-	Electron.
γ	Photon.
e^+	Positron.

Quantum numbers

J	Total angular momentum.
M_J	Projection of J.
l	Orbital angular momentum.
m_s	Spin projection.
n	Principal.
S	Spin.

Symbols

$\vec{B}$	Magnetic field.
E	Energy.
$\vec{F}$	Electric field.
S_γ	Radiation-induced signal.
Γ_m	Measured linewidth.
Γ_0	Natural linewidth.
λ	Wavelength.
m	Mass.
ν_R	Measured resonance frequency.
ν	Frequency.
q	Fano asymmetry parameter.
τ	Lifetime.
t	Time.

Publications

The results presented in this thesis have been published in the following journal articles:

- L. Gurung, T. J. Babij, S. D. Hogan, and D. B. Cassidy. Precision Microwave Spectroscopy of the Positronium $n = 2$ Fine Structure. *Phys. Rev. Lett.*, 125:073002, 2020
- L. Gurung, T. J. Babij, J. Pérez-Ríos, S. D. Hogan, and D. B. Cassidy. Observation of asymmetric lineshapes in precision microwave spectroscopy of the positronium 2^3S_1-2^3P_j (J=1,2) fine structure intervals. *Phys. Rev. A*, (Accepted)

Other authored publications:

- L. Gurung, T. J. Babij, and D. B. Cassidy. Fast decay of 2^3S_1 positronium atoms in an MgO lined cavity. *EPJ Techniques and Instrumentation*, 8(1):3, 2021
- R. E. Sheldon, T. J. Babij, B. A. Devlin-Hill, L. Gurung, and D. B. Cassidy. Measurement of the annihilation decay rate of 2^3S_1 positronium. *EPL*, 132(1):13001, 2020
- L. Gurung, B. S. Cooper, S. D. Hogan, and D. B. Cassidy. Resonant shifts of positronium energy levels in MgO powder. *Phys. Rev. A*, 101:012701, 2020

- M. H. Rayment, L. Gurung, R. E. Sheldon, S. D. Hogan, and D. B. Cassidy. Multiring electrostatic guide for Rydberg positronium. *Phys. Rev. A*, 100:013410, 2019

- L. Gurung, A. M. Alonso, T. J. Babij, B. S. Cooper, A. L. Shluger, and D. B. Cassidy. Positronium emission from MgO smoke nanocrystals. *Journal of Physics B: Atomic, Molecular and Optical Physics*, 52:105004, 2019

- A. M. Alonso, L. Gurung, B. A. D. Sukra, S. D. Hogan, and D. B. Cassidy. State-selective electric-field ionization of Rydberg positronium. *Phys. Rev. A*, 98:053417, 2018

- B. S. Cooper, J.-P. Boilot, C. Corbel, F. Guillemot, L. Gurung, L. Liszkay, and D. B. Cassidy. Annihilation of positronium atoms confined in mesoporous and macroporous SiO2 films. *Phys. Rev. B*, 97:205302, 2018

- A. M. Alonso, B. S. Cooper, A. Deller, L. Gurung, S. D. Hogan, and D. B. Cassidy. Velocity selection of Rydberg positronium using a curved electrostatic guide. *Phys. Rev. A*, 95:053409, 2017

More information regarding positronium laser physics can be found on:

- https://antimattergravity.com

Acknowledgements

These 4 years of my PhD have been an extraordinary and enjoyable experience of my life, and would have been a lesser experience if it weren't for the support I received from numerous people. Firstly, I am extremely grateful to my supervisor, Prof. David Cassidy, for his mentorship, work ethic, and expertise. I wish to thank him for allowing me this incredible opportunity to carry out research in such an exciting field. I would also like to thank my second supervisor, Prof. Stephen Hogan, for being equally instrumental in my professional development as a scientist and for his collaboration through which I have learnt a lot. I owe him thanks for providing the interference code used in chapter 4.3. I am also grateful to both my supervisors for their invaluable support, both inside and outside of academia.

I am also grateful to the past and present members of our group, especially Dr Ben Cooper, Dr Alberto Alonso, Dr Adam Deller, and Dr Tamara Babij for being patient and taking their time to train me. It has been my privilege to get to know all four and share many fond memories. I wish to thank Mathew Rayment, Benedict Sukra, and Ross Sheldon for the opportunity of working with them. Thank you to John Dumper, Rafid Jawad, and Derek Thomas for their technical support. I acknowledge the office mates I had the pleasure of knowing: Andrea Loreti, Rina Kadokura, Simon Brawley, Don Newson, and Klaudia Gawlas.

I would like to thank my family and friends for their unwavering support and love. My parents, Gupta and Nanu Gurung, have endured much and dedicated themselves to purse a better life for our family, and I dedicate this thesis to them.

The results presented in this thesis were achieved due to the preceding work conducted by previous members in the group. The author of this thesis developed a new microwave guide and spectroscopy system (sections 3.7 and 3.7) and coupled this technique with the previous techniques to probe the Ps fine structure transitions. The existing techniques are outlined in chapters 2 and 3 and were published by the authors in the following articles:

- A. M. Alonso, S. D. Hogan, and D. B. Cassidy. Production of $2\,^3S_1$ positronium atoms by single-photon excitation in an electric field. *Phys. Rev. A*, 95:033408, 2017
- A. M. Alonso, B. S. Cooper, A. Deller, and D. B. Cassidy. Single-shot positron annihilation lifetime spectroscopy with LYSO scintillators. *NIM A*, 828:163 – 169, 2016
- A. M. Alonso, B. S. Cooper, A. Deller, S. D. Hogan, and D. B. Cassidy. Positronium decay from $n = 2$ states in electric and magnetic fields. *Phys. Rev. A*, 93:012506, 2016
- A. M. Alonso, B. S. Cooper, A. Deller, S. D. Hogan, and D. B. Cassidy. Controlling Positronium Annihilation with Electric Fields. *Phys. Rev. Lett.*, 115:183401, 2015
- B. S. Cooper, A. M. Alonso, A. Deller, T. E. Wall, and D. B. Cassidy. A trap-based pulsed positron beam optimised for positronium laser spectroscopy. *Review of Scientific Instruments*, 86:103101, 2015
- A. Deller, B. S. Cooper, T. E. Wall, and D. B. Cassidy. Positronium emission from mesoporous silica studied by laser-enhanced time-of-flight spectroscopy. *New J. Phys.*, 17:043059, 2015

Abstract

A new precision measurement of the positronium (Ps) $2^3S_1 \rightarrow 2^3P_{J=0,1,2}$ fine structure intervals is presented in this thesis. A Surko-type positron trap coupled to a radioactive ^{22}Na source was used to generate intense pulses of positrons to produce slow Ps atoms from a SiO_2 target. These atoms, initially in the ground state, were then optically excited with a UV laser in a region of applied electric field to generate atoms in the 2^3S_1 state. The radiatively metastable atoms then travelled through a microwave guide where $\nu_J = 2^3S_1 \rightarrow 2^3P_J$ ($J = 0,1,2$) transitions were driven with microwave radiation. Atoms in the 2^3P_J states radiatively decay to the 1^3S_1 state and the ν_J transitions were observed via the time-dependent annihilation radiation of the ground state Ps. The ν_0 transition resonance frequency is measured to be ν_0 = 18501.02 $\pm$ 0.62 MHz. This is in disagreement with the theoretical calculation of ν_0 = 18498.25 $\pm$ 0.08 MHz by 2.77 MHz (4.5σ). The ν_1 and ν_2 transition lineshapes are observed to be asymmetric, which prevents the determination of the true resonance frequency. Known quantum interference effects are too small to account for the observed shift and the source of the asymmetry is not presently known. Our measurements, nevertheless, show an improvement in precision compared to previous experiments by a factor of $\approx$ 3-7. These new measurements mark progress in precision Ps physics, and future work to improve precision further and address the current discrepancies are outlined.

Impact Statement

The research presented in this thesis is a step towards advancing spectroscopic measurements of positronium (Ps). Positronium is well described by quantum electrodynamics (QED) and measuring the energy levels of Ps provide a way of testing QED theory. The findings of this thesis highlight an improvement in precision by a factor of 5 compared to previous experiments, and represents a significant progress in the field of Ps spectroscopy in the last 25 years. The techniques and results outlined in this thesis can be improved upon to further advance the field and bring the precision of the experiments to a level comparable with theoretical calculations.

The results presented in this thesis are not in agreement with theoretical calculations. Further investigations and independent experiments are required to find the source of the disagreement. If the disagreement still persists then it could be an indication of contribution from new physics. The standard model of physics predicts that matter and antimatter were created in equal parts when the universe was created. The universe today, however, is dominated by matter. The explanation for the matter-antimatter asymmetry may be understood within the framework of the standard model, but search for new physics beyond the standard model is still being pursued. In order to be sensitive to new particles or new forces, the precision of measurements must be improved.

Contents

Chapter 1

Introduction

1.1 Antimatter: the Positron

In 1928 Paul Dirac put forward his derivation of the quantum theory of electrons [17, 18]. Born out of his formalism were some perplexing negative energy solutions to the relativistic wave-equation which Dirac later branded as 'difficult' and 'unwanted'. Dirac then postulated that these negative energy solutions were a 'sea' of electrons with Pauli's exclusion principle preventing transitions to the occupied states [19]. Also proposed was the idea that an unoccupied negative energy state, a 'hole particle', would be observable as a particle with equal and opposite charge to the electron. Then in 1931 the notion of an anti-electron was theorised [20].

Not long after its prediction Carl Anderson discovered the anti-electron (later named positron) in a cloud chamber study of cosmic rays [21]. In 1934 Stjepan Mohorovičić [22] postulated that the positron and electron can form a bound state called 'electrum', and later John Wheeler [23] coined the term 'polyelectron' for the same atom. This exotic, part matter and part antimatter, atom is bound by the Coulomb interaction and is now commonly known as positronium (Ps) [24]. 17 years after its prediction positronium was eventually discovered by Martin Deutsch in 1951 [25].

1.2 Positronium and its Properties

1.2.1 Positronium: A Hydrogen-like Atom

The two individual spin 1/2 leptonic components of positronium can combine to result in states with total spin $S = 0$ (singlet state), or $S = 1$ (triplet state). The singlet and triplet states of Ps, often referred to as para-positronium (para-Ps) and ortho-positronium (ortho-Ps) respectively, can be represented with the ket notation ($|S, m_s\rangle$) as,

$$|0,0\rangle = \frac{1}{\sqrt{2}}(|\uparrow,\Downarrow\rangle - |\downarrow,\Uparrow\rangle), \tag{1.1}$$

$$|1,1\rangle = |\uparrow,\Uparrow\rangle\,, \tag{1.2}$$

$$|1,0\rangle = \frac{1}{\sqrt{2}}(|\uparrow,\Downarrow\rangle + |\downarrow,\Uparrow\rangle), \tag{1.3}$$

$$|1,-1\rangle = |\downarrow,\Downarrow\rangle\,, \tag{1.4}$$

where m_s indicates the projection of the spin S onto a quantisation axis. The $\uparrow$ and $\Uparrow$ symbols refer to the electron and positron spin respectively.

The energy levels of Ps can be defined by the quantum numbers: n, l, S, and J where n is the principal quantum number, l, S, and $J = l + S$ are the orbital, spin, and total angular momentum respectively. Henceforth, states of Ps will be labelled using the spectroscopic notation $n^{2S+1}l_J$. It should be noted that a state with $l = 0$ will be denoted with the letter S (i.e. $n^{2S+1}\mathrm{S}_J$), which is not to be confused with the spin angular momentum, S. Quantum numbers such as l, S, and J are italicised for distinction.

Positronium [26, 27] is a hydrogen-like atom, but has a reduced mass of $\mu_{\mathrm{Ps}} = m_e/2$ instead of $\mu_{\mathrm{H}} \approx 0.9995 m_e$. This means that the gross energy levels of Ps are approximately half that of found in hydrogen (H) and can be described by [28]

$$E_n = -\frac{\alpha^2 \mu_{\mathrm{Ps}} c^2}{2n^2} = -\frac{m_e \alpha^2 c^2}{4n^2} \approx -\frac{6.8\ \mathrm{eV}}{n^2}, \tag{1.5}$$

where α is the fine structure constant, μ_{Ps} is the reduced mass for Ps, m_e is the mass of the electron, and c is the speed of light in vacuum. Therefore, the binding energy of ground state ($n = 1$) Ps is 6.8 eV instead of 13.6 eV. In addition, the Bohr radius for Ps (a_{Ps})[1] is approximately twice as large compared to hydrogen (a_H) These similarities between Ps and H are illustrated in figure 1.1.

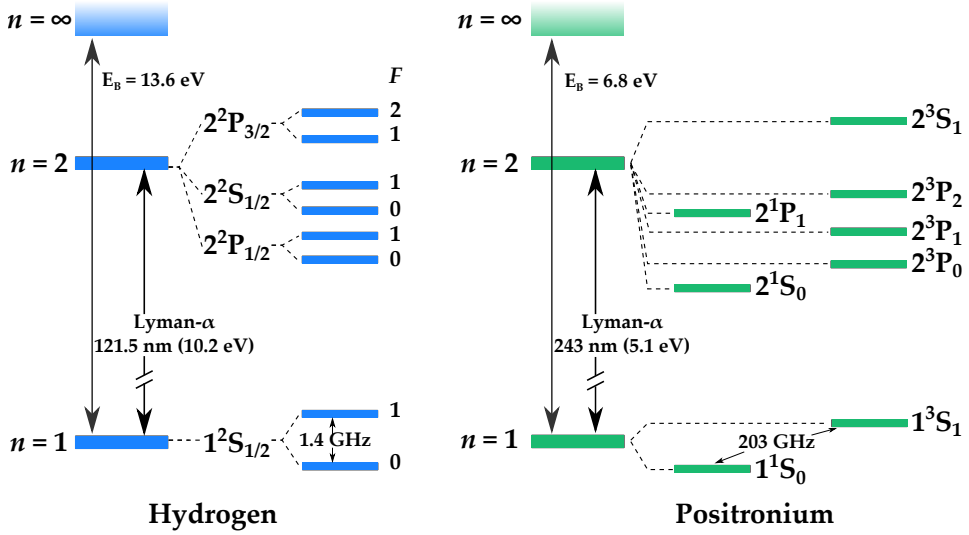

Figure 1.1: Energy level diagram of hydrogen (H) and positronium (Ps) in the $n = 1$ and $n = 2$ levels. At the gross (Bohr) level, properties such as the binding energy and 1S-2P interval differ by approximately a factor of 2 between Ps and H.

1.2.2 Beyond the Similarities

Similarities between positronium and hydrogen soon disappear beyond the gross level. Unlike in hydrogen, the spin-orbit coupling and the spin-spin interactions in Ps are of the same order. The hyperfine structure (HFS) in Ps does not exist, but the triplet-singlet level energy difference in the ground state of Ps is often labelled as the hyperfine splitting (E_{hfs}). Due to the large magnetic moment of the positron compared to the proton ($\mu_{e^+} \approx 658\mu_p$), and QED effects such as virtual annihilation, the fine structure ($n = 2$) and hyperfine separation ($n = 1$) are significantly different to those of hydrogen.

[1]The Bohr radius is defined as the most probable distance between the electron and nucleus. In Ps the electron and positron revolve around their common centre of mass, therefore the Ps Bohr radius is actually the diameter of the electron orbit.

According to equation 1.5, all states in each n level are degenerate. In 1944, Pirenne calculated the $\mathscr{O}(m_e\alpha^4c^2)$ corrections to the ground-state energy levels as follows [29]:

$$\Delta E(1^3S_1) = m_e\alpha^4c^2\left(\frac{1}{12} - \frac{5}{64} + \frac{1}{4}\right), \tag{1.6}$$

$$\Delta E(1^1S_0) = m_e\alpha^4c^2\left(-\frac{1}{4} - \frac{5}{64}\right). \tag{1.7}$$

The first and second terms in both equation 1.6 and equation 1.7 arise from the electron and positron spin-spin interactions and relativistic corrections to the Hamiltonian, respectively. Virtual annihilation, which is forbidden in the singlet state of Ps at this order due to charge conjugation invariance (and entirely non-existent in hydrogen), contribute to the third the term in the triplet level shift [29].

From equations 1.7 and 1.6, the hyperfine structure (HFS) splitting between the triplet and singlet states in the $n = 1$ state can then be written as

$$\Delta E^{\mathrm{Ps}}_{\mathrm{hfs}} = \Delta E(1^3S_1) - \Delta E(1^1S_0) = \frac{7}{12}m_e\alpha^4c^2 \approx 203\ \mathrm{GHz} \tag{1.8}$$

Virtual annihilation channels contribute approximately 40% to the $\Delta E^{\mathrm{Ps}}_{\mathrm{hfs}}$ energy. In contrast, $\Delta E^{\mathrm{H}}_{\mathrm{hfs}}$ in hydrogen has a value of only $\approx$1.4 GHz [30].

The expressions in equation 1.6 and equation 1.7 can be generalised for positronium in a state with arbitrary n, l, S, and J. They were calculated independently by Pirenne [29] and Berestestski [31]. The expressions were later corrected by Ferrell [32] and can be written as:

$$\Delta E_{n,l,S,J} = \frac{m_e\alpha^4c^2}{n^3}\left[\frac{11}{64n} - \frac{(1+\varepsilon_{l,J}/2)}{2(2l+1)}\right], \tag{1.9}$$

where $\varepsilon_{l,J} = 0$ for $S = 0$ and for $S = 1$,

$$\varepsilon_{l,J} = -\frac{7}{3}\delta_{l,0} + (1-\delta_{l,0}) \begin{pmatrix} \frac{-(3l+4)}{(l+1)(2l+3)}, J = l+1 \\ \frac{1}{l(l+1)}, J = l \\ \frac{(3l-1)}{l(2l-1)}, J = l-1 \end{pmatrix}, \tag{1.10}$$

where $\delta_{l,0}$ is the Kronecker delta. It should be noted that the equation 1.10 takes into account a factor 7/12 missing from the first Kronecker delta term in the version given by Ferrell [32, 33]. From equation 1.9 and equation 1.10, the fine structure splitting of the $n = 2$ level can be calculated at the $m_e\alpha^4c^2$ order.

As a particle-antiparticle system positronium is intrinsically unstable against annihilation and this feature makes Ps markedly different than most atoms. The annihilation rate of Ps is dependent on the overlap of the positron and electron wavefunctions and therefore, varies for different states. For a Ps atom in an arbitrary state n and $l = 0$, the lowest order annihilation rate in the singlet state was calculated by Wheeler in 1946 [23], while the lowest order triplet state annihilation rate was calculated in 1949 [34]. The singlet and triplet annihilation rates can be expressed as,

$$\Gamma(n^1\mathrm{S}_0) = \frac{1}{2}\frac{m_e\alpha^5c^2}{\hbar n^3} \approx \frac{8\ \mathrm{GHz}}{n^3} \tag{1.11}$$

$$\Gamma(n^3\mathrm{S}_1) = \frac{2}{9\pi}(\pi^2-9)\frac{m_e\alpha^6c^2}{\hbar n^3} \approx \frac{7\ \mathrm{MHz}}{n^3}. \tag{1.12}$$

For the ground state ($n = 1$), $\Gamma(1^1\mathrm{S}_0)$ and $\Gamma(1^3\mathrm{S}_1)$ are approximately 8 GHz and 7 MHz, which equate to lifetimes against annihilations of 125 ps [35] and 142 ns [36] respectively. Higher-order contributions to the annihilation rates have also been calculated [27]. Ps atoms in excited states can have both annihilation and radiative decays. In the former channel the atom decays into gamma-rays, while during radiative decay the atoms drops down to a lower energy level.

The presence of annihilation processes, both virtual and real, have an effect

on the energy levels of Ps and different states have different decay rates. For $l = 0$ (nS) states, the positron and electron wave function overlap (a requirement for self-annihilation) is non-zero: therefore, the annihilation rate is faster than the radiative decay rate. Whereas for states with $l > 0$, such as the 2P states, the overlap of the wave functions is zero resulting in lifetimes against annihilation longer than 142 ns [37, 38]. Both annihilation ($\tau_{\text{ann.}}$) and radiative ($\tau_{\text{rad.}}$) lifetimes for the ground state ($n = 1$) and first excited state ($n = 2$) of Ps are given in table 1.1.

State	$\tau_{\text{ann.}}$(ns)	Ref.	$\tau_{\text{rad.}}$(ns)	Ref.
1^1S_0	0.125	[23]	N/A	N/A
1^3S_1	142	[34]	$\gtrsim 10^{16}$	[39]
2^1S_0	1	[40]	$\simeq$ 243 100 000	[41]
2^3P_0	100 000	[37]	3.19	[42]
2^3P_1	$\simeq \infty$	[37]	3.19	[42]
2^1P_1	3 330 000	[38]	3.19	[42]
2^3P_2	384 000	[37]	3.19	[42]
2^3S_1	1 136	[34]	$\simeq$ 243 100 000	[41]

Table 1.1: Calculated annihilation ($\tau_{\text{ann.}}$) and radiative ($\tau_{\text{rad.}}$) lifetimes for Ps in $n = 1$ and $n = 2$ states.

The lifetime of each state is, in practice, dictated by the largest decay rate of the two modes. In general, only the 1^1S_0, 1^3S_1, 2^1S_0, and 2^3S_1 states can self-annihilate, while the 2P states will radiatively decay to one of the 1S states before annihilation. Ps atoms in highly excited (Rydberg) states [43] have radiative lifetimes much longer than the ground state annihilation lifetimes. These Rydberg state radiative lifetimes vary with n^4 for S, D states, but if circular states ($l = n - 1$) are populated the lifetimes scale with n^5 [44]. In addition, the annihilation dynamics of positronium in the excited states has been shown to be controllable with external electric and magnetic fields [14, 45].

A positronium atom with orbital angular momentum l and spin S quantum numbers is permitted to annihilate into N_γ photons in order to conserve charge conjugation invariance [46, 47]. This selection rule can be written as

$$(-1)^{N_\gamma} = (-1)^{l+S}. \tag{1.13}$$

For Ps in the ground states (where $l = 0$), the singlet ($S = 0$) and triplet ($S = 1$) states can annihilate into even and odd numbers of photons respectively. Radiationless ($N_\gamma = 0$) and single-photon ($N_\gamma = 1$) annihilations are forbidden by angular momentum and energy conservation laws, while higher order channels are allowed, but strongly suppressed. Therefore, the annihilation photons from the decay of singlet and triplet states are dominated by two and three gamma-rays respectively.

1.3 Positronium Spectroscopy

1.3.1 Search for Optical Excitation of Ps

Positronium atoms have also been created in the excited states. In an experiment performed by Canter and colleagues in 1975 [48] the radiative decay of Ps from the $n = 2$ state was observed. Here, positrons were implanted into a single crystal Ge target and some Ps atoms were naturally created in the $n = 2$ state with an efficiency of $\approx 0.01\%$ [48]. The 2P$\rightarrow$1S decay emits a 243 nm photon, which was detected to monitor the excited state formation. This was a first step towards spectroscopy of excited state positronium (Ps*), but a more efficient method of Ps* production was evidently necessary.

After some unsuccessful attempts [49–51] the first measurement of the optical excitation of positronium from the ground state was achieved in 1982 [52]. Moderated positrons trapped in a magnetic bottle were ejected in a $\Delta t_{\mathrm{FWHM}} \approx 10$ ns pulse towards a single crystal Cu target [52]. Approximately 4 of the incoming 20 positrons formed slow Ps in the 1^3S_1 state. The $1^3S_1 \rightarrow 2^3S_1$ transition was observed using two-photon Doppler free excitation and photoionisation of the excited state atoms with the same laser.

Another two-photon excitation of the $1^3S_1 \rightarrow 2^3S_1$ transition was conducted in 1984 [53]. Approximately 100 positrons per pulse were implanted into an Al target to produce Ps atoms for laser excitation [53]. This proved to be a better measurement, but a significant improvement was made through the employment of

continuous-wave (CW) lasers, and an electron microtron accelerator as the positron source. This experiment [54], performed with 2.6 ppb uncertainty, is the most precise spectroscopic measurement of Ps made to date.

Excitation of Ps to high n, or Rydberg, states was first observed in 1990 [55]. Although the number of positrons generated from the electron linear accelerator (LINAC) was higher than in previous experiments, the observed excitation signal was very weak due to the small amount of Ps produced from the Cu target. Nevertheless, excitation of Ps atoms to the $n = 13 - 15$ states, using a two-photon, two-colour excitation scheme, was observed. The use of a LINAC in a university laboratory is, however, not practical. This meant that progress in Ps spectroscopy did not advance significantly for a number of years.

The advent of the Surko trap [56] marked a significant progress in the field of positronium spectroscopy [57–60]. These positron traps are compact ($\approx$ 1 m in length) and therefore, can be easily installed in a small laboratory. Over 10^5 positrons can be accumulated in such traps and ejected in a $\sim$ 5 ns pulse towards a target material to form a dense cloud of positronium. The use of Surko traps, coupled with a new detection technique [61], proved to be a vital step in further advancing positronium spectroscopy. This facilitated an improved production and detection of Rydberg Ps [58], as well as generation of Ps Stark states [62], which have been exploited to perform atom manipulation techniques [60, 63]. Another milestone in Ps physics has been the creation [64] and optical spectroscopy [65] of the Ps_2 molecule. These experiments are a stepping stone towards the formation of Ps Bose-Einstein condensate (BEC) [66], pursued for its implications in precision spectroscopy and interferometry experiments.

1.3.2 Tests of QED Theory

The vulnerability of Ps to self-annihilation, which may appear as a limitation in Ps research at a first glance, makes it a unique system to study. As a purely leptonic system, positronium is an excellent test-bed for testing quantum electrodynamics

(QED) theory via the spectroscopy of its energy levels, or measurement of decay rates [67]. The absence of a proton means that only electromagnetic forces have to be considered in Ps. The study of Ps is interesting because annihilation channels, due to its part antimatter nature, have to be taken into account. The energy levels of Ps are well defined by QED and any discrepancy with theory can be an indication of new physics if experimental errors can be ruled out [68]. There has been a prediction of an ultra fine splitting (≈ 75 kHz) between the 2P singlet state and the spin averaged triplet state arising at order $m_e\alpha^6c^2$ [69]. Such effects, although beyond the precision of Ps spectroscopy today, may be observable if higher precision can be achieved.

The energy levels of Ps up to the order $m_e\alpha^4c^2$ were expressed earlier in equation 1.9 and 1.10. Higher order corrections up to the order $m_e\alpha^6c^2$ have also been calculated [70–73], with the $m_e\alpha^7c^2$ corrections in progress [74–78]. The ground state hyperfine interval ($1^3S_1 \rightarrow 1^1S_0$) [79–82], the $n = 2$ fine structure intervals [83–85], and the $1^3S_1 \rightarrow 2^3S_1$ interval [52–54, 86] of positronium have been previously measured. The most recent measurements and theoretical calculations are summarised in table 1.2.

The energy levels of Ps in the $n = 1$ and $n = 2$ states are illustrated in figure 1.2. As explained earlier, the 2S states have greater annihilation rates than radiative decay rates. In contrast, the 2P states have larger radiative decay rates. Therefore, the 2P states are short-lived and radiatively decay to $n = 1$ level after a mean radiative lifetime of 3.19 ns, emitting a 243 nm Lyman-α photon in the process. The fine structure intervals are labelled by ν_J in figure 1.2, and the dominant lifetime for each state is also indicated. The $2^3S_1 \rightarrow 2^1P_1$ transition is a single-photon forbidden transition in a zero magnetic field due to charge-conjugation invariance, but can be observed for non-zero magnetic field due to Zeeman mixing [87, 88]. The ground state hyperfine interval ($1^3S_1 \rightarrow 1^1S_0$) has been measured to a precision of 3.6 ppm [82], only a factor of 1.8 times less precise than theoretical calculations.

Transition	Experiment (MHz)	Precision (Exp.)	Ref.	Theory (MHz)	Precision (Th.)	Ref.
$1^3S_1 \rightarrow 1^1S_0$	203 389.10 $\pm$ 0.74	3.6 ppm	[82]	203 391.69$\pm$ 0.41	2.0 ppm	[75]
$1^3S_1 \rightarrow 2^3S_1$	1 233 607 216.4 $\pm$ 3.2	2.6 ppb	[54]	1 233 607 222.18 $\pm$ 0.58	0.8 ppb	[72]
$2^3S_1 \rightarrow 2^1P_1$	11 180.0 $\pm$ 5.0$_{\text{stat}}$ $\pm$ 4.0$_{\text{sys}}$	600 ppm	[88]	11 185.37 $\pm$ 0.08	7 ppm	[72]
$2^3S_1 \rightarrow 2^3P_0$	18 499.65 $\pm$ 1.20$_{\text{stat}}$ $\pm$ 4.00$_{\text{sys}}$	230 ppm	[85]	18 498.25 $\pm$ 0.08	4 ppm	[72]
$2^3S_1 \rightarrow 2^3P_1$	13 012.42 $\pm$ 0.67$_{\text{stat}}$ $\pm$ 1.54$_{\text{sys}}$	130 ppm	[85]	13 012.41 $\pm$ 0.08	6 ppm	[72]
$2^3S_1 \rightarrow 2^3P_2$	8 624.38 $\pm$ 0.54$_{\text{stat}}$ $\pm$ 1.40$_{\text{sys}}$	170 ppm	[85]	8 626.71 $\pm$ 0.08	10 ppm	[72]

Table 1.2: The most recent optical and microwave precision spectroscopy measurements of Ps including the $n = 1$ hyperfine structure interval and $n = 2$ fine structure intervals. The relative precisions are stated for the experimental measurements and theoretical calculations.

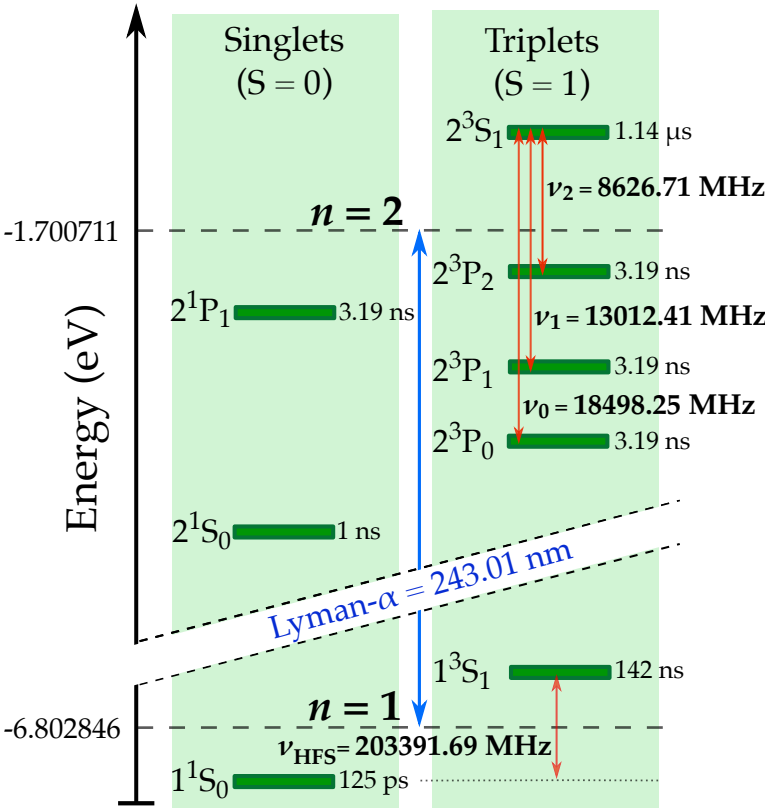

Figure 1.2: Energy level diagram for Ps in the $n = 1$ and $n = 2$ state. The energy for individual sub-states are shown relative to the Bohr (i.e., $\mathcal{O}(m_e\alpha^2c^2)$) level. The dominant lifetime for each state is also quoted. The fine structure and hyperfine structure transitions are indicated by the vertical arrows with corresponding frequencies stated. The frequency values are from [72].

Tests of QED theory can also be done via the measurement of the Ps annihilation rates [89–91]. The leading annihilation rates for singlet and triplet states with $l = 0$ were given earlier in equations 1.11 and 1.12. The measurements of the ortho-Ps annihilation rate were not in agreement with theory initially and the discrepancy was called the 'ortho-Ps lifetime puzzle'. After the effects from non-thermalised Ps were accounted for, new measurements were performed and were in agreement with the QED calculations [36, 92]. The annihilation rate of para-Ps has also been measured [35] and good agreement with theory was found.

The splitting of the ground state triplet (1^3S_1) and singlet (1^1S_0) levels is the Ps hyperfine structure interval ($\Delta E^{\mathrm{Ps}}_{\mathrm{hfs}}$), which been measured indirectly [80, 82]. This indirect method relies on the measurement to be done in a static magnetic field,

which induces Zeeman mixing between the $1^3S_1(M_J = 0)$ and $1^1S_0(M_J = 0)$ states (figure 2.2). The mixing (Δ_{mix}) depends on the $\Delta E^{\text{Ps}}_{\text{hfs}}$, and thus the $\Delta E^{\text{Ps}}_{\text{hfs}}$ can be extracted by measuring Δ_{mix}.

The theoretical calculation of the HFS transition is $\Delta E^{\text{Ps}}_{\text{hfs}}$(th.) = 203,391.69 $\pm$ 0.41 MHz (2 ppm) [75]. The two most precise HFS measurement have a combined result of $\Delta E^{\text{Ps}}_{\text{hfs}}$(exp.) = 203,388.65 $\pm$ 0.67 MHz (3.3 ppm) [80, 82], which amounts to a disagreement of $\approx 4\sigma$ with theory. The discrepancy could be due to systematic effects from the nonthermalised Ps atoms, or the non-uniformity of the static magnetic field. If the theory is correct, and the disagreement still persists after systematic checks are verified, then the disagreement could be an indication of contribution from new physics. A new experiment designed to investigate non-thermal Ps effects was carried out [81], yielding a result of 203,394.20 $\pm$ 2.06 MHz (10 ppm). The new measurement is in good agreement (1.2σ) with theoretical calculations but disagrees with previous results [80, 82] by 2.6σ. The magnitude of the non-thermal Ps effects was dependent on the time windows selected for analysis and were found to be half as large as the largest systematic uncertainty [81]. The use of time selection, however, resulted in poorer statistics, with a reduction in precision by a factor of ≈ 3 compared to previous measurements [80, 82]. More precise and independent measurements are needed to resolve the HFS interval issue.

1.3.3 Previous Measurements of the $n = 2$ Fine Structure Intervals

The $n = 2$ Ps fine structure interval measurements pertinent to this thesis have been performed previously at Brandeis [83], Michigan [84], and Mainz [85] as summarised in figure 1.3. Compared to the 80 kHz uncertainty in the QED calculations the experimental uncertainties are of the order of few MHz, and have not progressed for the last 25 years. Here, limitations mainly arising from the inefficient 2^3S_1 state production, as well the detection of Lyman-α radiation resulted in such large uncertainties as shown in figure 1.3.

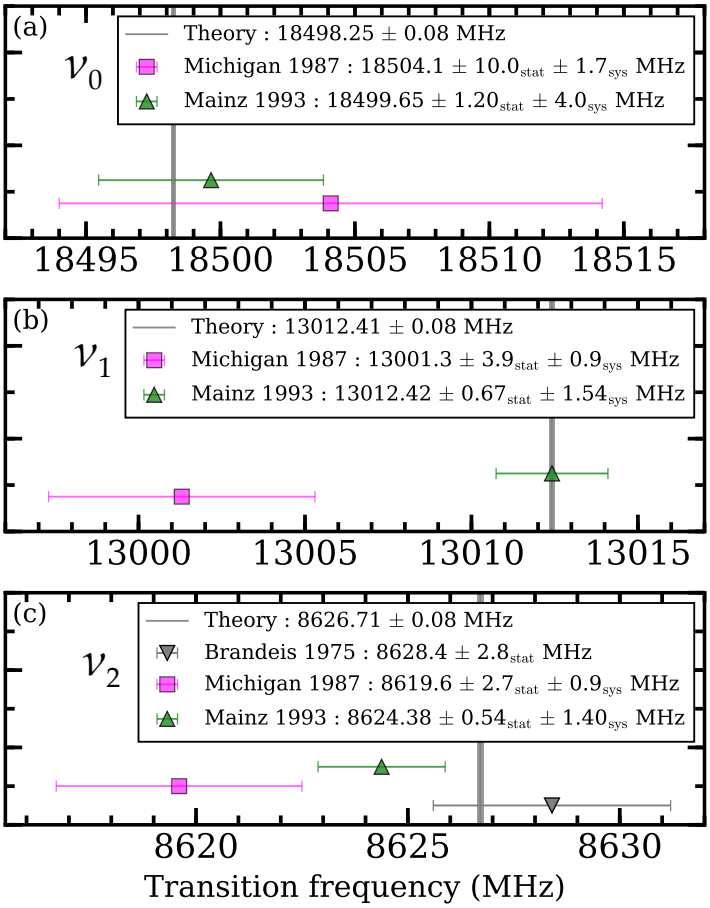

Figure 1.3: Summary of the previous measurements of the (a) ν_0, (b) ν_1, and (c) ν_2 Ps $n = 2$ fine structure intervals performed in Brandeis [83], Michigan [84], and Mainz [85]. The vertical lines indicate the current theoretical values of each interval [72].

The experiment conducted in Mainz [85] was the third measurement (and the most precise to date) of the $n = 2$ fine structure intervals. Here, positrons were extracted out of the magnetic field with electrostatic lenses and directed into a molybdenum (Mo) foil inside a WR-90 waveguide as shown in figure 1.4. Approximately 0.4% of the positrons naturally produced Ps in the $n = 2$ states. If equal population of all 16 substates is assumed, the resulting 2^3S_1 production efficiency was calculated to be on the order of 0.4% $\times$ 3/16 = 0.08%. 12 out of the 16 substates were in the 2P states which radiatively decayed to the 1S states by emitting a 243 nm Lyman-α photon. The $2^3S_1 \rightarrow 2^3P_J$ transitions were then driven with microwave radiation in the WR-90 waveguide. Similar to the background 2P states, once atoms

were driven to the 2^3P_J, they decayed to the 1^3S_1 state by emitting a background Lyman-α photon. These 243 nm photons were then detected by a photomultiplier (PM), separated from the waveguide with a light guide and located outside the vacuum chamber. A schematic of the Mainz experimental setup is shown in figure 1.4.

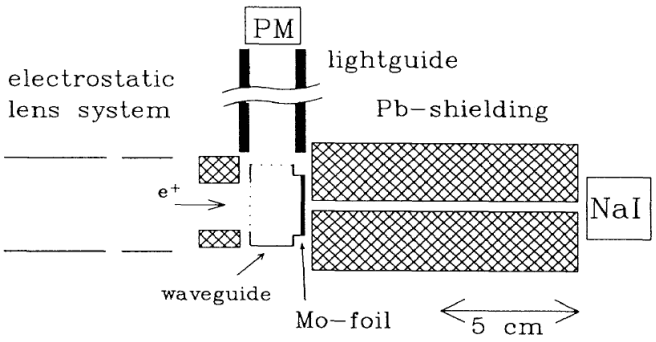

Figure 1.4: Experimental setup in the Ps $n = 2$ fine structure measurement conducted in Mainz in 1993. The positrons were extracted out of the magnetic field with electrostatic lenses and implanted into a Mo foil target located inside a WR-90 waveguide. 2^3S_1 were naturally generated and the microwave induced transitions to the 2^3P_J were detected by the photomultiplier (PM) located outside the chamber. The NaI detector was used to monitor the position of the incoming positron beam. From [85].

The $2^3S_1 \rightarrow 2^3P_J$ transitions were identified by monitoring the change in the 243 nm light detected by the PM. The increase in the 243 nm photon count was $\approx$ +0.05% when the microwave radiation was tuned to be on resonance. Lineshapes for the all three transitions were then generated by monitoring the PM counts as a function of the microwave frequency. These lineshapes are shown in figure 1.5, where the data were fitted with a Lorentzian function. After the systematic uncertainties were determined, the resonance frequencies of $18499.65 \pm 4.18_{\text{stat+sys}}$, $13012.42 \pm 1.68_{\text{stat+sys}}$, and $8624.38 \pm 1.50_{\text{stat+sys}}$ MHz were determined for the $2^3S_1 \rightarrow 2^3P_J$ ($J = 0, 1, 2$) transitions respectively.

While this technique did not require lasers for the production of 2^3S_1 states, energies of the atoms were on the order of 1 eV or higher which resulted in transit time broadening. This type of broadening effect arises from the interaction time between the atoms and radiation field [93]. Transit time broadening can be reduced by in-

creasing the time of flight through the radiation field or using slower atoms. The use of fast atoms also meant that higher powers of microwave radiation were needed to drive the transitions, which can lead to power broadening of the lineshapes. This type of line broadening results when the absorption rate is increased due to high radiation intensity. In addition, the 2P states generated after positron bombardment into the target contributed to a large background signal present during the detection of the 243 nm Lyman-α photon following $2^3S_1 \rightarrow 2^3P_J$ transition. This further limited the precision of the previous experiments.

It is apparent from table 1.2 that the fine structure experimental data are severely behind theoretical calculations and new measurements have to be made to close this large gap. Precision studies of positronium may also shed some light on the observed matter-antimatter asymmetry. According to the Standard Model (SM), matter and antimatter were produced in equal amounts during the Big Bang, but the universe as we know today is dominated by matter. The solution to this problem may lie in new forces or particles unaccounted for in the SM, and may benefit from the study of antimatter systems like Ps. Therefore, if areas of new physics are to be explored with positronium, then experiments have to performed with uncertainties comparable to theoretical predictions. While the long-term goal of Ps precision study may be to test new physics (and perhaps be able to offer some insight into the 'proton radius puzzle' [94, 95]), the short-term goal is a new and more precise measurement of the $n = 2$ Ps fine structure intervals to test QED theory.

In this thesis I outline a new measurement of the Ps $n = 2$ fine-structure intervals. A buffer gas positron trap, coupled to a radioactive source, was used to generate a positron pulse that was then deposited on a SiO_2 film to produce Ps atoms. These near thermal atoms ($\approx$ 50 meV) were optically excited to the 2^3S_1 state, before the $\nu_J = 2^3S_1 \rightarrow 2^3P_J$ ($J = 0,1,2$) transitions were driven in a microwave guide. This new technique has delivered a factor of $\approx$5 improvement in precision compared to the previous measurements, and is a step towards progressing the field of precision Ps spectroscopy The ν_1 and ν_2 transition lineshapes were found to be

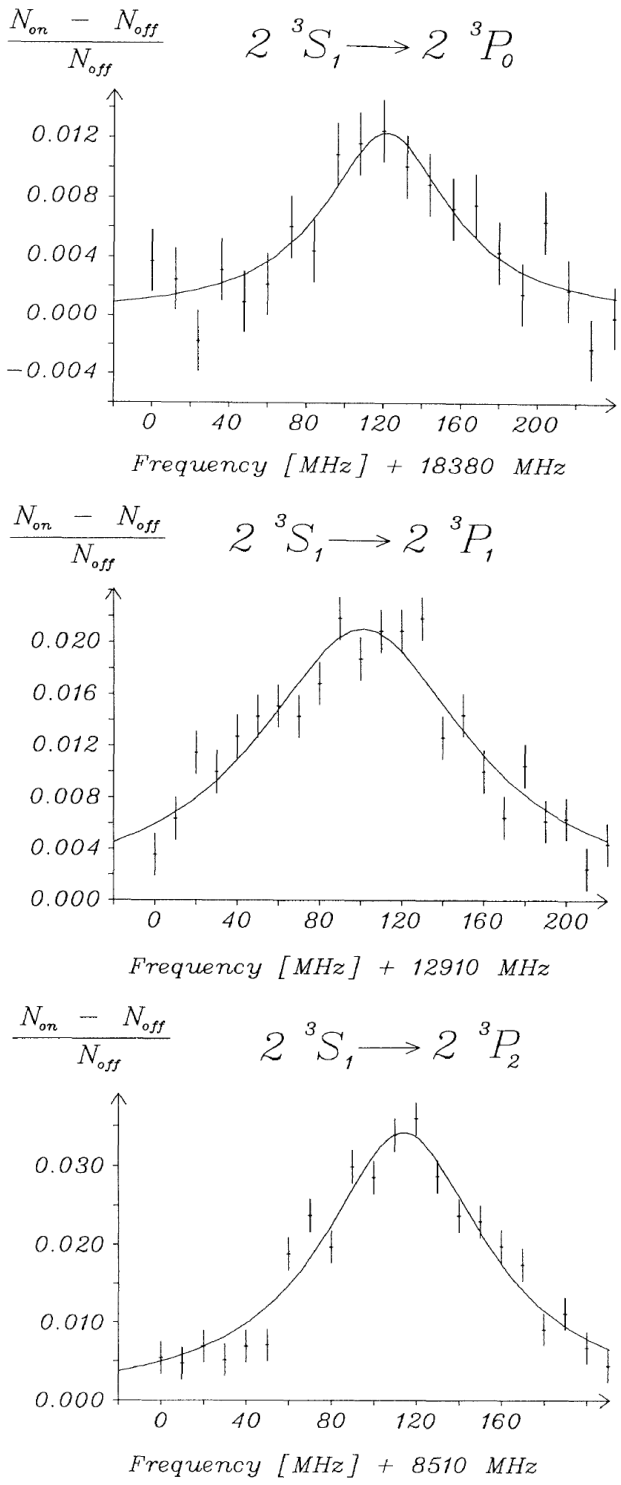

Figure 1.5: Measured lineshapes of the $2^3S_1 \rightarrow 2^3P_J$ ($J = 0, 1, 2$) transitions performed in Mainz [85]. The data were fitted with a Lorentzian function, and the final resonance frequency values from the measurements were 18499.65 ± 4.18 MHz, 13012.42 ± 1.68, and 8624.38 ± 1.50 MHz for $J = 0, 1, 2$ transitions respectively. From [85].

asymmetric which prevents the determination of the resonance frequency. The ν_0 lineshape is not asymmetric, but its measured resonance frequency disagrees with theoretical calculation [72]. A shift in line centre due to known quantum interference effects are too small for account for the observed disagreements. Future work to address the asymmetry and disagreement with theory are outlined.

Chapter 2

Theoretical Background

2.1 QED Calculations

Following the first order correction given by Ferrell [32] in equation 1.9 and equation 1.10, higher order QED corrections to the Ps $n = 2$ energy levels have been calculated up to $m_e\alpha^6c^2$ [70–73]. The $m_e\alpha^7c^2$ corrections are in progress [74, 75, 77, 78].

The energies of Ps in the $n = 2$ triplet states, up to the $\mathcal{O}(m_e\alpha^6c^2)$, can be expressed as [72]:

$$E(2^3S_1) = \frac{1}{8}m_ec^2\left(-\frac{1}{2}\alpha^2 + \frac{65}{384}\alpha^4 + A_{S5}\alpha^5 + A_{S6}\alpha^6 + ...\right), \tag{2.1}$$

$$E(2^3P_0) = \frac{1}{8}m_ec^2\left(-\frac{1}{2}\alpha^2 - \frac{95}{384}\alpha^4 + A_{05}\alpha^5 + A_{06}\alpha^6 + ...\right), \tag{2.2}$$

$$E(2^3P_1) = \frac{1}{8}m_ec^2\left(-\frac{1}{2}\alpha^2 - \frac{47}{384}\alpha^4 + A_{15}\alpha^5 + A_{16}\alpha^6 + ...\right), \tag{2.3}$$

$$E(2^3P_2) = \frac{1}{8}m_ec^2\left(-\frac{1}{2}\alpha^2 - \frac{43}{1920}\alpha^4 + A_{25}\alpha^5 + A_{26}\alpha^6 + ...\right), \tag{2.4}$$

where the terms A_{S5}, A_{S6}, A_{05}, A_{06}, A_{15}, A_{16}, A_{25}, and A_{26} have been calculated.

The fine structure intervals can then be determined from the four equations above and are listed in table 2.1.

It can be seen from the four equations above that the degeneracy in levels with $n = 2$ is lifted by the $m_e\alpha^4c^2$ (lowest order) correction, arising due to relativistic, spin-orbit, and spin-spin effects. The $m_e\alpha^5c^2$ corrections due to recoil effects, vacuum polarisation, and virtual annihilations are quite prominent in the 2S states, amounting to 50 - 300 MHz. Virtual annihilation effects are absent in the 2P states and $m_e\alpha^5c^2$ corrections are only 1-20 MHz in magnitude as these effects are "short-range" and thus, depend on the wave-function overlap near the origin [96].

Transition	$\mathcal{O}(m_e\alpha^4c^2)$ (MHz)	$\mathcal{O}(m_e\alpha^5c^2)$ (MHz)	$\mathcal{O}(m_e\alpha^6c^2)$ (MHz)
$2^3S_1 \rightarrow 2^3P_2$	8 394.45	8 625.25	8 626.71
$2^3S_1 \rightarrow 2^3P_1$	12 774.17	13 010.90	13 012.41
$2^3S_1 \rightarrow 2^3P_0$	18 248.81	18 496.14	18 498.25

Table 2.1: The $n = 2$ Ps fine structure intervals for different orders of QED corrections. The values are from [32], [97], and [72] for the three orders listed above respectively.

2.2 Zeeman and Stark Effects

The energies of Ps atoms in the $n = 2$ states listed in equation 2.1- 2.4 are the unperturbed energies when external fields are not present. The effects of magnetic and electric fields for Ps in the $n = 2$ states have been previously calculated [98, 99]. The strengths of the electric and magnetic fields used in the experiments do not result in overlapping of the $n = 2$ states with the neighbouring $n = 1$ and $n = 3$ states.

Employing the treatment used by Bethe and Salpeter [42], the eigenvalues and eigenvectors of the Hamiltonian matrix in an $|nSlJM_J\rangle$ basis were calculated, where n is the principal quantum number, S is the total spin quantum number, l is the orbital angular momentum quantum number, $J = l + S$ is the total angular momentum quantum number, and M_J is the projection of $\overrightarrow{J}$ onto the axis parallel to the quantisation axis. The applied electric and magnetic fields in our measurements were

orientated parallel to the z axis, which was defined as the quantisation axis.

The total Hamiltonian matrix of a Ps atom in an electric and magnetic field can be expressed as:

$$\hat{H} = \hat{H}_0 + \hat{H}_{\mathrm{Z}} + \hat{H}_{\mathrm{S}}, \tag{2.5}$$

where $\hat{H}_0$ is the field-free Hamiltonian. $\hat{H}_{\mathrm{Z}} = -\overrightarrow{\mu}_{\mathrm{mag}} \cdot \overrightarrow{B}$ is the Zeeman Hamiltonian due to magnetic field, where $\overrightarrow{\mu}_{\mathrm{mag}} = \overrightarrow{\mu}_{\mathrm{e^-}} + \overrightarrow{\mu}_{\mathrm{e^+}}$ is the total magnetic moment the atom. $\hat{H}_{\mathrm{S}} = -e\overrightarrow{F} \cdot \overrightarrow{r}$ is the Stark Hamiltonian due to the electric field $\overrightarrow{F}$, where e and $\overrightarrow{r}$ are the electron charge and position vector respectively.

As strong fields were not used in our measurements, there were no overlaps with the neighbouring n states and a 16×16 matrix in the $|nSlJM_J\rangle$ basis was sufficient to express the total Hamiltonian for the states with $n = 2$. The 16 basis states represent the individual 16 M_J substates with $n = 2$.

2.2.1 Stark Effects

The matrix elements representing the interaction between the substates $|nSlJM_J\rangle$ and $|nS'l'J'M_J'\rangle$ of the Stark Hamiltonian due to an electric field $\overrightarrow{F} = (0,0,F)$, evaluated using the Wigner-Eckart theorem, take the form [99]

$$\begin{aligned}\left\langle nS'l'J'M_J' \middle| \hat{H}_{\mathrm{S}} \middle| nSlJM_J \right\rangle &= \delta_{S',S}(-1)^{S+l+M_J'} \left\langle n'l' \middle| r \middle| nl \right\rangle eF \\ \times \sqrt{\max(l',l)(2J'+1)(2J+1)} &\begin{pmatrix} J' & 1 & J \\ -M_J' & 0 & M_J \end{pmatrix} \begin{Bmatrix} S' & l' & J' \\ 1 & J & l \end{Bmatrix},\end{aligned} \tag{2.6}$$

where $\delta_{x',x}$ is the Kronecker delta symbol, $\left\langle n'l' \middle| r \middle| nl \right\rangle$ is a radial matrix element, and the last two terms are the Wigner 3J and 6J symbols, respectively. For two states with angular momentum J and J', the Wigner-Eckart theorem separates the matrix elements of the spherical tensor operators into two parts: one that depends on the M_J quantum numbers and another that does not, which is often called a reduced matrix element.

The 3J and 6J symbols are related to Clebsch-Gordan coefficients arising from the addition of angular momenta. The expression on the right hand side of equation 2.6 is non-zero for $S^{'} = S$ and $\Delta l = \left| l - l^{'} \right| = \pm 1$. This means that the electric field couples the S ($l = 0$) and P ($l = 1$) states with the same spin. This coupling due to an external electric field is often called Stark mixing. Furthermore, for an external electric field oriented parallel to z axis, the bottom row of the 3J symbol in equation 2.6 introduces the selection rule $-M_J^{'} + 0 + M_J = 0$, i.e., $\Delta M_J = 0$. The elements in the upper row of the 3J symbols should satisfy the triangle rule (i.e. $\left| J^{'} - J \right| \leq 1 \leq J^{'} + J$). The 3J symbol, and hence the Stark mixing, are zero if these rules are not satisfied. The 6J symbol (often visually represented as a tetrahedron) is a combination of four 3J symbols, each satisfying the selection rules and forming one of the four vertices of a tetrahedron.

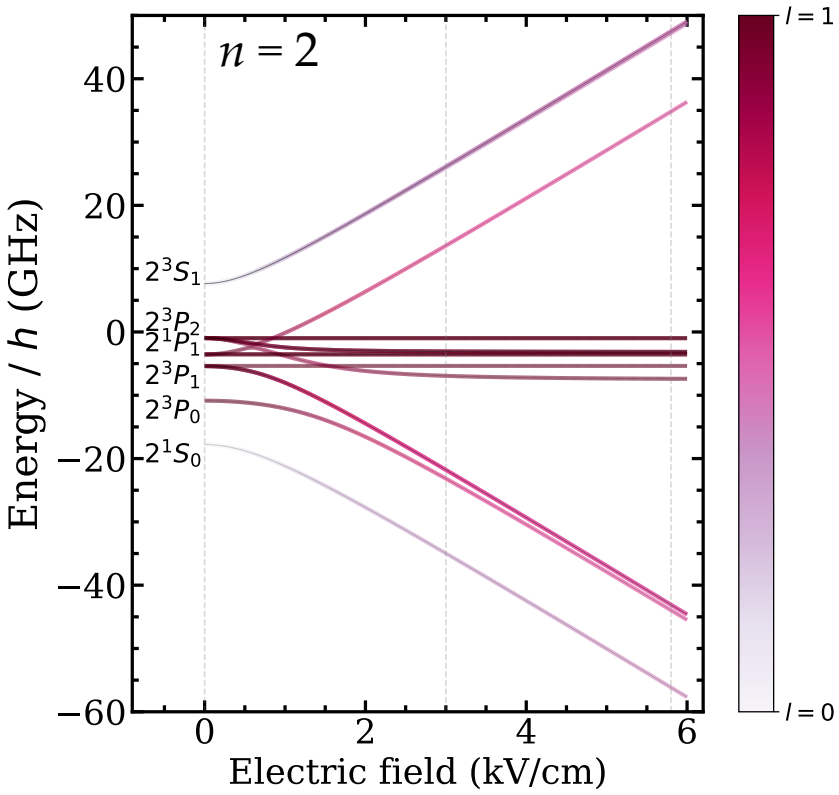

Figure 2.1: Stark structure of the $n = 2$ level for a range of electric field relevant in our measurement. The 2S and 2P states which are pure in zero electric field, gradually mix together in non-zero electric field as indicated by the colour intensity scale, and the energies shift away from the unperturbed energies.

The resulting Stark structure of Ps in the $n = 2$ level is shown in figure 2.1. When the electric field is zero, the energies of the $n = 2$ states are unaffected and the energy of the triplet states are quantified by the equations 2.1- 2.4. When the electric field is increased, the energies shift due to Stark mixing. With the aid of the colour intensity scale, it can be seen that the states have pure S ($l = 0$) or P ($l = 1$) character in zero electric field, but gradually acquire mixed l character when the electric field is non-zero. Some substates are not affected by the electric field as they do not satisfy the $\Delta M_J = 0$ rule imposed by the Wigner 3J symbol in equation 2.6. For example the $2^3P_2(\pm 2)$ substates do not shift as there are no $2^3S_1(\pm 2)$ substates, and mixing with the $2^3S_1(\pm 1)$ substates violates the $\Delta M_J = 0$ rule.

2.2.2 Zeeman Effects

The Zeeman Hamiltonian due to a magnetic field, aligned in the z direction, $\overrightarrow{B} = (0,0,B)$ can be written as:

$$\hat{H_Z} = (g_e \mu_B \hat{s}_{z_{e^-}} - g_e \mu_B \hat{s}_{z_{e^+}})B, \tag{2.7}$$

where g_e is the electron ($\equiv$ positron) spin-g factor, μ_B is the Bohr magneton, and $\hat{s}_{z_{e^-}}$ ($\hat{s}_{z_{e^+}}$) is the projection operator of electron (positron) spin onto the quantisation axis. The matrix elements representing the interaction between the substates $|nSlJM_J\rangle$ and $|nS'l'J'M'_J\rangle$ takes the form [99]

$$\begin{aligned}\left\langle nS'l'J'M'_J \middle| \hat{H_Z} \middle| nSlJM_J \right\rangle &= \delta_{l',l}\delta_{M'_J,M_J}(-1)^{l+M_J}[(-1)^{S+S'} - 1] \\ &\times \mu_B B \sqrt{3(2J'+1)(2J+1)} \begin{pmatrix} J' & 1 & J \\ -M'_J & 0 & M_J \end{pmatrix} \begin{Bmatrix} S' & l' & J' \\ J & 1 & S \end{Bmatrix},\end{aligned} \tag{2.8}$$

where $\delta_{x',x}$ is the Dirac delta function. The expression on the right hand side of equation 2.8 is non-zero for $l' = l$, $S' \neq S$, and $M'_J = M_J$. The $M'_J = M_J$ condition is the consequence of the selection rule of the 3J symbol as explained earlier. Therefore, the magnetic field couples the $S = 0$ and $S = 1$ states with same l and M_J,

causing Zeeman mixing.

The Ps population in the $n = 1$ level is only affected by Zeeman mixing. As both the 1^3S_1 and 1^1S_0 states have $l = 0$, the Stark effect (which causes l mixing) is absent. The Zeeman structure for the $n = 1$ states are shown in figure 2.2. The $1^1S_0(0)$ and $1^3S_1(0)$ states mix and experience an energy (Zeeman) shift due to the magnetic field. As there are no $1^1S_0(\pm1)$ substates, the $1^3S_1(\pm1)$ substates are unaffected by the magnetic field [100]. The magnitude of the Zeeman mixing shift (Δ_{mix}) is dependent on the strength of the magnetic field, and can be expressed by the Breit-Rabi formula [101]:

$$\begin{aligned} \Delta_{\text{mix}} &= \frac{\Delta W}{2}\left((1+x^2)^{1/2}-1\right) \simeq \frac{\Delta W}{4}x^2, \\ x &= \frac{2e\hbar B}{m_e \Delta W}, \end{aligned} \tag{2.9}$$

for small x, where ΔW is the energy difference of the singlet and triplet substates at $B = 0$. For the $n = 1$ level, $\Delta W = \Delta E^{\text{Ps}}_{\text{hfs}}$ as shown in figure 2.2.

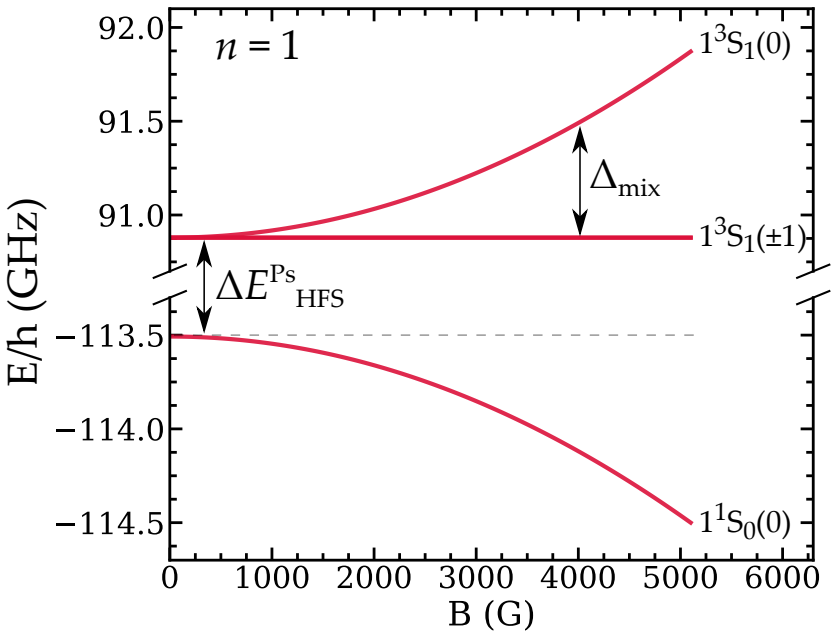

Figure 2.2: Zeeman structure of Ps in the $n = 1$ state. The $1^3S_1(\pm1)$ states are unaffected by the magnetic field as they do not have a mixing counterpart. At zero magnetic field, the 1^3S_1 and 1^1S_0 states are separated by $\Delta E^{\text{Ps}}_{\text{hfs}} \approx 203$ GHz.

From equation 2.9 it can be seen that the mixing strength is inversely proportional to the separation between the substates. Separation of the substates in excited levels have a n^{-3} dependence, as mentioned earlier in equation 1.9, and therefore, require a weaker field to mix. For a magnetic field strength of 100 G (0.01 T), Δ_{mix} for the 2^3S_1 state is ≈ 3 MHz. For the same field strength, Δ_{mix} in the 1^3S_1 state is only ≈ 0.4 MHz. From equation 2.9, the magnitude of the Zeeman mixing is found to be quadratic in B and no linear energy shift occurs. As mentioned earlier in section 1.3.1, the HFS interval ($\Delta E_{\text{hfs}}^{\text{Ps}}$) has been indirectly measured by measuring the mixing of the triplet and singlet ground states in a static magnetic field [80, 82].

The Zeeman structure of the $n = 2$ states is shown in figure 2.3. Similar to the $n = 1$ state, the $2^1S_0(0)$ and $2^3S_1(0)$ mix, and therefore shift in a magnetic field. The 2^1S_0 state does not have $M_J = \pm 1$ components: therefore, the $2^3S_1(\pm 1)$ substates are unaffected by the magnetic field [102]. This is also the case for the $2^3P_2(\pm 2)$ substates. The $2^3P_1(0)$ substate does have a $2^1P_1(0)$ counterpart to mix with, but does not shift because the $2^1P_1(0)$ and $2^3P_1(0)$ mixing matrix element in equation 2.8 is zero. The shift of the $n = 2$ substates also have a quadratic dependence on the magnetic field [102]. The allowed $2^3S_1 \rightarrow 2^3P_J$ transitions for $\Delta M_J = 0$ indicated by the vertical arrows in figure 2.3.

2.2.3 Zeeman and Stark Effects in the $n = 2$ Fine Structure

The Zeeman and Stark matrix elements can be combined to calculate the $n = 2$ energy levels by calculating the set of eigenvalues of the total Hamiltonian matrix. An atom interacts most strongly with the oscillating electric component of an electromagnetic field and transitions due to this interaction are governed by selection rules. According to electric dipole transition rules, optical transitions from the singlet and triplet ground states to the $n = 2$ states are allowed for the conditions: $\Delta S = 0$, $\Delta l = \pm 1$, and $\Delta J = 0, \pm 1$. The transition between states with $J = 0$ and $J' = 0$ is not allowed. Radiation polarised parallel to the quantisation axis is defined as π-polarised and satisfies the selection rule $\Delta M_J = 0$. Polarisation perpendicular to the z-axis is circularly polarised and carries angular momentum of $\pm\hbar$. Therefore, if

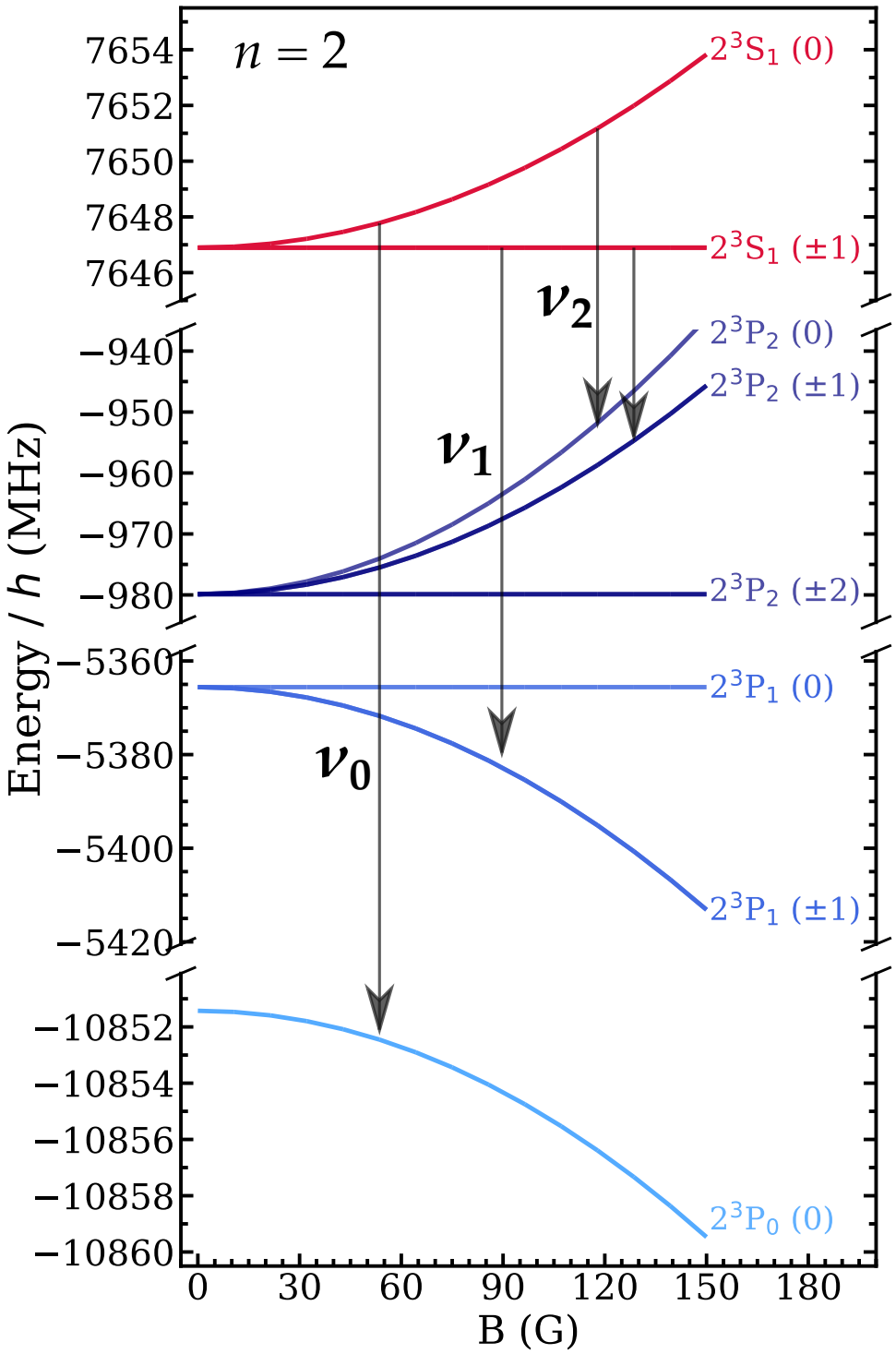

Figure 2.3: Zeeman structure of Ps in the 2^3S_1 and 2^3P_J states relative to the $n = 2$ Bohr (i.e., $\mathcal{O}(mc^2)$) level. The vertical grey lines indicate the allowed $\Delta M_J = 0$ transitions. The $2^3S_1(M_J{=}0) \rightarrow 2^3P_1(M_J{=}0)$ transition dipole moment is zero because it is not allowed. The $2^3S_1(\pm1)$, $2^3P_2(\pm2)$, and $2^3P_1(\pm0)$ states do not shift as explained in the text. The singlet states are not shown for clarity.

the microwave radiation polarisation is parallel (perpendicular) to the z-axis, only $\Delta M_J = 0$ ($\Delta M_J = \pm 1$) transitions can occur as shown in figure 2.3.

The transition dipole moments for transitions between $|nSlJM_J\rangle$ and $|n'S'l'J'M'_J\rangle$ substates can be expressed as

$$M_{n'S'l'J'M'_J,nSlJM_J} = (-1)^{J-M_J}\sqrt{(2J+1)(2J'+1)} \times \begin{pmatrix} J & 1 & J' \\ -M_J & \Delta M_J & M'_J \end{pmatrix} \begin{Bmatrix} l & J & S' \\ J' & l' & 1 \end{Bmatrix} \left\langle n'l' \middle| er \middle| nl \right\rangle. \tag{2.10}$$

The shift of the $2^3S_1 \rightarrow 2^3P_J$ energy intervals due to the Zeeman and Stark effects are shown in figure 2.4 and figure 2.5 respectively. Fermi's golden rule states that the transition strength is proportional to the square of the dipole moments and the relative transition strengths are indicated in figure 2.4 and figure 2.5. It can be seen that the shift in the transition frequencies due to the Zeeman effect can be positive or negative, whereas the Stark effect always results in a positive shift.

The structure of the microwave guide set the polarisation of the microwave radiation to be parallel to the external magnetic field, thereby, allowing only $\Delta M_J = 0$ transitions as determined by the selection rules. The transition dipole moment for $2^3S_1(M_J{=}0) \rightarrow 2^3P_1(M_J{=}0)$ is zero because it is not allowed. The number of transition pathways (satisfying the $\Delta M_J = 0$ condition) for the ν_0, ν_1, and ν_2 transitions are 1, 2, and 3 respectively.

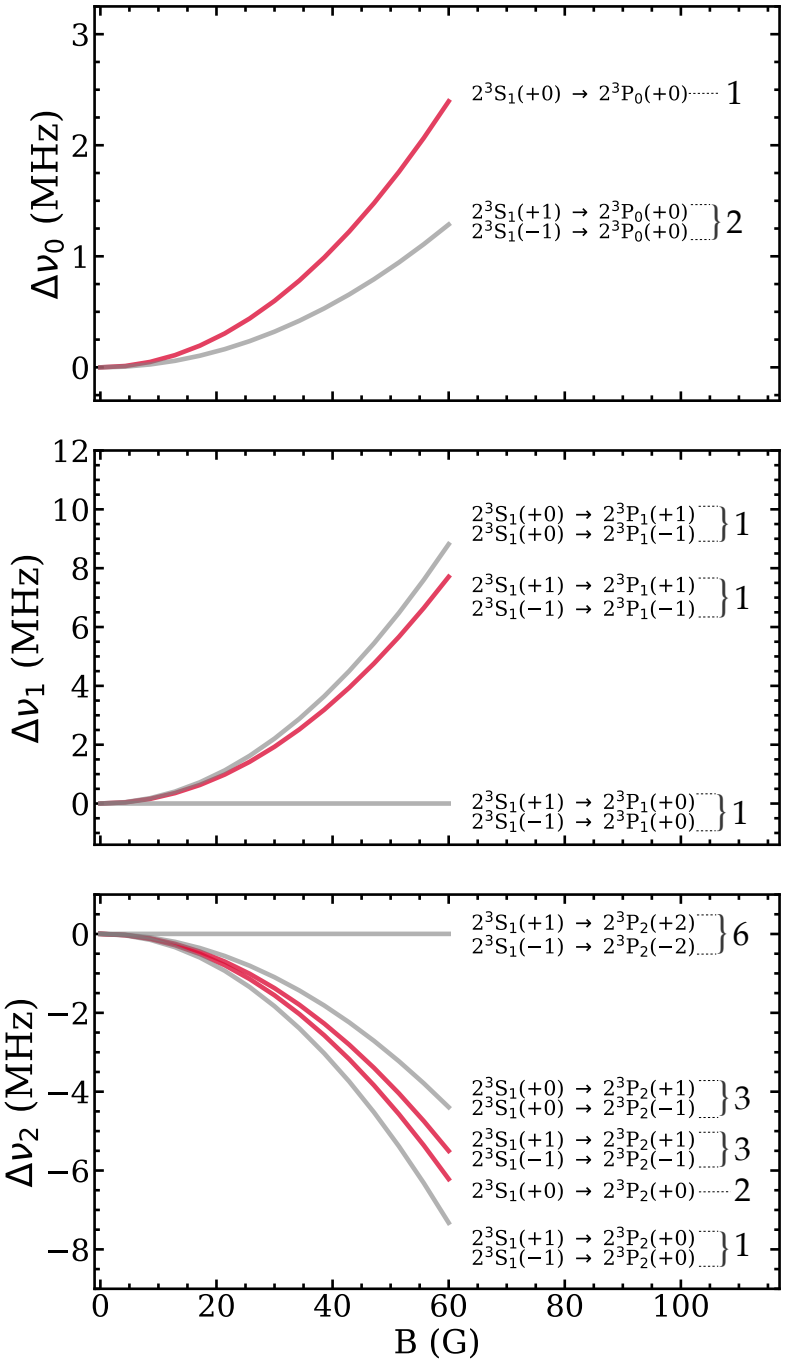

Figure 2.4: Microwave resonance frequency shifts for the ν_0, ν_1, and ν_2 as a function of the magnetic field. The red and the grey lines indicate the $\Delta M_J = 0$ and the $\Delta M_J = \pm 1$ transitions respectively. The transition strengths relative to the weakest transition for each ν_J are also indicated by the numbers next to the transitions.

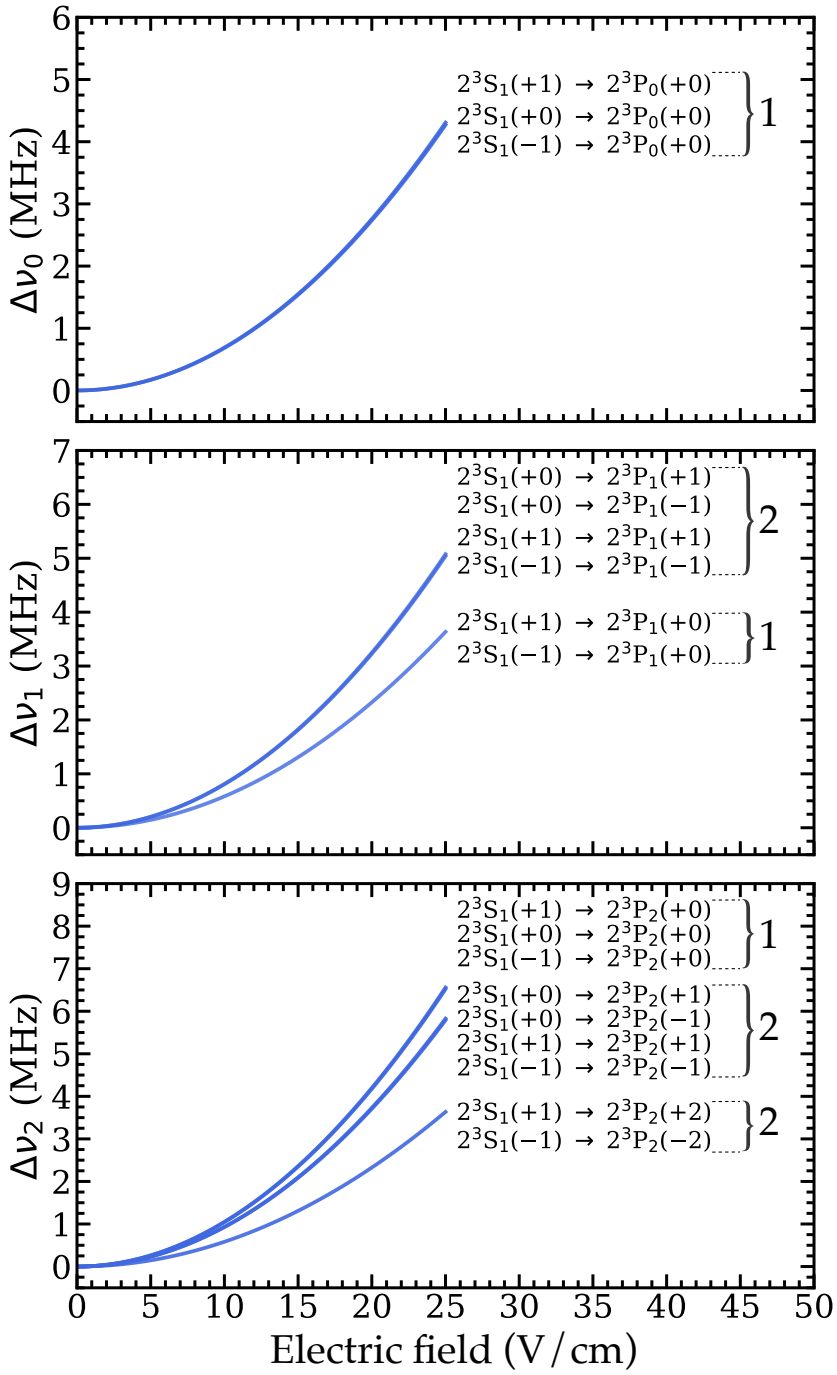

Figure 2.5: Stark shifts in ν_0, ν_1, and ν_2 transition as a function of the electric field, with the relative transition strengths. Both $\Delta M_J = 0$ and $\Delta M_J = \pm 1$ transitions are shown with the relative transition strengths.

Chapter 3

Experimental Methods

3.1 Outline of Apparatus

The methodology described in chapters 3.2, 3.3, 3.4, 3.5, 3.6, and 3.8 were already developed by the previous members of the group. The author of this thesis developed a microwave spectroscopy technique described in chapter 3.7 and combined it with the existing methodology to obtain the results presented in this thesis.

A 1.6 GBq radioactive ^{22}Na source, which produces positrons via β^+ decay, was moderated using neon (Ne) gas frozen onto a conical aperture. The moderated positrons were accumulated in a Surko-type buffer gas trap where they lost some of their energy via collisions with a mixture of N_2 and SF_6 gas. The positrons were then ejected from the trap and compressed temporally to a $\Delta t \approx 4$ ns (FWHM) pulse with a buncher and transported magnetically to the target chamber which contained a target material used to create positronium. Ortho-positronium atoms emitted from the SiO_2 target were excited using pulsed dye-lasers to generate metastable 2^3S_1 atoms. The atoms then entered a microwave guide where transitions to 2^3P_J (J = 0,1,2) state were driven via stimulated emission, and subsequent annihilation of the 1^3S_1 atoms were detected by gamma-ray detectors via the process: $2^3S_1 \rightarrow 2^3P_J \rightarrow 1^3S_1 \rightarrow 3\gamma$. A schematic of the positron beamline is illustrated in figure 3.1.

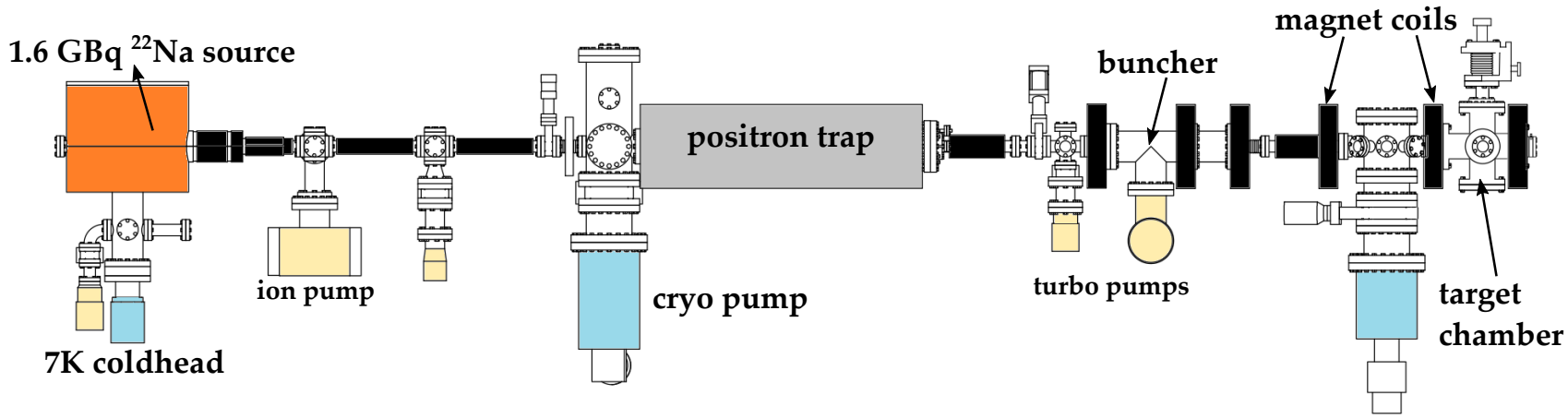

Figure 3.1: A schematic of the positron beamline showing the ^{22}Na radioactive positron source, Surko trap and the target chamber. Positrons emitted from the source were accumulated in the positron trap. The trap was operated at a rate of 1 Hz, ejecting a positron pulse towards the target chamber, where positronium atoms were produced and optically excited.

3.2 Positron Moderation

Positrons (e^+ or β^+) are generated from nuclear decay of a radioactive ^{22}Na source (intensity of $\approx$ 1.6 GBq). ^{22}Na has a half-life ($t_{1/2}$) of $\approx$ 2.6 years and decays into ^{22}Ne via positron emission (90%) or electron capture (10%). β^+ emitting nuclides, however, have a large energy spread, and ^{22}Na has an average and endpoint energies of $\approx$ 0.2 and 0.5 MeV respectively. Therefore, it was necessary to use a moderating material [103] to produce a slow positron beam. The process of generating a slow, usable positron beam is called moderation.

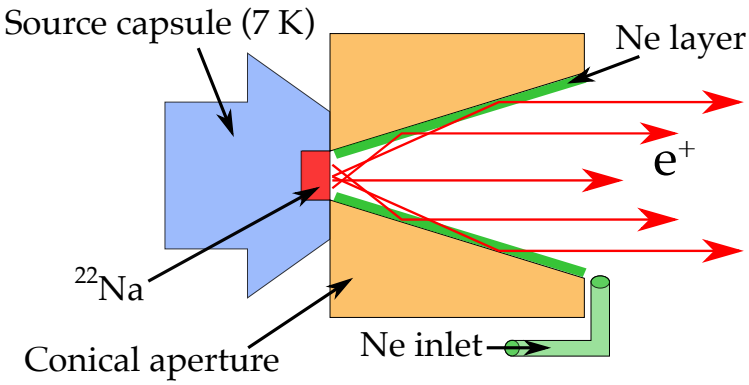

Figure 3.2: A simplified schematic of the source capsule, ^{22}Na source, conical aperture, and the solid Ne layer that is formed after injecting Ne gas into the region. The system temperature was held at 7 K and the pressure of the Ne gas was monitored with an ion gauge. The positron yield was monitored with a NaI detector.

A typical positron moderation process began by slowly admitting highly pure neon (Ne) gas [104], at pressure of $\approx 10^{-3}$ mbar, into a region containing a conical aperture [105]. The aperture was located in front of a source capsule (containing a ^{22}Na source) as shown in figure 3.2. The system was connected to a closed cycle helium cryostat and the temperature was held at 7 K. After injecting the Ne gas for $\approx$ 4 minutes, a solid layer of Ne was created on the surface of the cone. The positron yield was monitored with a sodium iodide (NaI) scintillator located near the entrance of the positron trap (section 3.3).

Inelastic collisions with the Ne layer reduces the energy of the positrons and

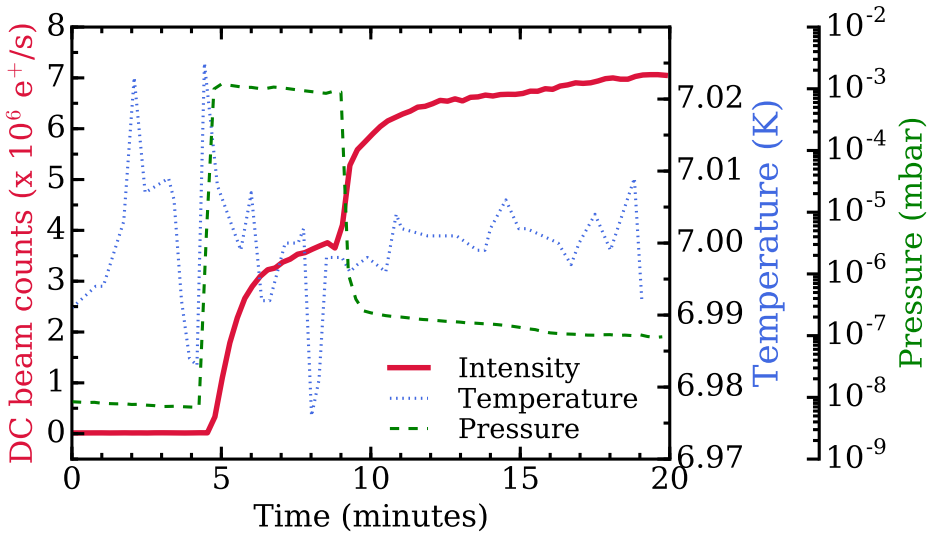

Figure 3.3: A graph showing the process of a moderator growth where the positron yield (solid line) is shown to increase when Ne is frozen on to the aperture at a constant pressure (green dashed line) and temperature of 7 K (blue dashed line). After the initial saturation occurred, the flow of Ne gas was stopped to further increase the positron yield.

once the positron yield saturated, the flow of Ne gas was stopped. The positron yield then started to rise further due to reduced attenuation from the excess Ne gas. An example of the moderation procedure is shown in figure 3.3. Taking the solid angle of the NaI detector into account, the total number of positrons in the moderated DC beam after $\approx$ 20 minutes was $\approx 7\times10^6$ s^{-1}, which equates to moderation efficiency of $\approx$0.5%. During the course of the next few days, the efficiency rose further to $\approx$1%. A typical moderator lasted approximately one month i.e., the positron yield was constant over the period. To regrow the moderator the old Ne layer was evaporated and the procedure outlined above was repeated.

3.3 Positron Trap

Much of the advancement in positronium physics in the last decade has been possible due to the development of positron trapping in Surko-type buffer gas traps [106] enabling short, intense pulses of positrons to be generated.

After emerging from the moderator, the DC positron beam entered a two-stage

Surko-type buffer gas trap [56]. The trap (First Point Scientific Inc.) contains a set of cylindrically symmetric electrodes and an inlet for the gas molecules. The positrons lose some of their energy via electronic excitation of N_2 [107, 108] and vibrational excitation of SF_6 molecules [109]. The positron trap was housed inside a solenoid, which provided a flat magnetic field of $\approx$ 500 G, to radially confine the positrons.

Varying electric potential biases applied to the electrodes in the trap, as shown in figure 3.4, ensured that the positrons experienced gradually deeper potential wells as they traversed the trap. The positrons were then accumulated at the end of the trap using a potential barrier $\approx$ 50 V in magnitude, which prevented them from escaping. The pressure in the second stage of the trap was lower than the first stage because of larger radius electrodes and as a result the positron lifetime against annihilation is higher.

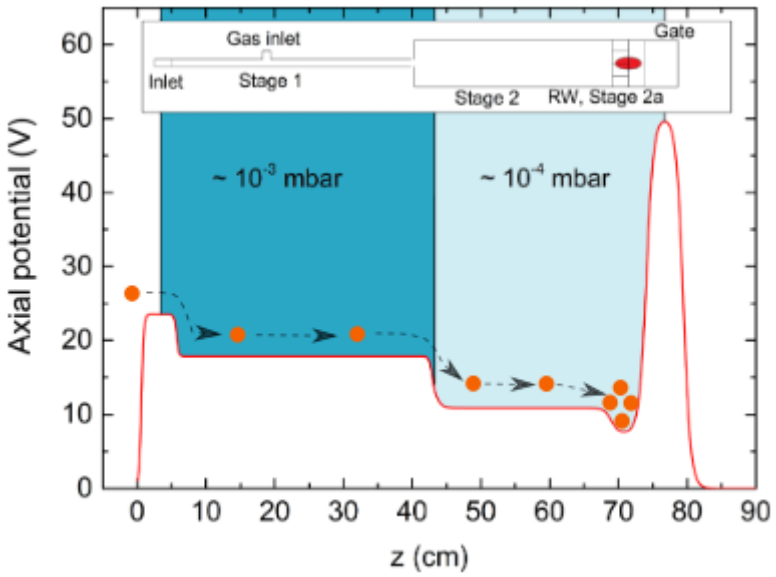

Figure 3.4: The electric potential and corresponding schematic diagram of a two-stage Surko trap where a DC positron beam entered from the left and was accumulated at the end of stage 2. The RW was located at the end of stage 2. Adapted from [15].

At the end of the second stage, a rotating wall (RW) quadrupole electric field compressed the positrons radially inwards, reducing the positron spot size as a res-

ult. This prevented the positrons from colliding with the chamber walls, further increasing their annihilation lifetimes [61, 109]. The lifetime of the positrons was then mainly limited by the interaction with the gas molecules.

The output signal from the trap, with the RW off and on, as a function of accumulation time is shown in figure 3.5. The two data sets are fitted with the function:

$$N_{e^+}(t) = A(1 - e^{-t/\tau}), \tag{3.1}$$

where τ is the positron lifetime in the second stage of the trap, $A = R\tau$, and R is the positron capture rate. The positron lifetimes with the rotating wall was off and on were measured to be (0.13 ± 0.09) s and (1.72 ± 0.07) s respectively. As seen in figure 3.5, the trapped positron yield saturated after ≈ 2 s accumulation time, setting a lower operation limit of 0.5 Hz. In our measurements the trap was operated at 1 Hz, which was synchronised with the pulsed dye lasers also operating at 1 Hz.

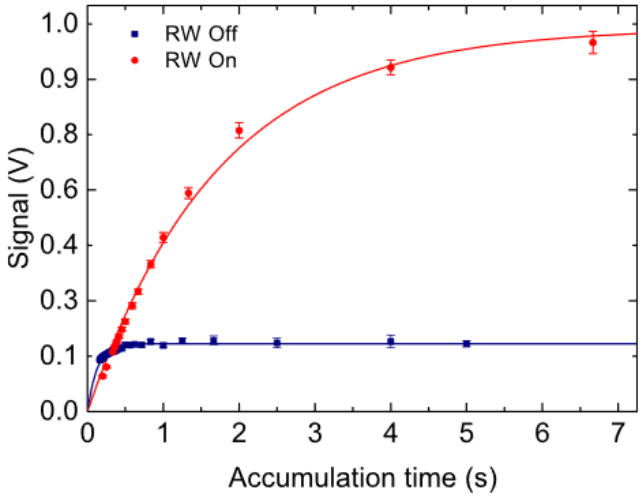

Figure 3.5: Positron pulse signal as a function of accumulation time in the trap. These data sets are fitted with equation 3.1. The application of the RW on the trapped positrons increased the lifetimes against annihilation. From [15].

Once accumulated at the end of stage 2 inside the gas trap, the positron pulse (which contained $\approx 10^6$ positrons) was ejected by lowering the trap gate potential via a trigger pulse. As the potential applied to the last electrode of the trap (≈ 50

V) does not provide enough energy to the positrons and the temporal width of the positron pulsed would widen as a result during the transport to the target chamber, a high voltage (HV) buncher was utilised to compress the temporal width of the positron pulse. Shortly after exiting the trap, the positron pulse was compressed temporally to a width (FWHM) of $\approx$ 4 ns by a parabolic potential applied by a HV buncher [110]. The positrons were then magnetically guided to a Ps production region, located 1-2 m away from the buffer gas trap.

3.4 Positronium Production

The positron pulse output from the trap was magnetically transported to a chamber which contained a target material that converted the incoming positrons into positronium. The converter material used in our experiments was a mesoporous silica (SiO_2) target with 5 nm pore size [111], preferred for its ease of use and stability. A micro-channel plate (MCP) detector (Photonis), located behind the target material, allowed the positron beam to be imaged and a 2D intensity profile to be generated in order to measure the positron beam size [15].The spatial width (FWHM) of the positron pulse due to RW compression was measured to be $\approx$ 2 mm.

Mesoporous SiO_2 targets, depicted in figure 3.6, produce ortho-Ps with efficiencies of around 30%, and the atoms are emitted into vacuum with near thermal energies. The SiO_2 target was mounted on an electrode to control the positron implantation energy via the potential bias (V_T) applied on the electrode. The potential bias could be applied directly, or with a high-voltage (HV) switch which allows the user to control the input voltage and timing (section 3.8).

After implanting the positron pulse into the porous SiO_2 film at a certain energy the implantation profile on the positrons is defined by the Mahkovian profile [112]. This means that positron distribution is spread out inside the material with a certain mean stopping distance [113]. Some positrons thermalise and form Ps atoms in the bulk material, which then diffuse through the material until they reach an internal

surface i.e., pore walls. Here, the Ps is ejected into the 5 nm diameter pores with an energy of around 1 eV [114] and cool down by via collisions with the pore surfaces as shown in figure 3.6. The Ps atoms diffuse through the interconnected porous network of the film and are emitted into vacuum with energies on the order of 50 meV with a cosine distribution [115].

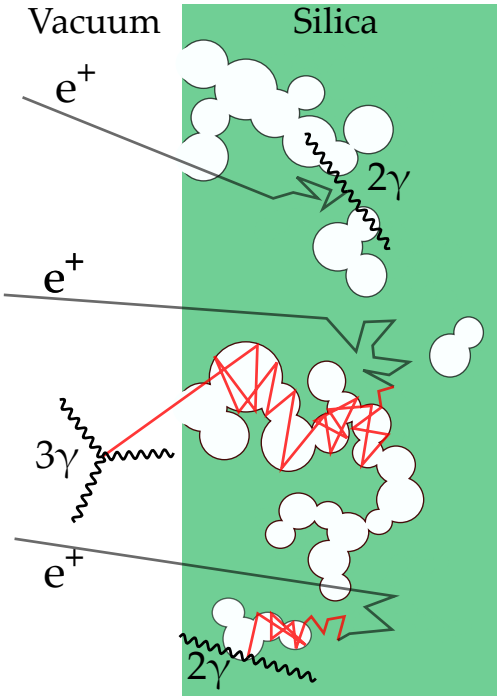

Figure 3.6: The three cases from top to bottom depict direct positron annihilation, ortho-Ps formation, and formation of para-Ps in mesoporous silica target respectively. About 30% of the incoming positrons formed ortho-Ps. The positron implantation depth was controlled by the potential bias applied to the target electrode. A deeper implantation resulted in higher number of collisions between the Ps and the SiO_2 walls.

Along with ortho-Ps formation positrons can also form the shorter-lived para-Ps in the SiO_2 target. The para-Ps atoms, however, annihilate in less than 1 ns, and so do most of the positrons by directly annihilating with electrons. Figure 3.6 shows these three cases following positron implantation in porous silica: direct annihilation of positrons, ortho-Ps formation, and para-Ps formation.

An additional reason for the selection of porous SiO_2 for Ps production was the ability to tune, albeit roughly, the energy of atoms emitted into vacuum. As the

positrons depth is spread out inside the SiO_2 film, the position of Ps formation is also spread out. The atoms that are formed deeper in the material take longer to be emitted and thus, experience a greater amount of collisional cooling. These atoms, although fewer in numbers, can be colder than 50 meV. Additionally, positrons implanted with higher energy have a deeper mean stopping distance and therefore, also undergo greater amount of collisional cooling [16, 57]. Atoms emitted from a silica target with 5 nm diameter pores can have minimum energies of around 30 meV. Figure 3.7 shows the reduction in energy of a Ps atom [116] in a SiO_2 pore of various diameter, and is an idealised case as the pores, in reality, have a distribution. In our measurements the transverse energy of the emitted atoms was $\approx$ 50 meV.

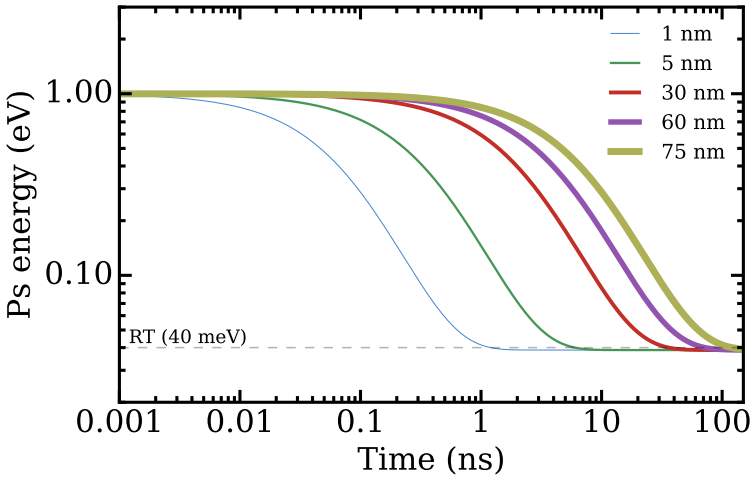

Figure 3.7: Cooling curves for Ps starting with 1 eV initial energy in a SiO_2 pore with various diameter. Pores with smaller diameter cool the Ps faster as the scattering length between collisions are shorter. These curves were generated from the model given in Ref. [116]

Positronium emitted from SiO_2 targets, however, are divergent: therefore, the associated Doppler broadening can limit the laser excitation efficiency. Even atoms emitted with transverse energy of $\approx$ 30 meV have a broad Doppler spread. To mitigate this effect the bandwidth of the UV laser was increased to achieve a greater excitation efficiency. Other materials such as smoked MgO were also used to produce Ps atoms, but the energies after emission into vacuum were even higher (approximately on the order of 300 meV) [7]. Ps atoms in MgO undergo collisional process

similar to SiO_2, but the large voids in MgO do not cool the atoms as effectively. Metal targets such as oxygen treated Al have also been shown to generate cold Ps, but require more care and maintenance [117]. In contrast, the SiO_2 targets used in this work are stable and do not require a great deal of maintenance.

3.5 Laser Systems

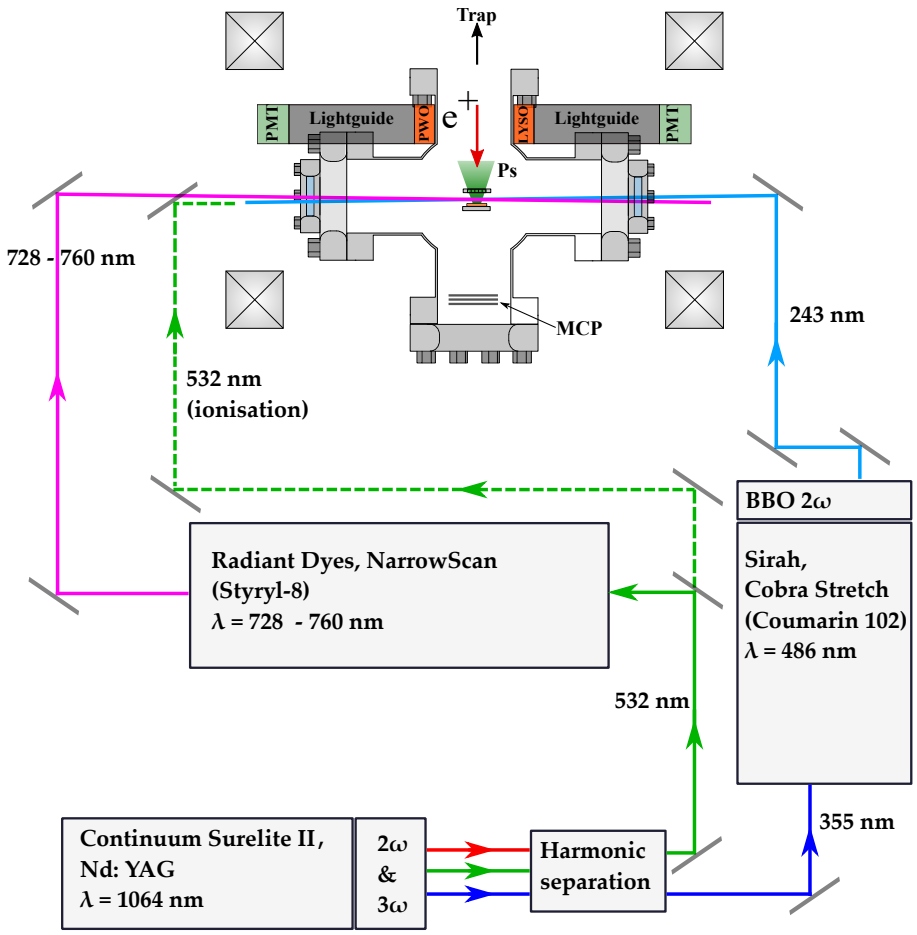

Figure 3.8: Schematic showing the laser setup and the target chamber including two gamma-ray detectors. The pulsed Nd:YAG laser pumped the two dye lasers to produce UV and IR radiation as explained in section 3.5. The four crossed squares around the target chamber depict the magnet coils shown in figure 3.1.

Positronium generated by SiO_2 films are created in the ground state. To produce excited states two pulsed dye lasers (pumped by a neodymium-doped yttrium aluminium garnet (Nd:YAG) laser (FWHM $\approx$ 5 ns) at a rate of 1 Hz) were used.

Similar to the method used in Ref [55], we employed a two-colour, two-photon (i.e., $1^3S_1 \rightarrow 2^3P_J \rightarrow n^3D_J/n^3S_J$) excitation scheme where n ranged from 8 to the ionisation potential. A schematic diagram of the laser systems and their interaction with the apparatus is shown in figure 3.8. A trigger pulse, with adjustable timing controlled via LabVIEW software, was sent to the Nd:YAG laser (Surelite II, Continuum) to control the timing of the laser pulse as shown in figure 3.11(a). The wavelength of the light from the dye lasers was also controlled via LabVIEW software and recorded by the data acquisition (DAQ) system.

To facilitate the first step of the excitation scheme, $1^3S_1 \rightarrow 2^3P_J$, a dye laser (Cobra Stretch, Sirah), operated using Coumarin 102 dye, was pumped by the third harmonic (λ = 355 nm) of the Nd:YAG laser. This tunable dye laser produced photons with λ = 486 nm, which were then frequency doubled in a barium borate (BBO) nonlinear optical crystal to produce λ = 243 nm ultraviolet (UV) light pulses with energy of $\sim$1 mJ. The UV laser pulse had a spectral FWHM bandwidth of $\Delta\nu \approx$ 100 GHz. The broad bandwidth was required to achieve a more efficient excitation of the emitted Ps ensemble which has a large Doppler spread.

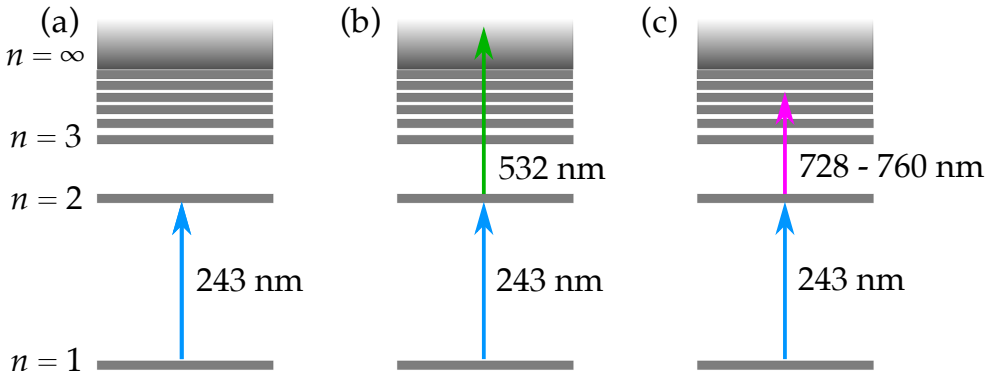

Figure 3.9: Ps optical excitation schemes as described in section 3.5. (a) $1^3S_1 \rightarrow 2^3P_J$ transition with 243 nm photons. (b) $1^3S_1 \rightarrow 2^3P_J$ transition with 243 nm photons and subsequent photoionisation using 532 nm light. (c) $1^3S_1 \rightarrow 2^3P_J \rightarrow n^3S_J/n^3D_J$ transition to Rydberg states with $n = 8 - \infty$. The $1^3S_1 \rightarrow 2^3S_1$ transition can be achieved in (a) in the presence of an external electric field as explained later in section 3.8.

The second harmonic (λ = 532 nm) of the Nd:YAG laser was used to pho-

toionise atoms in 2^3P_J state, or to pump a second dye laser (NarrowScan, Radiant Dyes) as illustrated in figure 3.8. This dye laser was operated using Styryl-8 dye to produce infrared (IR) light with λ = 728-760 nm with energy of ≈10 mJ. The resulting IR radiation pulse was used to either photoionise $n = 2$ atoms, or drive the $2^3P_J \rightarrow n^3D_J/n^3S_J$ Rydberg transitions with $n = 8 - \infty$. These excitation schemes are illustrated in figure 3.9. The $1^3S_1 \rightarrow 2^3S_1$ transition, although forbidden for a single photon due to electric dipole selection rules, can still be driven with the UV laser if performed in an electric field. This technique is discussed in detail in section 3.8.

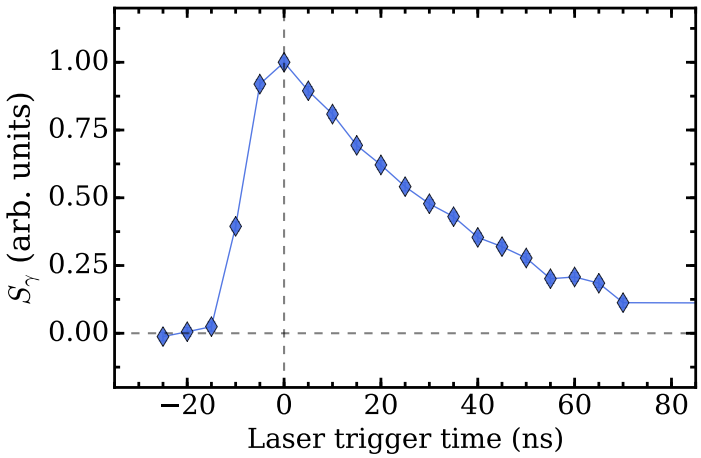

Figure 3.10: Example of a laser delay scan to find the optimal overlap between the positronium beam and laser pulses. To get the laser induced signal (section 3.6), the excitation scheme in figure 3.9(b) was utilised. The trigger times have been plotted relative to the optimal time (i.e., highest S_γ). For delayed trigger times, the laser excited slower atoms that take longer to be emitted into vacuum.

After the positronium atoms were emitted from the SiO_2 target, optimal overlap between the atoms and laser pulse was determined. A time adjustable trigger pulse, generated from a signal generator and controlled by the DAQ system, sent to the Nd:YAG laser (see section 3.6) was scanned across to find the optimal overlap between the Ps atoms and the laser radiation. This process is shown in figure 3.10, which is essentially a representation of the distribution of the Ps emission time from the SiO_2 film. S_γ is the laser induced signal parameter, and is explained in greater detail in the next section. For our measurements the laser trigger time was set to the

optimal delay for higher signal-to-noise ratio (SNR), and the transverse energy of the atoms probed at this optimal time was found to be ≈ 50 meV.

It can be seen that some signal is still present even 40 ns after the optimal time. The signal at late trigger times are due to some Ps atoms, formed deeper in the target, that take longer to be emitted into vacuum as explained earlier in section 3.4. Delaying the trigger to the laser can result in excitation of these slower atoms, resulting in transverse energies of approximately 30 meV, but also lower SNR.

3.6 Positronium Detection: SSPALS

Positronium produced by the SiO_2 target after positron implantation eventually annihilate either by self-annihilation, photoionisation by a laser, or due to collisions with the vacuum chamber walls. During the photoionisation process the liberated positrons were attracted to the negatively biased target electrode resulting in excess annihilation. The γ-rays emitted from these annihilation events were detected by γ-ray detectors placed outside the vacuum chamber as shown in figure 3.8.

A typical gamma-ray detector used in these measurements was a scintillator optically coupled to a photo-multiplier tube (PMT) via an acrylic light guide. The time dependent detector anode voltage output was divided into two channels using a 50 Ω splitter and coupled to a digital oscilloscope (HD 04014, Teledyne Lecroy). The early parts of the signal, which were generally higher in amplitude and contained direct annihilation events, were recorded with low scope gain in order to avoid saturation. The later parts of the detector signal have lower amplitudes and were recorded with high gain to minimise electronic noise. Using only one oscilloscope channel to record the detector output added electronic noise in the later parts of the spectrum, which is typically a region of interest when searching for excited state Ps. The high and low gain signals were then recombined to form a lifetime spectrum and analysed with the single shot positronium annihilation lifetime spectroscopy (SSPALS) method [118].

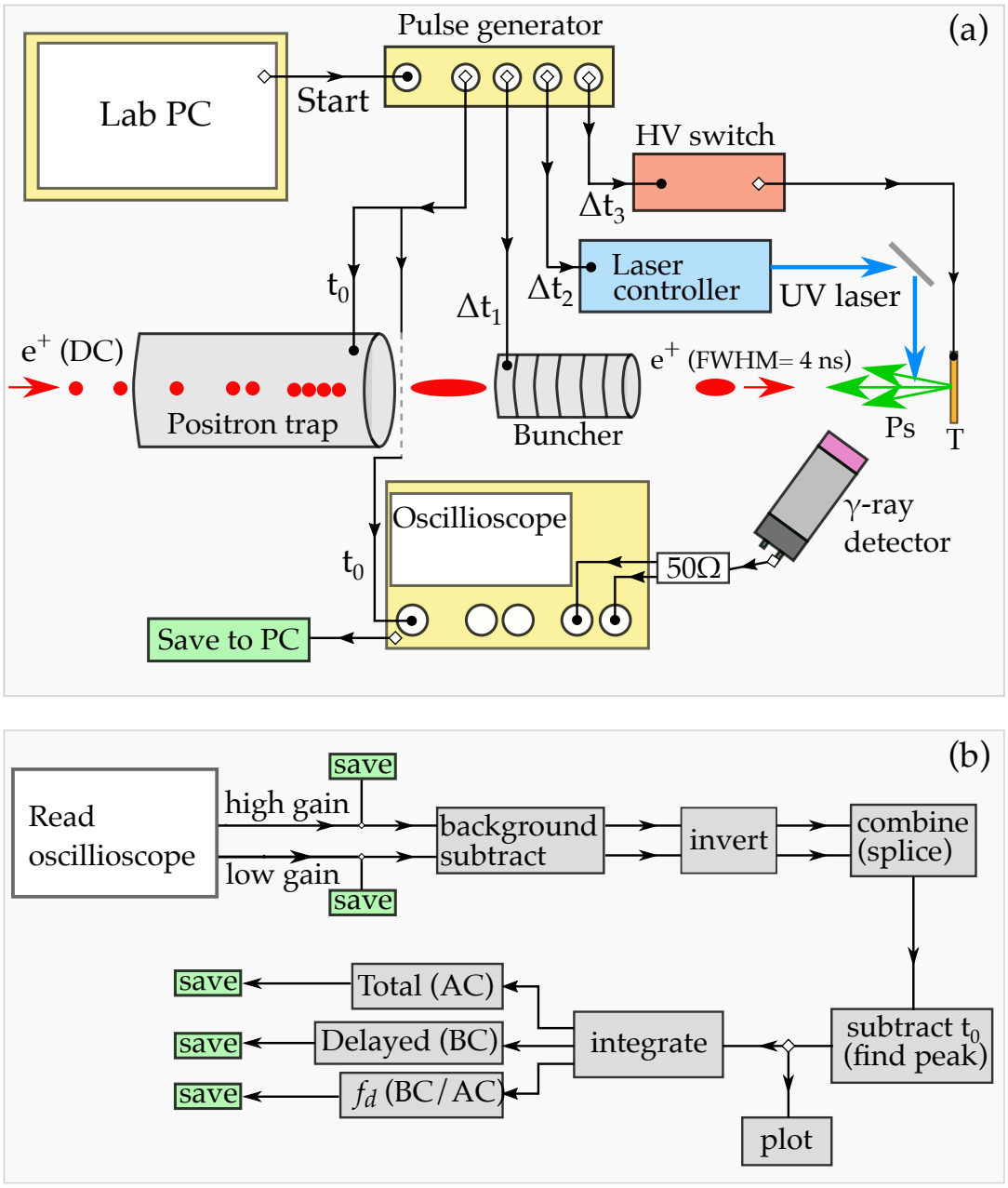

Figure 3.11: (a) Schematic of the DAQ system. Data acquisition was initiated by the PC and the pulse generator sent trigger pulses to various terminals in sequence at 1 Hz. Signal from the oscilloscope as well as parameters such as wavelength from the laser controller and target bias were recorded and saved to the PC. The HV switch took two input: a trigger pulse and a potential bias, and its operation is explained in section 3.8. (b) Schematic showing the analysis of the gamma-ray detector signal to generate lifetime spectra.

A schematic representation of the DAQ system and SSPALS analysis is illustrated in figure 3.11(a). The DAQ process was initiated by the main computer

(PC) and a pulse generator sent trigger pulses sequentially to the positron trap (+ oscilloscope), buncher, Nd:YAG laser, and a HV switch connected to the target (section 3.8). All of these instruments were triggered at a rate of 1 Hz as explained earlier. Gamma-ray signal from the detectors were recorded by the oscilloscope and saved to the PC as shown in figure 3.11(b).

The scintillator used was selected depending on the process being studied, but a lead tungstate ($PbWO_4$, henceforth abbreviated PWO) scintillator (attached to a Hamamatsu H10570 PMT) with its high γ-ray stopping efficiency arising from its density (8.3 gm/cm^3, decay time of $\approx$12 ns) [119] was utilised to quantify the amount of Ps present. As the PWO is a relatively fast detector, the earlier events like direct annihilation of positrons were well defined. A lutetium yttrium oxyorthosilicate (henceforth abbreviated LYSO) scintillator (attached to a EMI type 9954KA PMT) based detector [12] was also used in our experiments. Although the LYSO detector has a relatively long decay time of $\approx$40 ns, it has higher light output and the signal to noise ratio (SNR) of data collected from LYSO was found to be $\approx$ 2-3 times higher compared to the PWO detector.

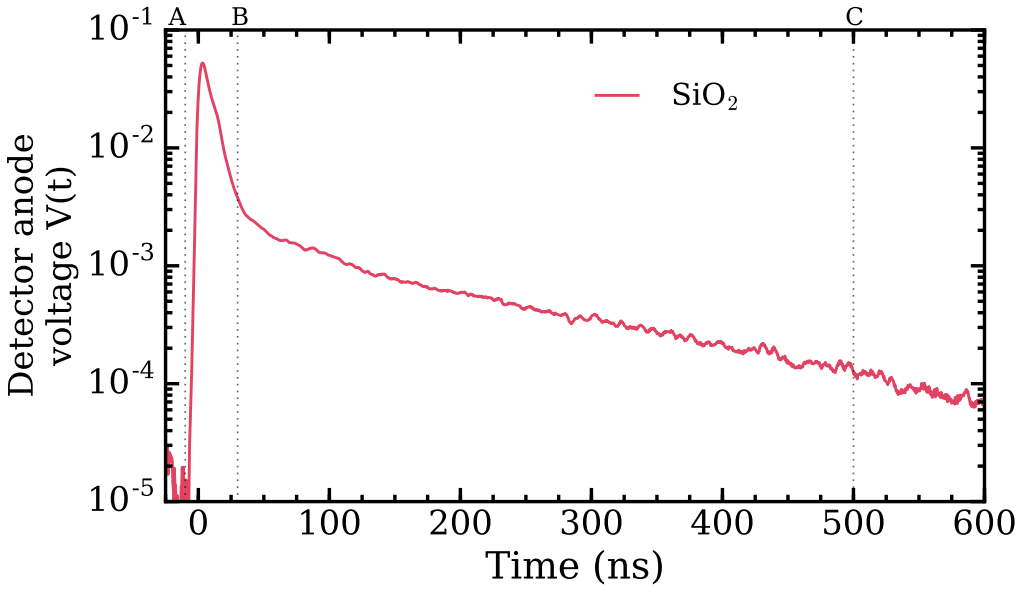

Figure 3.12: Lifetime spectra obtained from a SiO_2 target. The vertical lines indicate the SSPALS integration time windows *A*, *B*, and *C*. The spectrum was recorded using the PWO detector.

Figure 3.12 shows an example lifetime spectrum obtained from positron implantation into SiO_2 recorded by a PWO detector. The spectrum has two main features. There is an initial peak ('prompt peak'), which is due to the para-Ps annihilation and direct annihilation of positrons as well as some ortho-Ps annihilations. The width of the prompt peak is defined by the convolution of the positron pulse width and the detector decay time. The annihilation signal from short-lived para-Ps and positrons are not present after a short time period. After $\approx$ 30 ns the signal in the SiO_2 spectrum in figure 3.12 is due to the exponential decay (τ_{ann} = 142 ns) of the longer-lived ortho-Ps atoms.

To analyse the lifetime spectrum different regions of the spectrum were integrated to obtain a parameter f_{d}. Constraining the total measured lifetime spectrum in the region $A-C$, the prompt peak in region $A-B$, and delayed events in region $B-C$, we quantify f_{d} as:

$$f_{\text{d}} = \int_B^C V(t)\,dt \,/\, \int_A^C V(t)\,dt, \tag{3.2}$$

where $V(t)$ is the time dependent detector anode voltage function. f_{d} is proportional to the amount of ortho-Ps present in the SSPALS time windows selected.

The interaction of radiation with the Ps atoms will change f_{d}. Such changes can be accounted for by defining another parameter S_γ as:

$$S_\gamma = \frac{f_{\text{off}} - f_{\text{on}}}{f_{\text{off}}}, \tag{3.3}$$

where f_{off} and f_{on} are the background and signal measurements of f_{d} respectively. The definitions of f_{off} and f_{on} are dependent on the process being studied. For photoionisation from the $n = 2$ state f_{on} and f_{off} were defined to be the UV laser on and off $1^3\text{S}_1 \rightarrow 2^3\text{P}_J$ resonance respectively. For excitation to Rydberg states f_{on} and f_{off} were those measured by the IR laser on and off resonance with the $2^3\text{P}_J \rightarrow n^3\text{D}_J/n^3\text{S}_J$ transitions respectively.

3.6.1 Events at Early Timescales

Different processes shift the population of Ps atoms to different times in the lifetime spectrum: therefore, the SSPALS time windows, (A, B, C), used to calculate f_d and S_γ were optimised depending on the process being studied as well as the detector in use.

When direct photoionisation effects were being studied, for example, the time windows used were approximately A= -30 ns, B=30 ns, C=600 ns (A= -30 ns, B=100 ns, C=600 ns) for the PWO (LYSO) detector. Early annihilation events result in excess signal at early times with a corresponding reduction in signal at late times. This can be clearly seen in figure 3.13(b) which shows the background subtracted spectra, i.e., "laser on" signal - "laser off" signal.

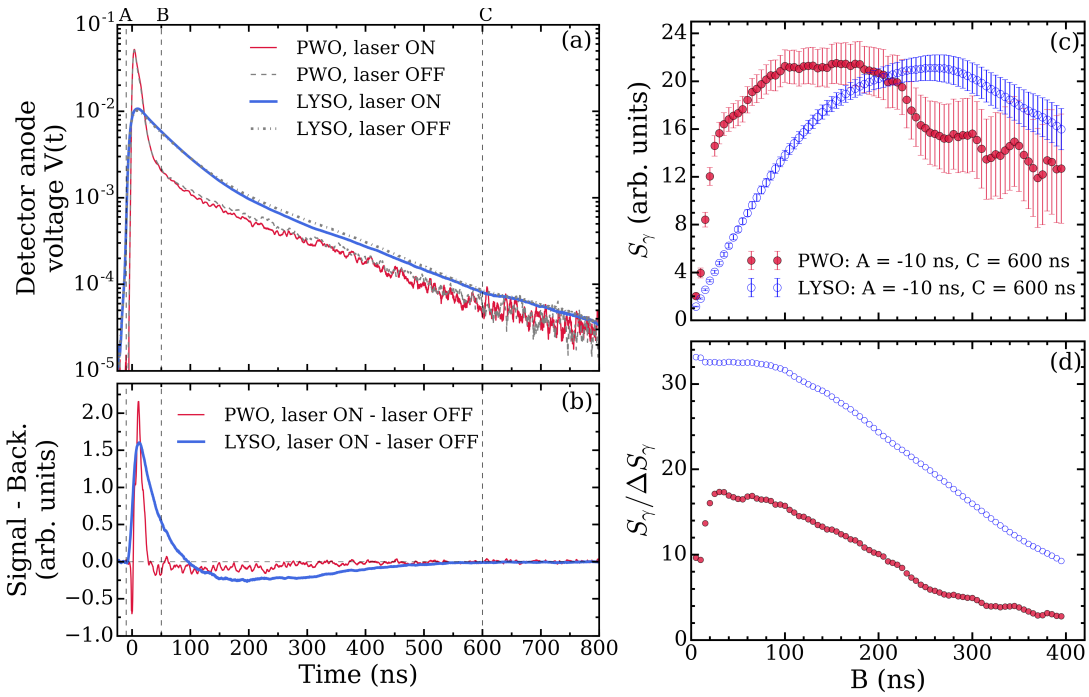

Figure 3.13: (a) Lifetime spectra with laser on and off $1^3S_1 \rightarrow 2^3P_J$ resonance recorded by PWO (red) and LYSO (blue) detector. After excitation to the 2^3P_J state, the Ps atoms were photoionised using the IR laser.(see figure 3.8) (b) Background subtracted (laser ON - laser OFF) spectra. S_γ (c) and $S_\gamma/\Delta S_\gamma$ i.e., SNR (d) as a function of the time B for fixed A and C times as indicated.

Constraining the entire spectrum within the bounds of A and C, the laser

radiation-induced signal S_γ, which has a statistical uncertainty of ΔS_γ, was optimised by scanning across the integration B parameter to find the time where the signal to noise ratio (SNR = $S_\gamma/\Delta S_\gamma$) was the highest. This procedure is illustrated in figures 3.13(c) and (d) for both PWO and LYSO detectors. For the LYSO example data the value of B corresponding to the highest SNR was $\approx$ 100 ns, which is crudely the time when the spectra in figure 3.13(b) transitions from positive to negative. For early annihilation events such as photoionisation S_γ has a positive value.

3.6.2 Events at Late Timescales

Excitation to long-lived states such as Rydberg levels or the metastable 2^3S_1 state have a different effect on the lifetime spectra compared to short-lived effects like photoionisation. Due to the long lifetime of Rydberg states an increase in signal is seen in the later part ($B - C$) of the spectrum and this can be seen in figure 3.14(a), which shows an example lifetime spectra of Ps atoms excited to the $n = 15$ state.

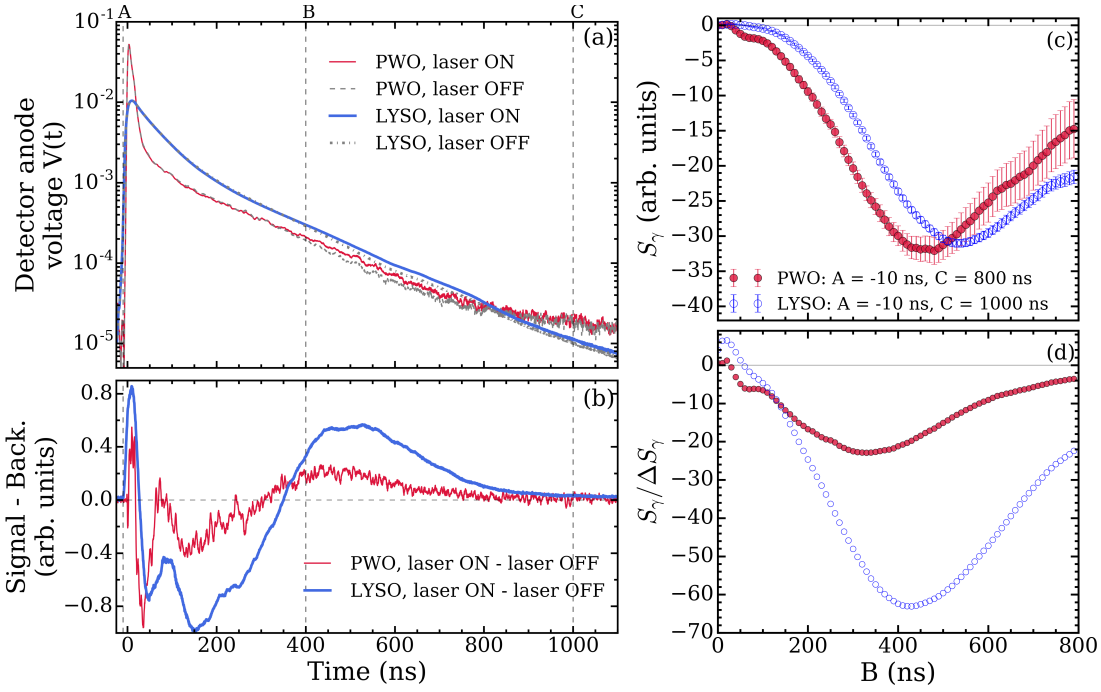

Figure 3.14: (a) Lifetime spectra with laser on and off $2^3P_J \rightarrow 15^3D_J/15^3S_J$ resonance recorded by PWO (red) and LYSO (blue) detector. (b) Background subtracted (laser ON - laser OFF) spectra. S_γ (c) and $S_\gamma/\Delta S_\gamma$ i.e., SNR (d) as a function of the time B for fixed A and C times as indicated.

These late annihilation events are clearly seen in the background subtracted spectra in figure 3.14(b) where the peak around 500 ns corresponds to Rydberg atoms annihilating due to collisions with the vacuum chamber. The earlier peak at ≈100 ns is due to atoms annihilating upon collisions with the grid electrode. Again, the value of the integration time parameter B was scanned to find the optimal SNR as shown in figures 3.14(c) and (d). The presence of the positive annihilation signal in the region $B-C$ of the background subtracted spectrum results in a negative value of S_γ.

3.7 Microwave Guide System

The pulsed positron output from the buffer gas trap was magnetically transported to the target chamber where positronium atoms were produced and subsequently excited as described in section 3.4 and 3.5. The layout of the target chamber including the γ-ray detectors and magnets is shown in figure 3.15 and figure 3.16.

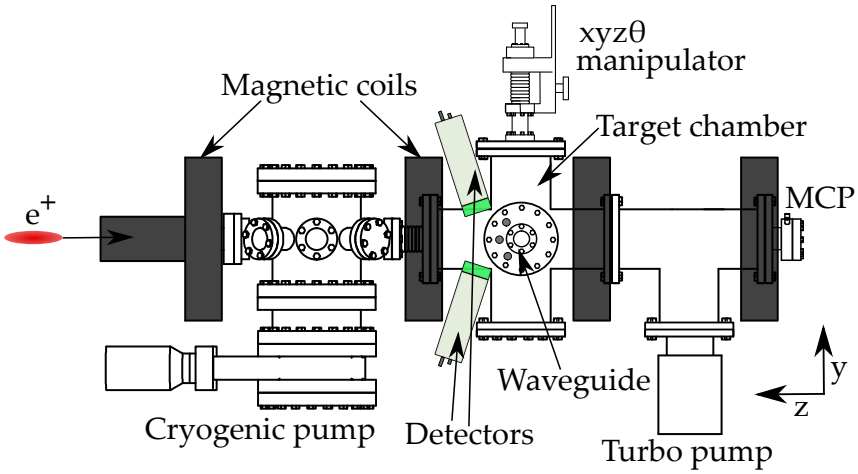

Figure 3.15: Target chamber schematic showing the position of the magnetic coils, target manipulator, and the detectors. The waveguide was mounted on a 6" flange and inserted through the side port of the target chamber. The two magnet coils around the target chamber were not in Helmholtz configuration as they were separated by more than the coil radius.

Following the laser excitation to the 2^3S_1 state (section 3.8), the metastable atoms entered a waveguide where the $2^3S_1 \rightarrow 2^3P_J$ transitions were driven with microwave radiation (as explained later in section 3.9). Three different waveguides

(differing only in their dimensions) were utilised to probe the three different fine structure intervals. The waveguides were designed using computer-aided design (CAD) software (Autodesk Inventor) and fabricated in-house. The waveguide was mounted on a 6" flange and inserted into the target chamber through a side port. The SiO_2 target, placed behind the waveguide, was attached to an electrode and a manipulator. A UV viewport on either side of the target chamber allowed the UV laser to enter the excitation region between the waveguide and the target. Detailed drawings of an example of a microwave guide used in the measurements are also shown in figure 3.17 and figure 3.18. The microwave-radiation-induced signal, S_γ, was then measured as a function of the applied microwave radiation frequency to yield a fine structure transition lineshape (presented later in section 4.1).

Two coils were placed around the target chamber and the resulting magnetic field, accounting for the field contributed by the coils used for transport of the beam, was measured using a Hall probe with 1% accuracy. The measurements reported here were performed in an axial magnetic field which was varied from $\approx$ 20-100 G. Variation of the field within the spatial region encompassing the waveguide were found to be no more than ± 1 G, which was defined as the uncertainty in the field determination. Fields lower than 20 G could not be used to due to difficulty in beam transportation, while fields higher than 100 G were beyond the capability of the magnets.

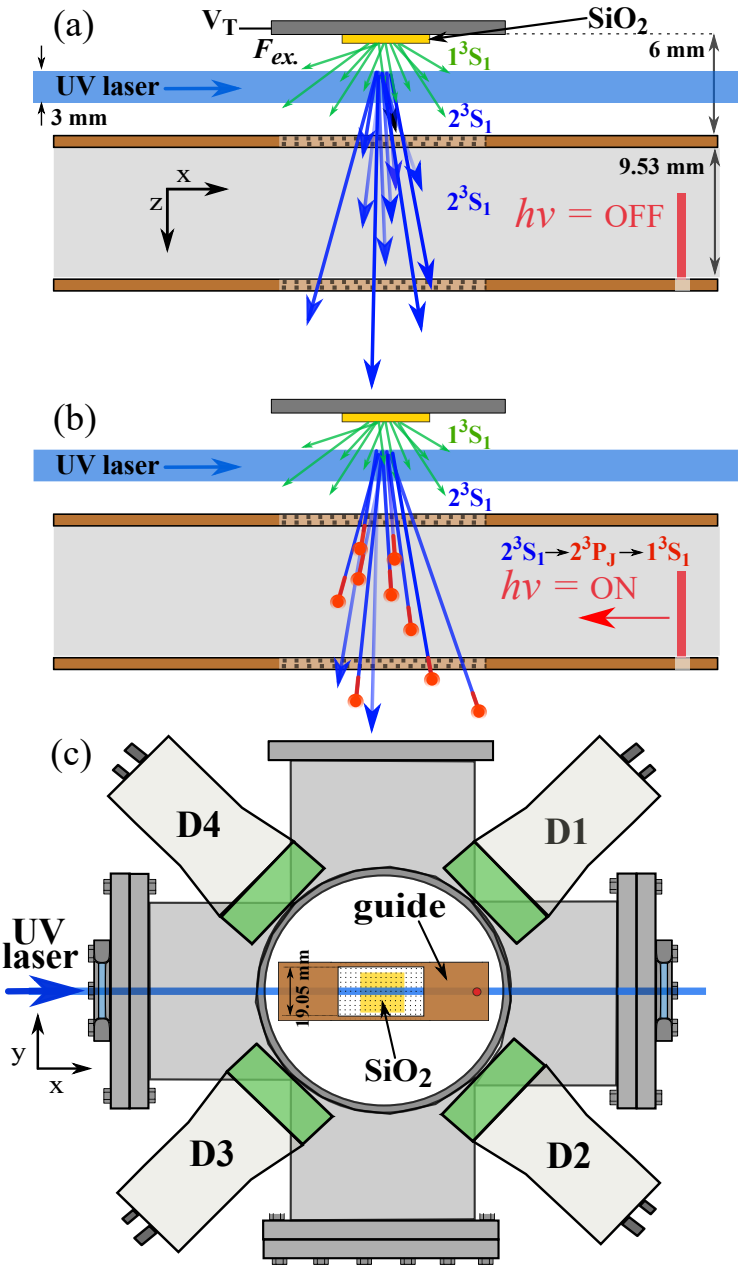

Figure 3.16: Schematic of the Ps target, UV laser, and a WR-75 microwave guide with microwave radiation off resonance (a) and on resonance (b). A potential bias of 3.5 kV was applied to the target electrode (V_T), generating an electric field of $F_{ex.}$ = 5.8 kV/cm in the laser excitation region. (c) The placement of the four LYSO detectors around the target chamber. After the microwave induced transition, annihilations of some of the 1^3S_1 atoms occurred outside the waveguide and this is represented by the conversion from an arrow to a solid circle in the depicted flight paths in (b).

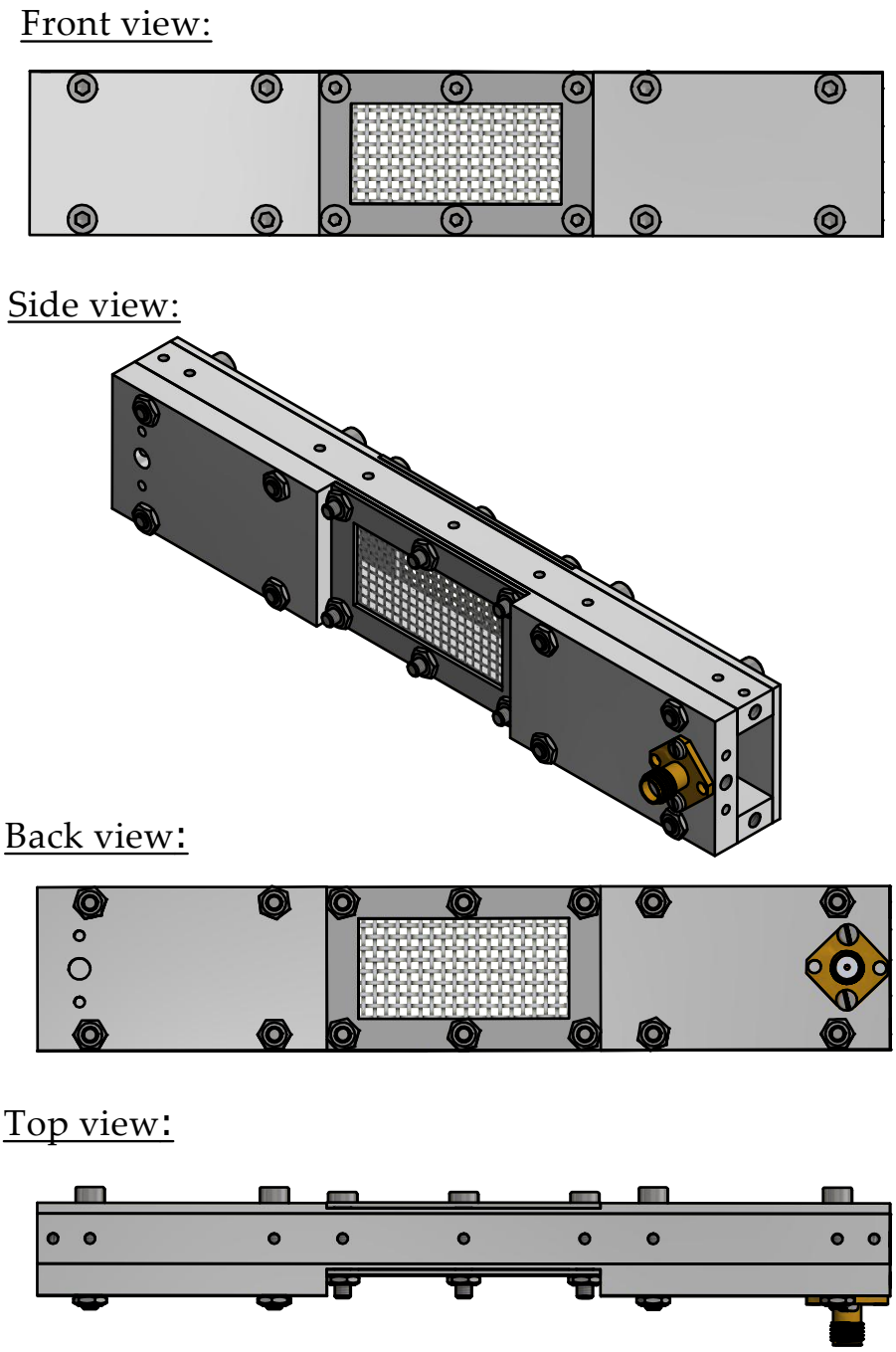

Figure 3.17: CAD drawing of an example microwave guide. The individual components were machined from aluminium, and the tungsten mesh (95% open area) allowed the transmission of the positrons and Ps atoms. The waveguides were grounded throughout the measurements. The microwave radiation was fed into the waveguides via a SMA antenna.

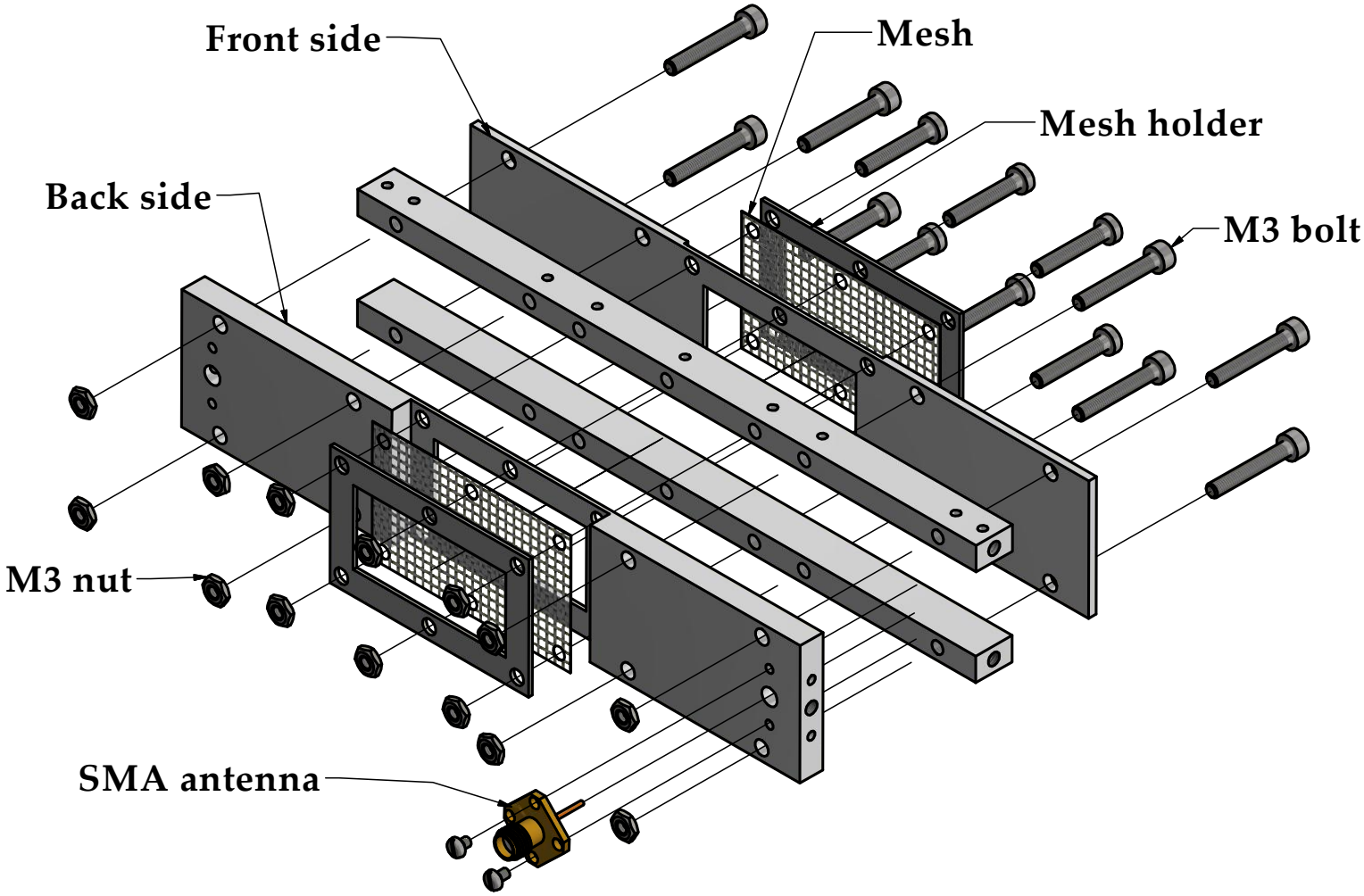

Figure 3.18: Exploded CAD drawing of an example microwave guide. All three waveguides were designed and fabricated in-house and only differ in their dimensions.

For a rectangular waveguide with dimensions a and b (as shown in figure 3.19), both transverse electric (TE) and transverse magnetic (TM) modes can propagate, but transverse electromagnetic (TEM) modes are not allowed. For TE waveguide modes the electric field in the direction of propagation (i.e., x axis) is zero by definition, $E_x = 0$. The remaining TE_{mn} mode field components can be expressed as

$$E_y \propto A_{mn} \cos\frac{m\pi y}{a} \sin\frac{n\pi z}{b} e^{i\beta x}, \tag{3.4}$$

$$E_z \propto A_{mn} \sin\frac{m\pi y}{a} \cos\frac{n\pi z}{b} e^{i\beta x}, \tag{3.5}$$

$$H_y \propto A_{mn} \sin\frac{m\pi y}{a} \cos\frac{n\pi z}{b} e^{i\beta x}, \tag{3.6}$$

$$H_z \propto A_{mn} \cos\frac{m\pi y}{a} \sin\frac{n\pi z}{b} e^{i\beta x}, \tag{3.7}$$

where A_{mn} is an arbitrary constant and β is the propagation constant whose value depends on a, b, m, and n. m and n are integers taking the values m = 0,1,2... and n = 0,1,2....

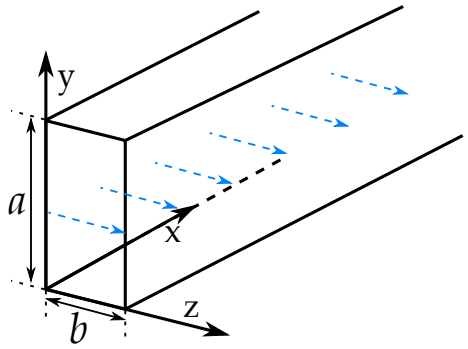

Figure 3.19: Geometry of a rectangular waveguide with the dimensions a and b, which are specified in table 3.1. In our measurements the microwave radiation (not shown) was propagating in the -x direction, anti-parallel to the UV laser (also not shown). The orientation of the E field is indicated by the blue dashed arrows.

There is no TE_{00} mode. For the TE_{10} mode ($m = 1$, $n = 0$) it can be seen from

equation 3.4 and 3.6 that $E_y = H_y = 0$. Additionally E_z in equation 3.5 reduces to,

$$E_z \propto A_{mn} \sin \frac{\pi y}{a} e^{i\beta x}, \tag{3.8}$$

indicating that the TE_{10} electric field is oriented in the z direction as shown by the dashed arrows in figure 3.19. The TE_{01} mode ($m = 0$, $n = 1$) has the electric field oriented in the y direction.

Each waveguide mode has a corresponding cutoff frequency (ν_c) below which propagation of that mode is not allowed. The cutoff frequency for each mode ν_c^{mn} is expressed as

$$\nu_c^{mn} = \frac{1}{2\sqrt{\mu\varepsilon}} \sqrt{\left(\frac{m}{a}\right)^2 + \left(\frac{n}{b}\right)^2}, \tag{3.9}$$

where $1/\sqrt{\mu\varepsilon} = c$ (speed of light). Taking the WR-112 guide (a = 28.5 mm and b = 12.6 mm) as an example the TE_{10} mode (m = 1, n = 0) has a cutoff frequency of ν_c = 5.26 GHz. The next order mode, TE_{01} mode, has a cutoff frequency of $\nu_c^{'}$ = 11.9 GHz. Therefore, only TE_{10} modes are allowed to propagate between $5.26 - 11.9$ GHz. As the TE_{10} mode has the lowest cutoff frequency, it is often called the dominant mode of a waveguide. The microwave frequencies used for our measurement of each transition were lower than $\nu_c^{'}$: therefore, only TE_{10} mode was present. TM_{00}, TM_{10}, and TM_{01} modes do not exist, and the lowest order TM_{11} modes cannot propagate as it has a cutoff frequency larger than the TE_{10} cutoff frequency, ν_c.

Three microwave guides were utilised in this work, one guide for each ν_J transition. Details of the microwave guides are listed in table 3.1. All three waveguides were designed and fabricated identically in-house, and differ only in their dimensions and range of frequency supported. The frequency column indicates the frequency range supported by each waveguide, and frequencies used in our measurements were within these ranges. The last column indicates the lowest order cutoff frequency (ν_c) and the next order cutoff frequency ($\nu_c^{'}$). Only TE_{10} modes can propagate between ν_c and $\nu_c^{'}$. The centre section of the front and back walls of

the waveguide were substituted with tungsten (W) mesh (95% transmission) to allow transmission of Ps atoms into and out of the guide as shown in figure 3.18. Microwave radiation, propagating in the -x direction, (antiparallel to the UV laser propagation as shown in figure 3.16) was coupled in through a high-frequency (45 GHz) feed through and an antenna as shown in figure 3.16(b) and 3.18.

Transition	Waveguide	Dimensions: $a \times b \times l$ (mm)	ν (GHz)	ν_c (ν_c') (GHz)
ν_0	WR-51	$12.95 \times 6.48 \times 160$	15 - 22	11.58 (23.14)
ν_1	WR-75	$19.05 \times 9.53 \times 160$	10 - 15	7.87 (15.74)
ν_2	WR-112	$28.50 \times 12.60 \times 160$	7 - 10	5.26 (11.9)

Table 3.1: Specification of the three waveguides used in the measurements. The dimensions of the waveguides are given in mm and the length, l for all waveguides was 160 mm. The last column indicates the lowest and next order cutoff frequency. Only TE_{10} modes are supported in the range between the cutoff frequencies.

For a constant power output from the microwave radiation generator (EXG X-Series N5173B, Keysight, California) the power measured had a variation as shown by the dashed line in figure 3.20. These variations are due to the frequency dependence of the cables and the feedthroughs. As these power variations can introduce systematic effects in our measurements, the output was adjusted to give a constant power level at the waveguide input, P_{Input}. Unless otherwise stated, our measurements of the ν_0, ν_1, and ν_2 transitions were taken with P_{Input} = 5, 4.3, and 6.5 mW respectively. The power transmitted into the waveguide, via a SubMiniature version A (SMA) antenna, was not measured directly, but was expected to be at least a factor of 2 lower than P_{Input}. Higher microwave powers can be used, but result in power broadening of the transition lineshapes.

The polarisation of the microwave radiation, determined by the physical structure of the waveguide, was parallel to the z axis, i.e., the orientation of the external magnetic field. As a result, only $2^3S_1 \rightarrow 2^3P_J$ transitions with $\Delta M_J = 0$ were expected to be driven as discussed earlier in section 2.2.3. Any microwave-radiation-induced transitions, as well as chamber-induced annihilations after leaving the guide, were monitored by four LYSO detectors (D1-4) surrounding the target

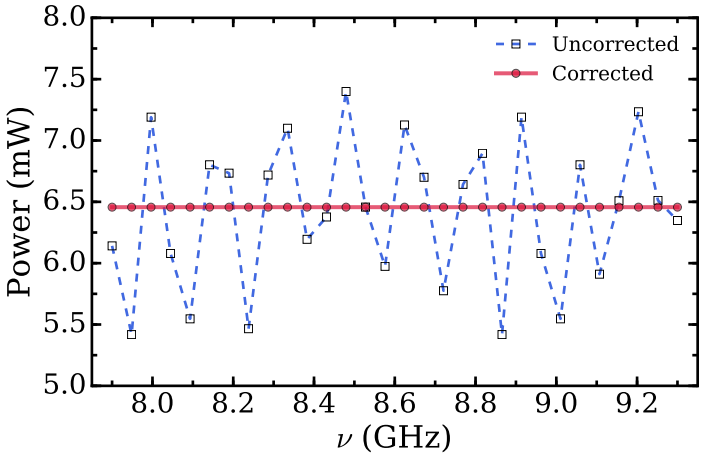

Figure 3.20: Example of obtaining a constant power input, P_{Input}, at the waveguide. The dashed line is the measured raw power for a fixed output from the generator, and the solid line indicates the corrected power after adjusting the power output from the generator.

chamber as shown in figure 3.16(c). The detectors recorded the time dependence of of the Ps annihilation radiation, and the microwave-radiation-induced transitions were quantified by the signal parameter S_γ as detailed in section 3.6.

3.8 2^3S_1 State Production

An essential prerequisite for the study of the $2^3S_1 \rightarrow 2^3P_J$ transition is an adequate population of atoms in the of 2^3S_1 states. The ground state (1^3S_1) to the 2^3S_1 state transition is formally electric dipole forbidden, but becomes single-photon allowed due to Stark mixing in an applied electric field [11] and was the method chosen for this work. Other approaches have involved Doppler-free two-photon excitation of the $1^3S_1 \rightarrow 2^3S_1$ transition [54], single-photon $1^3S \rightarrow 3^3P$ transition followed by radiative decay to the 2^3S_1 [59], as well as production via collisions of positrons on solid targets [48, 120] have been previously studied. These techniques were not considered in our measurements as the implementation was not possible at the time, or efficiencies were too low.

The $1^3S_1 \rightarrow 2^3S_1$ excitation with a single 243 nm photon, which is not allowed due to electric dipole selection rules ($\Delta S = 0$, $\Delta l = \pm 1$, and $\Delta J = 0, \pm 1$ ($0 \nleftrightarrow 0$)),

can be accomplished if done in a region of electric field, $F_{ex.}$ [11]. The electric field causes Stark mixing of the $n = 2$ sub-states and turning the field off after excitation allows pure 2^3S_1 atoms to be generated. The electric field, $F_{ex.}$, in the excitation region was generated by the potential bias applied to the target electrode and the ground plane of the microwave guide mesh. The potential bias applied to the target for all our measurements was -3.5 kV, and the waveguide mesh was located 6 mm away from the target electrode. This meant that the initial electric field strength in the excitation region was 5.8 kV/cm.

The Stark perturbed states in the $n = 2$ level was shown earlier in figure 2.1. For zero electric field strength the $n = 2$ states are pure and have either $l = 0$ or $l = 1$. For non-zero electric field Stark mixing occurs coupling the triplet S ($l = 0$) and P ($l = 1$) states as discussed earlier in section 2.2.1. This results in the creation of Stark mixed $n = 2$ state, denoted as $2^3S_1'$, which possesses both 2S and 2P character. The mixing of the states is dependent on the strength of the electric field as shown in figure 3.21(a).

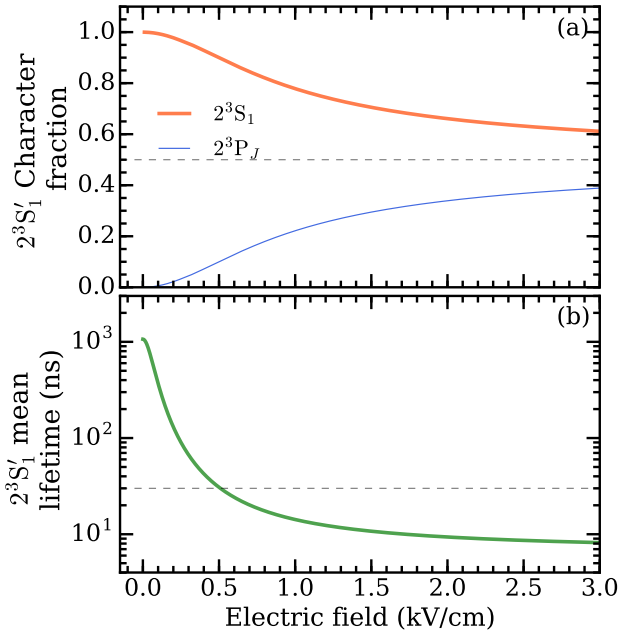

Figure 3.21: Calculated pure 2^3S_1 and 2^3P_J character possessed by the $2^3S_1'$ state (a) and the lifetime of the $2^3S_1'$ state (b) as a function of electric field. The horizontal line in (a) at 0.5 represents equal 2S and 2P character regime. The horizontal line in (b) represents the HV switch off time (30 ns). From [11]

The $l = 1$ (2P) character of the mixed state permits the single photon excitation from the 1^3S_1 ground state to the $2^3S_1^{'}$ state, while the $l = 0$ (2S) character prolongs the mixed state lifetime from 3.19 ns to $\approx$ 8 ns. Immediately after excitation, the potential bias on the target (therefore, the electric field also) was turned off promptly with a fast high-voltage (HV) switch [GHTS 60 (90-10% $\approx$ 30 ns), Behlke] to allow the mixed state to evolve into pure 2^3S_1 state adiabatically. Here, some $2^3S_1^{'}$ states gradually acquired 100% 2^3S_1 character fraction as shown in figure 3.21(a). At the same time the lifetime increased from $\approx$ 8 ns to 1.1 μs as shown in figure 3.21(b). Since the field switching rate was comparable to the $2^3S_1^{'}$ decay rate, extraction of pure 2^3S_1 atoms was possible.

The delay of the trigger pulse sent to the HV switch was scanned across to find the optimal 2^3S_1 state generation. The production of 2^3S_1 state atoms, analysed through the SSPALS method, was indicated by a spectra that looked similar to Rydberg production. The transition to the 2^3S_1 state was quantified with the parameter S_γ and S_γ is expected to be negative as discussed earlier in section 3.6.2. Figure 3.22(a) shows S_γ as a function of switch trigger time. As expected, S_γ has a negative value and different magnitude for the switching time range. The trigger time with the largest negative S_γ was identified as the optimal switch time, and all the trigger times, shown in figure 3.22(a), are relative to the optimal time.

Figure 3.22(b) shows the SSPALS background subtracted spectra for three switch trigger times, including the optimal delay. It can also be seen that spectra for non-optimal switch times have a smaller annihilation peak and lower S_γ compared to the optimal trigger time. This is because for earlier switch times (i.e., $\Delta T_{\text{Switch}} < 0$) the target electrode was turned off too early. This meant that the positrons were not implanted as deeply: therefore, the positronium emitted had higher energy, and less efficient temporal overlap with the excitation laser. For late switching times (i.e., $\Delta T_{\text{Switch}} > 0$) $2^3S_1^{'}$ states were still generated, but as the field was not turned off promptly, the evolution into pure 2^3S_1 states was less efficient.

The sequence of events, from positron implantation to HV switching, are

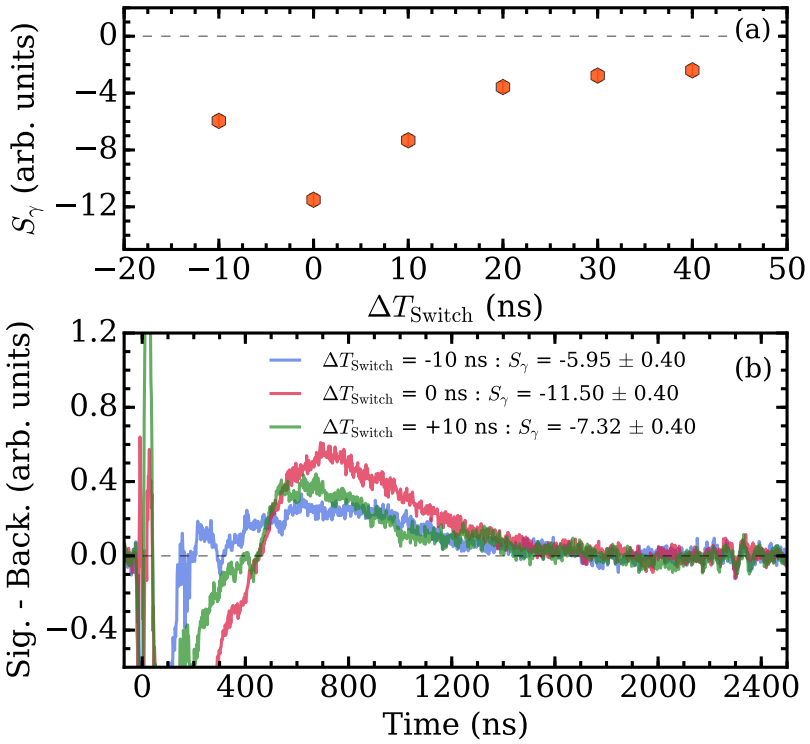

Figure 3.22: (a) S_γ from the 2^3S_1 production as a function of the switch trigger time. (b) Background subtracted SSPALS spectra for different switch delays. The trigger times in (a) have been plotted relative to the optimal switch time. This data was taken by one of the four detectors placed around the target chamber.

shown in figure 3.23. A plastic scintillator was used to measure the relative timing between the positron implantation and laser pulse. A fast silicon photodiode and HV probe were then used to record the relative timing between the laser pulse and HV switching. As discussed in section 3.5 the relative timing between the positron and laser pulses was fixed to ensure optimal excitation efficiency.

The plastic scintillator PMT has a delay due to the transit time of the electron pulse in the photo-multiplier tube. This delay did not lead to significant broadening: therefore, the positron and laser pulses were distinguishable. From the scintillator we were able to determine the delay between the positron and laser pulses. The Si photodiode, however, is faster and therefore, was used to measure the true arrival time of the laser pulse. The scintillator laser pulse (taken without the positron signal) and the photodiode laser pulse were then matched to shift the positron arrival pulse to the true arrival time (t = 0 ns) as shown in figure 3.23.

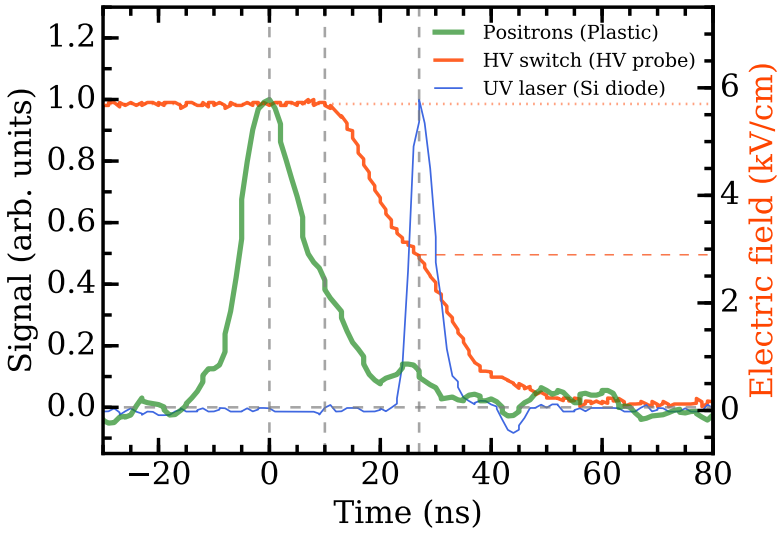

Figure 3.23: Relative time delay between the positron implantation, laser excitation, and the field switch off. The positron pulse arrival is detected by a plastic detector, which also detects the laser pulse (not shown) via a small pinhole. A fast Si photodiode also detects the same laser pulse, and was used to shift the positron peak to the true arrival time (set to $t = 0$). The HV switch output was measured by a fast HV probe. The 3.5 kV potential bias of the target electrode was switched off $\approx$ 10 ns after positron implantation as it resulted in optimal 2^3S_1 state production.

In figure 3.23 it can be seen that the target electrode was actually switched off after positron implantation, but before optical excitation. This allowed deeper positron implantation (hence, slower Ps atoms), while ensuring optimal 2^3S_1 state production. As a result the electric field during optical excitation was $F_{ex.} \approx 3$ kV/cm.

The transition of ground state atoms to the 2^3S_1 state was analysed with SSPALS method. Figure 3.24(a) shows an example of a lifetime spectra, taken with a LYSO detector, with the UV laser on (solid) and off (dashed) resonance. The transition is indicated by excess annihilation signal late times in the 'laser on' spectra and can be more clearly seen in the background subtracted spectra in figure 3.24(b). This spectra ('Sig. - Back.') represents the production and subsequent detection of the 2^3S_1 atoms via the process: $1^3S_1 \rightarrow 2^3S_1' \rightarrow 2^3S_1 \rightarrow 3\gamma$. The background subtracted spectra shows the time profile of the 2^3S_1 annihilation events relative to the ground state atoms. As the metastable state has longer annihilation

lifetime than the 1^3S_1 state, the curve exhibits a peak at late times. In the case where the electric field was not switched off after laser excitation (i.e., $F = F_{ex.}$), the Stark mixed $2^3S_1'$ states did not evolve into pure 2^3S_1 state: therefore, no excess annihilation signal was observed.

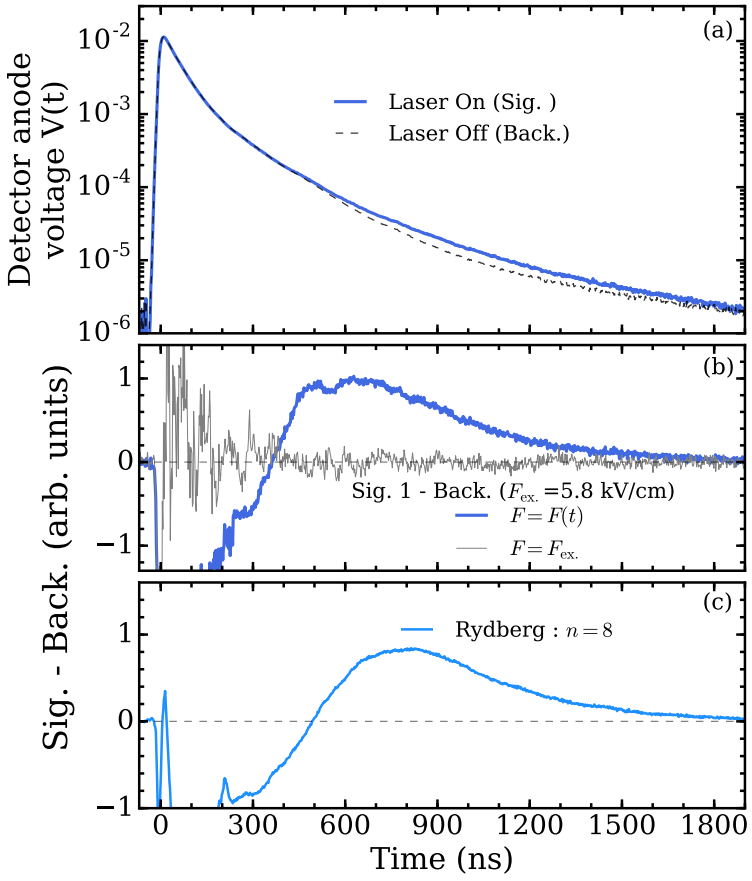

Figure 3.24: (a) Example lifetime spectra measured with and without the UV laser tuned to resonance. (b) 2^3S_1 production (Sig. - Back.) background subtracted spectra for two cases: with and without $F_{ex.}$ switched off after laser excitation. (c) Background subtracted spectra showing excitation to the $n = 8$ Rydberg state. This example data was recorded by one of the four LYSO detectors.

The background subtracted lifetime spectra for excitation to the $n = 8$ Rydberg state is shown in figure 3.24(c), where an IR laser was utilised to facilitate the transition. Ps in $n = 8$ Rydberg states have negligible annihilation rates compared to $n = 2$ level, and have radiative lifetime of ≈ 1 μs (similar to the metastable state lifetime). As a result the observed SSPALS signals for 2^3S_1 and Rydberg states are similar.

3.9 $2^3S_1 \rightarrow 2^3P_J$ Detection

Shortly after excitation the 2^3S_1 atoms entered microwave guide where transition to the 2^3P_J levels were driven. To probe the $2^3S_1 \rightarrow 2^3P_J$ ($J = 0,1,2$) transitions three rectangular waveguides were utilised in this work, the specifications for which are summarised in table 3.1. To drive the $2^3S_1 \rightarrow 2^3P_J$ ($J = 0,1,2$) (henceforth, labelled ν_0, ν_1, and ν_2 respectively) the frequency of the microwave radiation was tuned to the corresponding resonance values as stated in table 1.2.

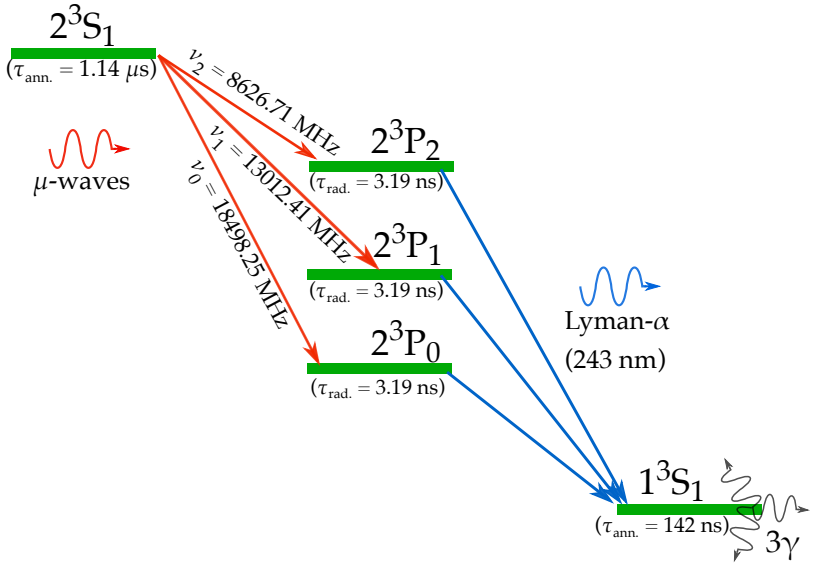

Figure 3.25: Schematic of the $2^3S_1 \rightarrow 2^3P_J \rightarrow 1^3S_1 \rightarrow 3\gamma$ process via which the microwave induced transitions were observed. The radiation induced signal S_γ was quantified by monitoring the annihilation γ-rays. The procedure for populating the 2^3S_1 states was discussed in section 3.8.

Once driven to the 2^3P_J state the Ps atoms radiatively decay to the 1^3S_1 state with a mean radiative lifetime of 3.19 ns, emitting a 243 nm Lyman-α photon in the process. In the previous experiment [85] the Lyman-α photons were detected to observe the fine structure transitions. In our measurements, however, the annihilation photons from the ground state atoms were detected to quantify any radiation induced signal S_γ. This microwave-radiation-induced quenching process can be expressed as $2^3S_1 \rightarrow 2^3P_J \rightarrow 1^3S_1 \rightarrow 3\gamma$, and is illustrated in figure 3.25. To quantify the microwave-induced signal, S_γ, a background spectrum was necessary and was

defined to be the microwave off-resonance signal (i.e., the 2^3S_1 production spectrum).

The mean annihilation lifetime of the 1^3S_1 atoms is 142 ns and these annihilation events occur at earlier times relative to the 2^3S_1 state annihilation lifetime (1.1 μs). The signal for 2^3S_1 production is indicated by the blue spectra in figure 3.26(b), and is similar to the signal already shown in figure 3.24(c). The transition to 1^3S_1, after the microwave induced transition, is indicated by the orange spectra in figure 3.26(b), where the annihilation peak shifts to earlier times. This is a direct representation of the transfer of some atoms in the 2^3S_1 state to the shorter-lived 1^3S_1 state.

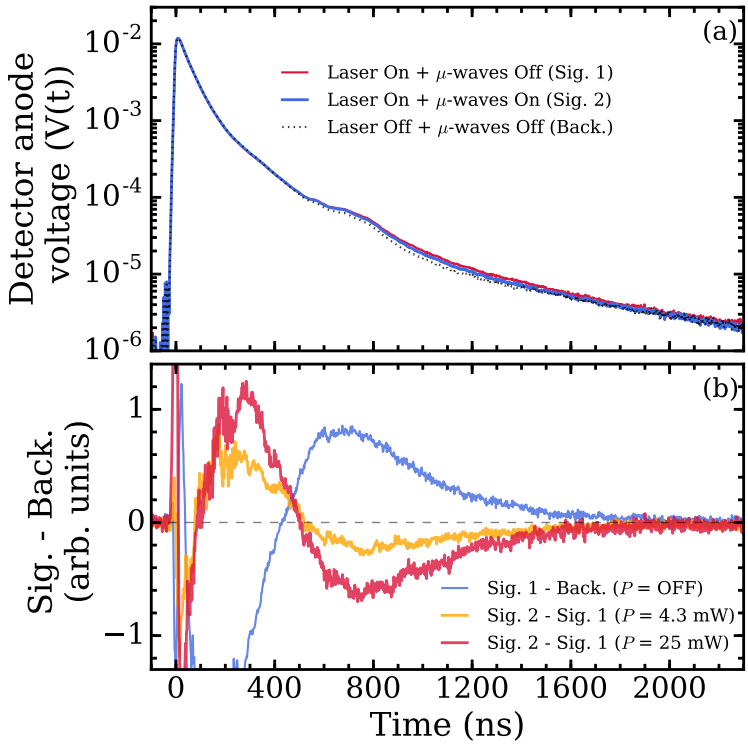

Figure 3.26: (a) Lifetime spectra for UV laser tuned to 1^3S_1-2^3P_J resonance and μ-waves radiation off (Sig. 1), 1^3S_1-2^3P_J resonance and μ-waves radiation on (Sig. 2), and both UV and μ-wave radiation off resonance (Back.). (b) Background subtracted spectra showing the 2^3S_1 spectra (Sig. 1 - Back.), and the μ-wave signal (Sig.2 - Sig. 1) for two different powers.

The similarity between the longer-lived 2^3S_1 and $n = 8$ Rydberg signal was highlighted in figure 3.24. On the other hand, the microwave quenching signal is

similar to photoionisation, as both processes happen on an early timescale. Therefore, some similarity can be seen between the orange spectra in figure 3.26(b) and the photoionisation signal in figure 3.13(b). The microwave quenching peak is, however, broader than the photoionisation peak as the Ps distribution had spread out by the time the 2^3S_1 atoms were quenched in the waveguide. Photoionisation happened immediately after emission from the SiO_2 target and therefore, resulted in a narrower peak. The value of microwave radiation induced transition signal, S_γ, is also positive, similar to the photoionisation process.

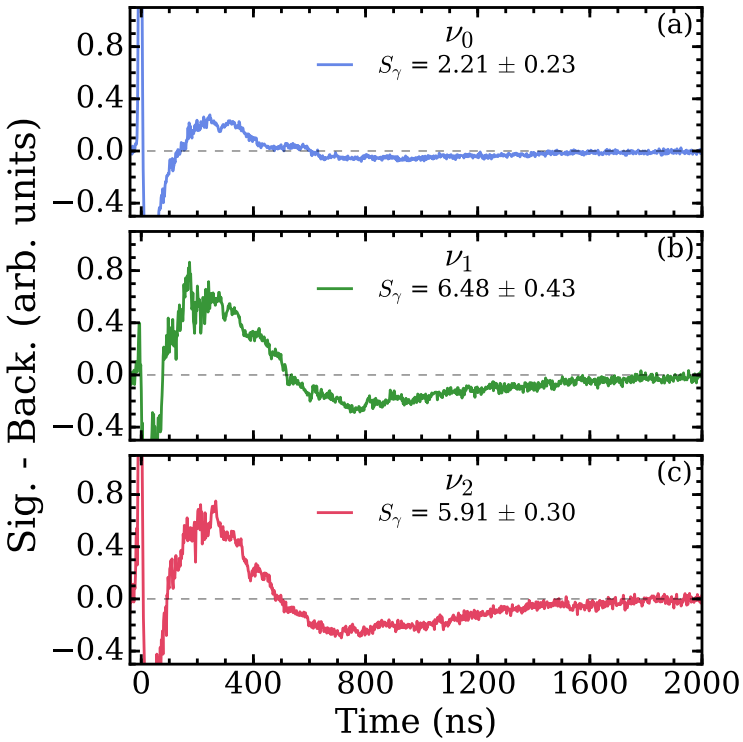

Figure 3.27: The microwave radiation induced quenching peak for the ν_0, ν_1, and ν_2 transitions. The microwave radiation power for all three measurements was set at 8 mW. The ν_0 transition only had one allowed pathway and therefore, had smaller S_γ than the signal for ν_1 and ν_2 transitions which had 2 and 3 pathways respectively.

When higher power ($\approx$ 25 mW) of microwave radiation was used the quenching peak was larger as shown by the red spectra in figure 3.26(b). Our measurements, however, were conducted at lower power ($\approx$ 5 mW) to avoid power broadening as mentioned earlier in section 3.7. This meant that the $2^3S_1 \rightarrow 2^3P_J$ transition

was not saturated and not all of the 2^3S_1 atoms were excited. Furthermore, as the lifetime of Ps in its ground state is 142 ns, some 1^3S_1 atoms were expected to exit the microwave guide before annihilation as shown in figure 3.16(b).

The microwave radiation induced quenching peaks for each transition are shown in figure 3.27. This example data was taken with microwave radiation power of $\approx$ 5 mW. All three transitions have similar quenching process ($2^3S_1 \rightarrow 2^3P_J \rightarrow 1^3S_1 \rightarrow 3\gamma$) and resulted in positive S_γ. The ν_0 signal, however, had a weaker quenching peak compared to ν_1 and ν_2. As explained earlier in section 2.2.3 this was because the ν_0 transition had only one allowed $\Delta M_J = 0$ pathway to the 2^3P_0 state as shown in figure 3.28. The ν_1 and ν_2 had 2 and 3 individual transitions respectively, and therefore, generated greater S_γ than the ν_0 transition.

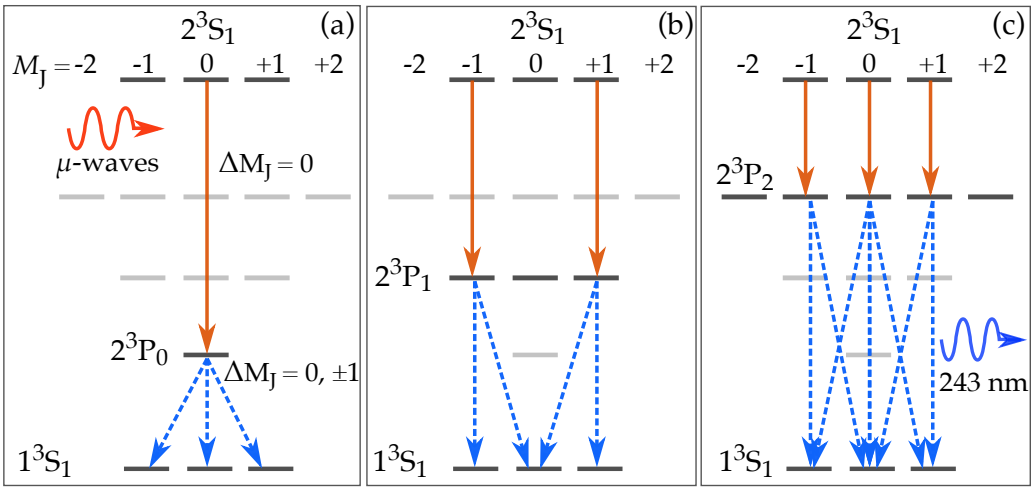

Figure 3.28: The allowed $2^3S_1 \rightarrow 2^3P_J$ transitions with $\Delta M_J = 0$: ν_0 (a), ν_1 (b), and ν_2 (c). The 2^3P_0 state only has $M_J = 0$ substate, so only one $\Delta M_J = 0$ transition occurs in the ν_0 transition. The $2^3P_J \rightarrow 1^3S_1$ radiative transitions, indicated by the dashed lines, occurs via $\Delta M_J = 0$ and $\Delta M_J = \pm 1$. The 1^3S_1 state atoms annihilate into 3 gamma-ray photons after a mean annihilation lifetime of 142 ns.

Chapter 4

Microwave Spectroscopy of $n = 2$ Fine Structure Intervals

4.1 The $2^3S_1 \rightarrow 2^3P_J$ Transitions

Lineshapes for the $\nu_J = 2^3S_1 \rightarrow 2^3P_J$ ($J = 0, 1, 2$) transitions (figure 3.25) were generated by measuring S_γ as a function of the microwave frequency ν. The values of S_γ were quantified by defining a measurement with the microwave radiation at ν = 1 GHz and P_{Input} = 0 mW (i.e., microwaves OFF) to be the background signal. This microwave radiation induced signal, S_γ, is represented by the spectra in figure 3.27.

Example lineshapes for the ν_0, ν_1, and ν_2 transitions are presented in figure 4.1(a), (b), and (c) respectively, with a Lorentzian function fitted to each lineshape. Each lineshape, consisting of 24 data points, needed $\approx$ 20 hours of acquisition time. The three waveguides employed to probe each transition are summarised in table 3.1. The mean radiative lifetime of the 2^3P_J states is $\tau_{\text{rad.}}$ = 3.19 ns: therefore, the natural linewidth of the $2^3S_1 \rightarrow 2^3P_J$ transition in the absence of broadening effects is $\Gamma_0 = 1/2\pi\tau_{\text{rad.}} \approx 50$ MHz.

A Lorentzian lineshape can be written as

$$L(\nu) = \frac{2A/\pi\Gamma_m}{1 + 4(\nu - \nu_R)^2/\Gamma_m^2}, \tag{4.1}$$

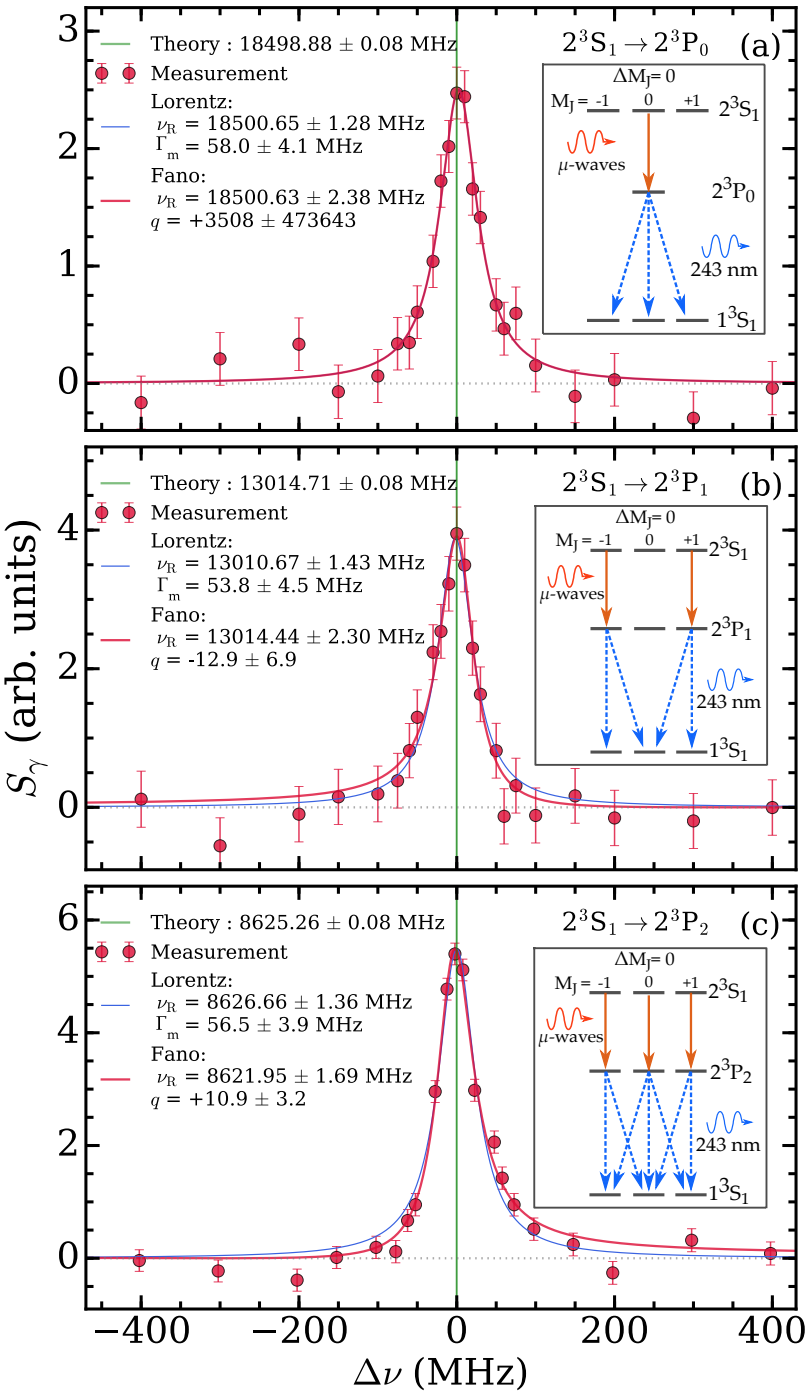

Figure 4.1: An example lineshape of ν_0 (a), ν_1 (b), and ν_2 (c) transitions as a function of the microwave frequency. Both Lorentzian and Fano function fits were applied to all measurements and the resonance frequencies from both fits are stated along with the linewidth and Fano asymmetry parameter (see equation 4.2). The green vertical lines indicates the theoretical transition frequencies at B = 30 G. The insets show the allowed $\Delta M_J = 0$ transition (solid arrows) to the 2^3P_J states, followed by $\Delta M_J = 0, \pm 1$ radiative decay (dashed lines) to the ground state. The data were measured in an axial magnetic field of ≈ 30 G, and recorded by detector D4.

where A is an arbitrary constant, Γ_m is the measured linewidth (FWHM), and ν_R is the resonance frequency. Fitting the lineshapes with the Lorentzian function in equation 4.1 yields a line width of $\approx$ 60 MHz for all three transitions and ν_R values of 18500.65 $\pm$ 1.28, 13010.67 $\pm$ 1.43, and 8626.66 $\pm$ 1.36 MHz for the ν_0, ν_1, and ν_2 transitions respectively. The linewidth is slightly wider than 50 MHz and a notable feature in figure 4.1 is the asymmetry in the ν_1 and ν_2 lineshapes. The lineshapes shown in figure 4.1(a) (b), and (c) were taken with P_{Input} = 5, 4.3, and 6.5 mW respectively.

The spectral lineshape width is affected by various effects such as atomic motion (Doppler broadening), interaction time with radiation field (transit time broadening), and intensity of the radiation (power broadening). If the microwave radiation intensity is sufficiently large, the stimulated emission rate increases and the subsequent saturation of the population density in the excited state occurs. Saturation occurs when the populations of atoms in the initial and excited state are equal. The saturation of excited state population causes additional line broadening called power broadening. A power broadened lineshape has a width that scales as $\Gamma = \Gamma_0(1 + P/P_{\text{sat}})^{1/2}$, where P_{sat} is the saturation power of the transition [93].

To verify that the microwave powers used were not in the saturation regime the microwave radiation induced signal, S_γ, was measured for various powers, P_{Input}, as shown in figure 4.2(a). As the microwave generator had a limited power output an amplifier was used for the measurements with $P_{\text{Input}} > 8$ mW. When higher powers were used the signal observed was also higher and appears to have saturated around 20-25 mW. Lineshapes of the ν_1 transition were also measured at various powers and the linewidths extracted from Lorentzian fits to these lineshapes measured for different powers are plotted in figure 4.2(b). As the microwave power was increased the linewidths also increased from $\approx$ 60 MHz to $\approx$ 90 MHz. Assuming P_{Input} = 25 mW to the saturation intensity, the 90 MHz linewidth is consistent with the expected broad linewidth due to power broadening. For $P_{\text{Input}} < 8$ mW the linewidths do not appear to get narrower indicating another source which broadens the lineshape from

50 MHz to 60 MHz. In order to avoid power broadening, all measurements were taken at $P_{\text{Input}} \approx 5$ mW unless otherwise stated.

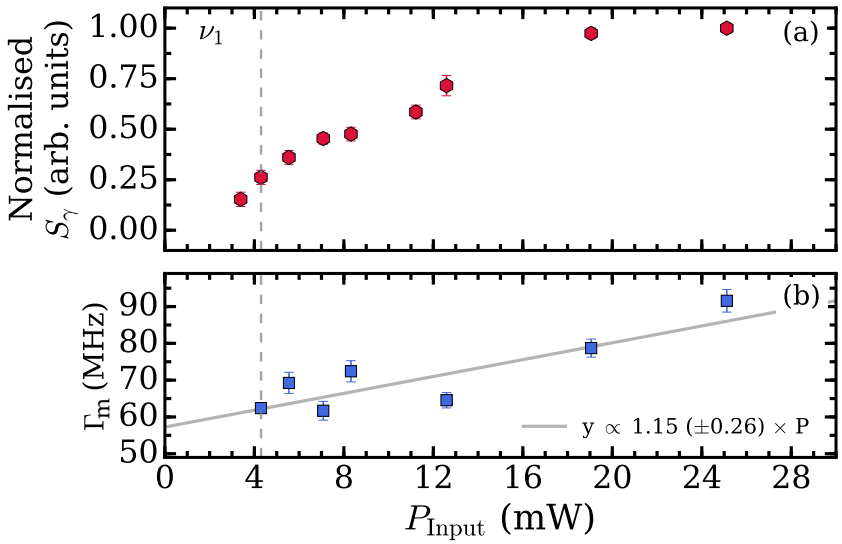

Figure 4.2: (a) The microwave induced transition signal, S_γ, measured at resonance for different microwave powers. (b) FWHM obtained from Lorentz function fits to lineshapes measured at different powers. These measurements were taken for the ν_1 transition (ν = 13012 MHz) at a magnetic field of 82 G. For $P_{\text{Input}} >$ 8 mW, an amplifier was used to obtain more power. The vertical dashed line indicates the power (4.3 mW) at which the ν_1 measurement was taken.

Ps atoms with speed of $\approx 9 \times 10^4$ m/s have a total flight time of 70 - 140 ns across the three waveguides (table 3.1). The microwave field strength at the waveguide boundaries is zero by definition, and as a result the effective flight time through the waveguide during excitation is shorter. The transit time broadening contribution was expected to be ≈15-10 MHz for ν_0-ν_2 transitions and is the source of the ≈ 10 MHz broadening of the lineshapes.

The ν_1 and ν_2 lineshapes in figure 4.1(b) and (c) have a slight asymmetry, while the ν_0 lineshape does not appear asymmetric. When distortions in the lineshapes are present [121] a Lorentz profile is not sufficient as the transition frequency may no longer be described by the centre of the line. To consider such asymmetry, the lineshapes were also fitted with the well-known Fano function [122, 123]. The Fano profile was first introduced in the context of photoionisation cross-sections, to describe the effect of interference between a discrete resonant transition and a

continuous non-resonant background, but have been widely applied to other phenomena [94, 124]. The Fano profile can be expressed as

$$F(\nu) = A\left[\frac{(q+\varepsilon)^2}{(1+q^2)(1+\varepsilon^2)}\right], \tag{4.2}$$

where A is an arbitrary constant, q is the asymmetry parameter. The reduced energy ε is a dimensionless quantity given by

$$\varepsilon = \frac{\nu - \nu_R}{\gamma/2}, \tag{4.3}$$

where ν_R is the Fano resonance frequency, and γ is the Lorentzian FWHM. The definition of equation 4.2 means that for large q values (i.e., $q \rightarrow \infty$) the function will approach a symmetric Lorentzian (equation 4.1). For $q = 0$ the Fano function will result in a symmetric dip, sometimes called an anti-resonance. For small and finite q the Fano profile is asymmetric as shown by the examples in figure 4.3.

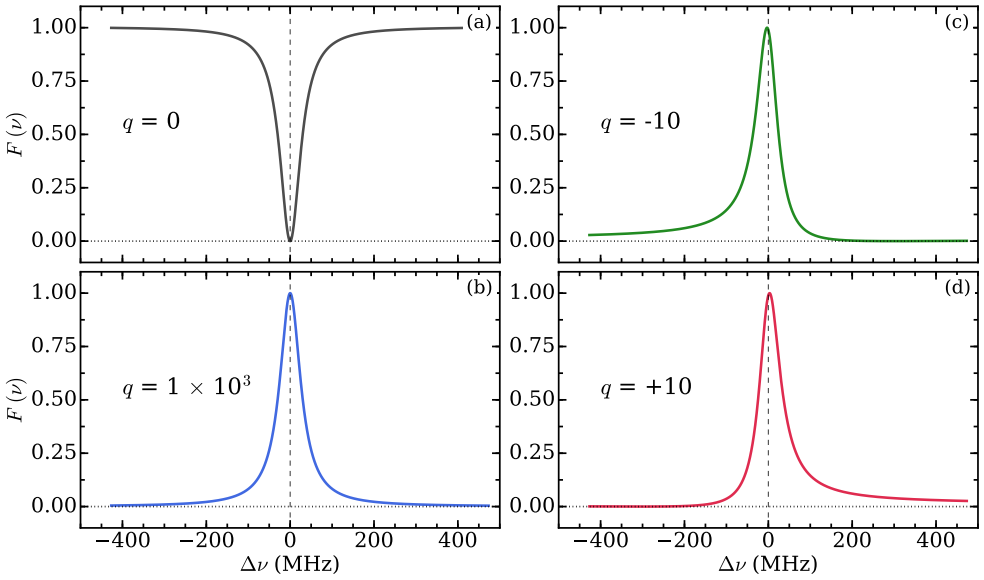

Figure 4.3: Examples of Fano profiles, with $\gamma = 50$ MHz, for different asymmetry parameters as indicated in the figures. For $q < 0$ ($q > 0$), the lineshape is skewed towards lower (higher) frequencies.

The Fano profile is only used to quantify the asymmetry, or lack thereof, in the lineshapes. The Fano ν_R may not describe the true resonance frequency of the

transition, which would require a complete lineshape model that takes into account the mechanism(s) causing the asymmetry. The Fano ν_R does not coincide with the peak of the Fano profile when asymmetry is present and the frequency at the peak of the profile may be extracted by taking the derivative of the profile. It may be the case that when the perturbations are small and the linewidth is relatively large, the frequency at the peak may be closer to the true resonance frequency than ν_R.

The results of Fano profile fits to the measured lineshapes, with the γ and q as free fit parameters, are also shown in figure 4.1. For the ν_1 transition, the lineshape is skewed towards lower frequencies resulting in $q \approx$ -13. In contrast, the lineshape for the ν_2 transition is skewed towards higher frequencies with $q \approx +10$. A rise in one of the slopes of the ν_1 and ν_2 lineshapes can be clearly seen in figure 4.1.

Whatever the source of the asymmetry in the ν_1 and ν_2 transition lineshapes, it appears to be absent in the ν_0 transition as the asymmetry parameter is over 3000 as shown in figure 4.1. Fano function fits to the data presented in figure 4.1 yield ν_R values of 18500.63 $\pm$ 2.38, 13014.44 $\pm$ 2.30, and 8621.95 $\pm$ 1.69 MHz for the ν_0, ν_1, and ν_2 transitions respectively. The ν_0 line shape is not asymmetric and therefore, both Lorentz and Fano profile fits yield similar ν_R values, which coincide with the centre of the lineshape. In the ν_1 and ν_2 lineshapes it can be seen that while the perturbation to the lineshape may be small, the extracted ν_R values from the Lorentz and Fano fits are significantly different. The lineshapes in figure 4.3 indicate that for $q \approx \pm 10$ the difference in the Lorentz and Fano ν_R values is ≈ 5 MHz, while for $q = \pm 100$ the difference is reduced to ≈ 0.6 MHz.

The lineshapes measured at various powers, to investigate power broadening (figure 4.2), were also fitted with the Fano profile to extract the asymmetry, q. The result of these fits are shown in figure 4.4. It can be seen that the asymmetry does not disappear for low powers and is not significantly different at high powers. Nevertheless, our measurements were taken at $P_{\text{Input}} \approx 5$ mW. Due to the presence of the asymmetry in the ν_1 and ν_2 lineshapes, the resonance frequency cannot be extracted reliably using the Lorentzian function.

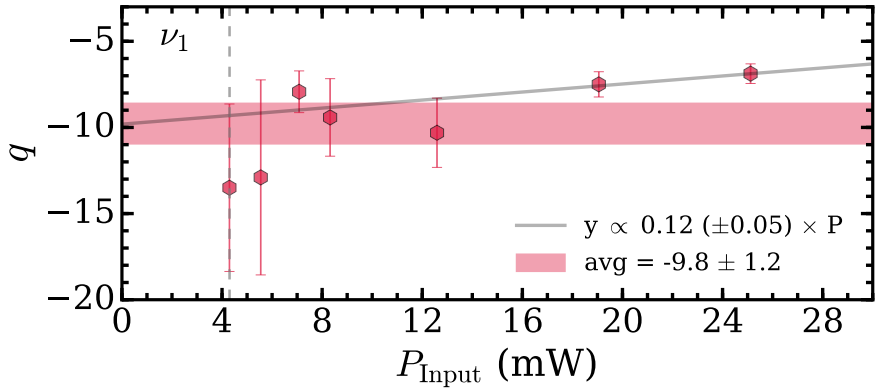

Figure 4.4: Fano asymmetry value, q, extracted from Fano function fits to lineshapes measured at various microwave radiation powers, P_{Input}. These measurements were taken for the ν_1 transition at a magnetic field of 82 G. For $P_{\text{Input}} > 8$ mW, an amplifier was used to obtain more power. The vertical dashed line indicates the power (4.3 mW) at which the ν_1 measurement was taken.

As stated earlier in section 3.7 the target chamber was surrounded by four LYSO detectors, each recording the annihilation time dependence independently. An example of the comparison of data collected by the detectors is shown in figure 4.5. The ν_R, Γ_m, and q values were consistent across the four detectors used in the experiment. Therefore, all fit results from the detectors were averaged. The ν_R values from Lorentz and Fano profiles were calculated for comparison. As the Lorentz linewidth (Γ_m) and Fano linewidth (γ) are similar, all linewidths quoted henceforth are Γ_0.

The relationship between the electric field strength E and the power P in the waveguide is different to that of free space [85]. Therefore, the measured lineshapes required a correction. This correction takes the form: $E^2 \sim P[1-\nu_c^2/\nu^2]^{-1/2}$, where ν_c = 11.58, 7.87, and 5.26 GHz are the lowest order cutoff frequencies for the waveguides used in the ν_0, ν_1, and ν_2 measurements. An example of the corrected data is represented by the solid markers in figure 4.5 while the uncorrected data are indicated by the empty markers. This procedure amounted to a correction of +0.017 MHz to the ν_R values while the Γ_m and q values were unaffected, and is similar for other transitions and applied magnetic field.. This power correction was found to be small as the waveguides used in our measurements was optimised for the frequen-

cies needed. In contrast, the WR-90 waveguide used in the Mainz experiment [85] operates in the frequency range 8.2-12.4 GHz and the power correction magnitude was +0.30 MHz.

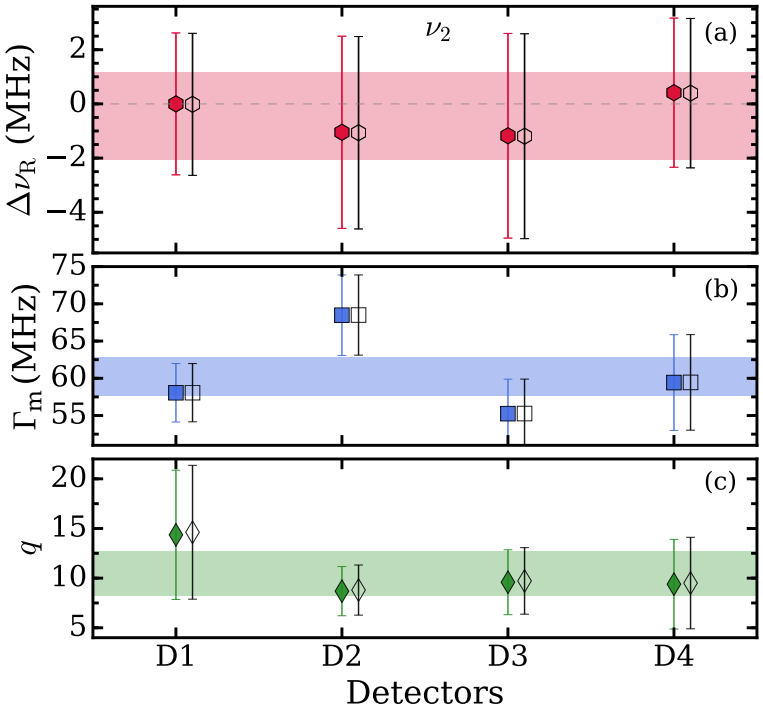

Figure 4.5: The ν_R (a), Γ_m (b), and q (c) values measured by all four detectors. The values in (a) are shown relative to the D1 measurement. The shaded bars indicate the averaged values. The filled and empty markers represent the data with and without the power correction method mentioned in [85], with the latter case shifted horizontally for clarity. Power corrections added +0.017 MHz shift to the ν_R, while the linewidth and asymmetry remained unchanged. The data presented is for Fano profile fits to ν_2 transition measured at B = 55 G.

4.2 Zeeman Measurements

Unlike the previous experiment conducted in Mainz [85] where the positron beam was extracted from the magnetic field, the measurements reported here were performed in an axial magnetic field. Therefore, the Zeeman shifts of the $n = 2$ energy levels had to be considered. The shift of the $n = 2$ energy levels due to the magnetic field were shown previously in figure 2.3, where the vertical arrows indicate the allowed $\Delta M_J = 0$ transitions. The calculated transition frequency as a function of

the magnetic field were also shown previously in figure 2.4. To account for these Zeeman shifts several measurements were taken for a range of magnetic fields for all three transitions.

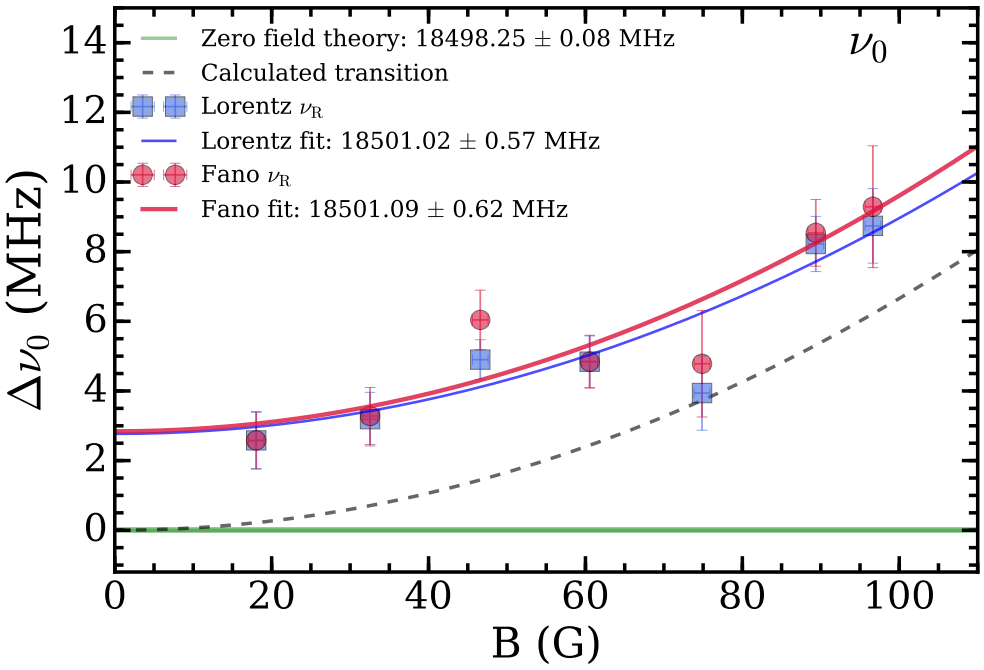

Figure 4.6: Measured ν_0 transition frequencies, relative to the theoretical resonance indicated by the horizontal green line, for a range of applied magnetic fields. The data points are from Lorentz fits (square) and Fano fits (circle) to the lineshapes. Quadratic fits were applied to all individual sets separately to extract the zero field resonance frequency as indicated. The uncertainty in the extrapolated values are statistical. The dashed line represents the calculated transition frequency as a function of B field.

Figure 4.6 shows the measured ν_0 resonance frequencies, relative to the theoretical zero field resonance, for magnetic fields ranging from $\approx$ 20-100 G. Measurements at fields lower than 20 G were not taken due to difficulty in positron beam transport. The data points shown are from Lorentz (square) and Fano profile (circle) fits to the lineshapes. Each data point (y variable) and the associated errorbar in figure 4.6 are the averaged value from all four detectors used. The uncertainty in the B field strengths (x variable) was set to be $\pm$1 G.

Measuring the transition at several magnetic fields allowed the resonance frequency at zero magnetic field to be extrapolated. A quadratic function of the form:

$aB^2 + c$ (where a is the quadratic coefficient, and c is the intercept at $B = 0$ G, i.e., the field free resonance value) was applied to the data in figure 4.6. This procedure yielded field free ν_0 resonance frequencies of 18501.02 ± 0.57 and 18501.09 ± 0.62 MHz for the Lorentz and Fano fitting routines respectively. The uncertainties from the extrapolations are statistical and due to the errors in the individual data points, and the ± 1 G variation in the magnetic field were considered in the quadratic fit. As explained earlier in section 4.1 the ν_0 lineshapes were not asymmetric and thus, similar ν_R values were obtained from both Lorentz and Fano function fits to the lineshape. By extension, the zero field extrapolated frequencies for both methods are also similar.

The calculated transition frequency, indicated by the dashed line in figure 4.6, has the quadratic coefficient of $a = 6.7\times10^{-4}$ MHz/G^2. The quadratic coefficients from fits to the Lorentz and Fano results were found to be $a = (6.2 \pm 1.2)\times10^{-4}$ and $a = (6.8 \pm 1.5)\times10^{-4}$ MHz/G^2 respectively. While the calculation and measurements have the similar field dependence, all the extrapolated values are shifted from the calculation by $\approx$ +2.8 MHz.

Figures 4.7 and 4.8 show the measured ν_1 and ν_2 resonance frequencies for magnetic fields ranging from $\approx$ 20-100 G. Similar to the ν_0 Zeeman measurement, the data points were the averaged value from the four detectors used. The observed resonance frequency for the ν_1 and ν_2 transitions have a positive and negative Zeeman shifts respectively as expected (see figure 2.4).

The extrapolated zero B field resonance frequencies for the ν_1 transition are 13008.41 ± 0.52 and 13014.13 ± 0.58 MHz for the Lorentz and Fano fitting routines respectively. Similarly, for ν_2 we obtained zero field transition frequency of 8628.28 ± 0.35 and 8624.67 ± 0.35 MHz for the two lineshape fitting routines. Unlike the ν_0 transition, the Lorentz and Fano fit results are not in agreement and have a separation of $\approx$ 5 MHz for both ν_1 and ν_2 measurements. This is because of the asymmetric nature of the lineshapes as shown earlier in figure 4.1.

For the ν_2 interval two $\Delta M_J = 0$ transitions were permitted as shown by the

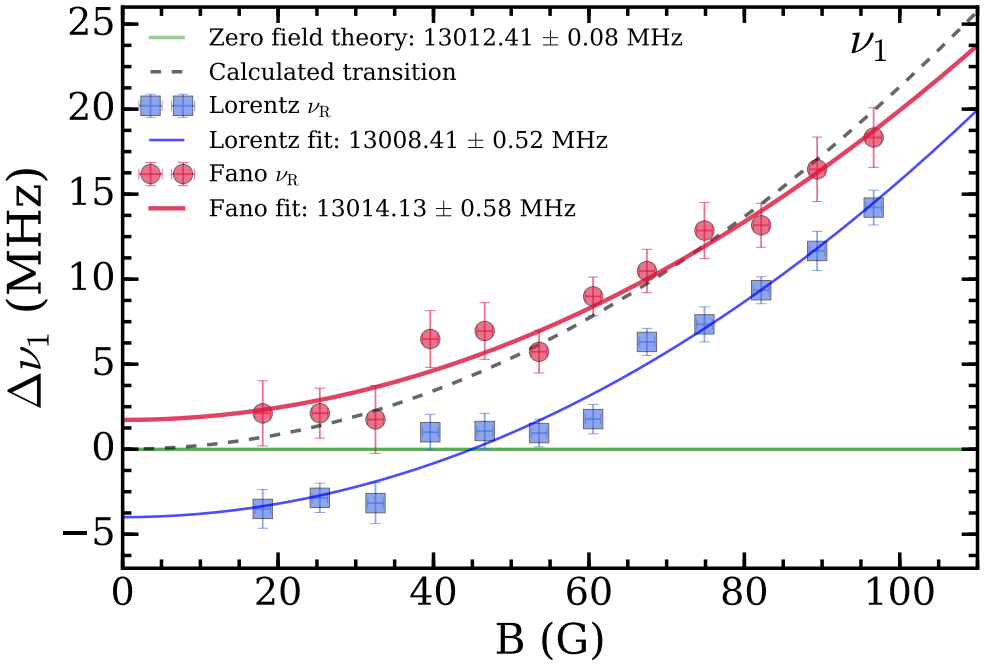

Figure 4.7: Measured ν_1 transition frequencies, relative to the theoretical resonance indicated by the horizontal green line, for a range of applied magnetic fields. The data points are from Lorentz (square) and Fano fits (circle) to the lineshapes. Quadratic fits were applied to individual data sets separately to extract the field free resonance frequency as indicated. The uncertainty in the extrapolated values are statistical. The dashed line represents the calculated transition frequency as a function of B field.

vertical arrows in figure 2.3. If these individual transitions were resolvable widening of the lineshape at higher magnetic fields would be expected. The measured linewidths, however, did not exhibit any significant field dependence as indicated by the linear fit shown in figure 4.9. Therefore, the measured linewidths are essentially independent of the magnetic field. The ν_0 data in figure 4.9(a) exhibits a positive trend but only one transition (i.e., M_J=0→0) was possible for this case. It is possible that this is due to the large errors in the data points. The ν_1 interval also has only one allowed $\Delta M_J = 0$ transition (i.e., $M_J = \pm 1 \rightarrow \pm 1$) and the linewidth was found to be independent of the magnetic field as shown in figure 4.9(b). The field averaged linewidths for the ν_0, ν_1, and ν_2 transition were 66.2 ± 1.0, 62.4 ± 0.9, and 61.8 ± 0.7 MHz respectively.

For this reason the weighted average of the two individual $\Delta M_J = 0$ allowed

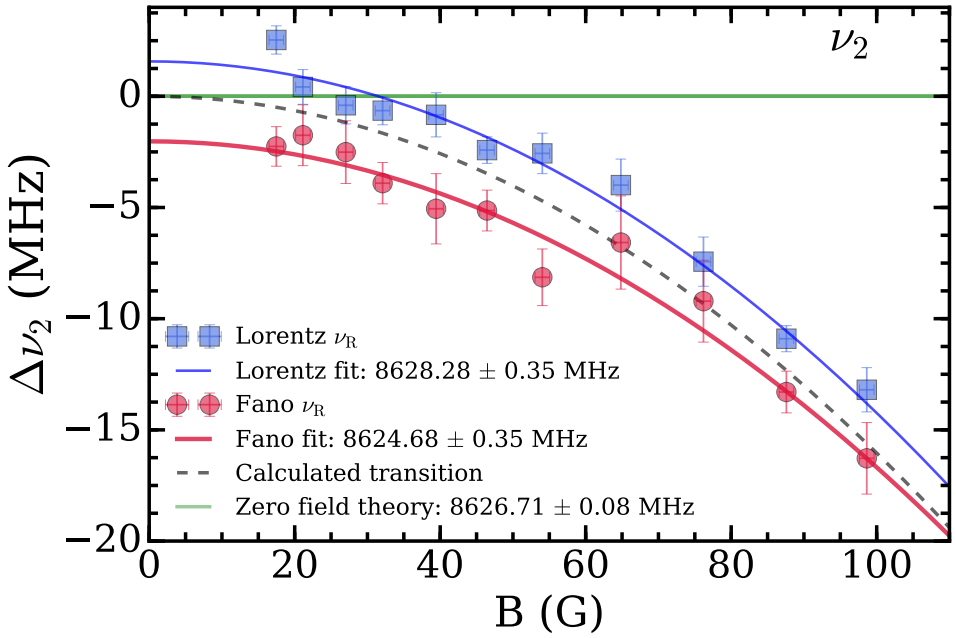

Figure 4.8: Measured ν_2 transition frequencies, relative to the theoretical resonance indicated by the horizontal green line, for a range of applied magnetic fields. The data points are from Lorentz fits (square) and Fano fits (circle) to the lineshapes. Quadratic fits were applied to individual data sets separately to extract the field free resonance frequency as indicated. The uncertainty in the extrapolated values are statistical. The dashed line represents the calculated transition frequency as a function of B field.

transitions in the ν_2 interval was taken. The calculated transition frequency as a function of the magnetic field is indicated by the grey dashed lines in figure 4.7 and 4.8. The calculated ν_1 transition frequency has a quadratic coefficient of $a = 2.1\times10^{-3}$ MHz/G^2. The quadratic coefficients from fits to the Lorentz and Fano data in figure 4.7 were found to be $a = (2.0 \pm 0.1)\times10^{-3}$ and $a = (1.8 \pm 0.1)\times10^{-3}$ MHz/G^2 respectively.

For the ν_2 measurement shown in figure 4.8, the quadratic coefficients from the calculation, fit to Lorentz, and Fano data points were found to be $a = -1.6\times10^{-3}$, $a = (-1.6\pm0.1)\times10^{-3}$, and $a = (-1.5\pm0.1)\times10^{-3}$ MHz/G^2 respectively. The zero field frequencies of the ν_1 and ν_2 transitions, for both Lorentz and Fano fit cases, are shifted by $|\Delta\nu|$ = 2-4 MHz from the calculation as shown in figures 4.7 and 4.8.

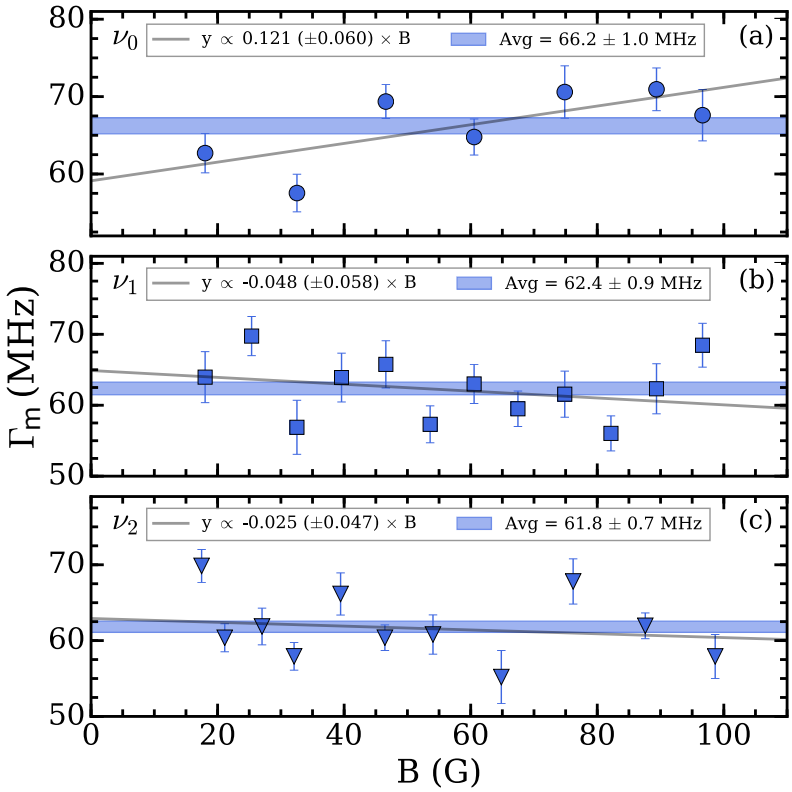

Figure 4.9: The measured Lorentz linewidths for the ν_0 (a), ν_1 (b), and ν_2 (c) transitions as a function of the magnetic field B. The horizontal shaded bars represent the average value of Γ_m and the solid lines represent a linear fit to the data.

4.3 Interference Effects

The measured Fano asymmetry parameters, q, for a range of magnetic fields are shown in figure 4.10. The parameter q is defined such that values close to zero indicate an asymmetric lineshape, whereas large values of q indicate a symmetric lineshape. The slope of the linear fit to the ν_0 data in figure 4.10(a) (denoted by y) is zero within the errors and the asymmetry is found to be essentially independent of the magnetic field. The smallest value of q in ν_0 data is on the order of 10^5, and both Lorentz and Fano fits to the ν_0 lineshapes yielded similar ν_R values even at high B fields as shown in figure 4.6. The large values of q justify the use of the Lorentz profile to describe the resonance frequency of the ν_0 interval.

The linear fits to the ν_1 and ν_2 Fano q values are shown in figures 4.10(b) and (c) respectively. Similar to the linear fit in figure 4.10(a), the asymmetry in the ν_1

and ν_2 lineshape is observed to be independent of the magnetic field. Therefore, the asymmetry is not likely to be due to the presence of an axial magnetic field in the excitation region.

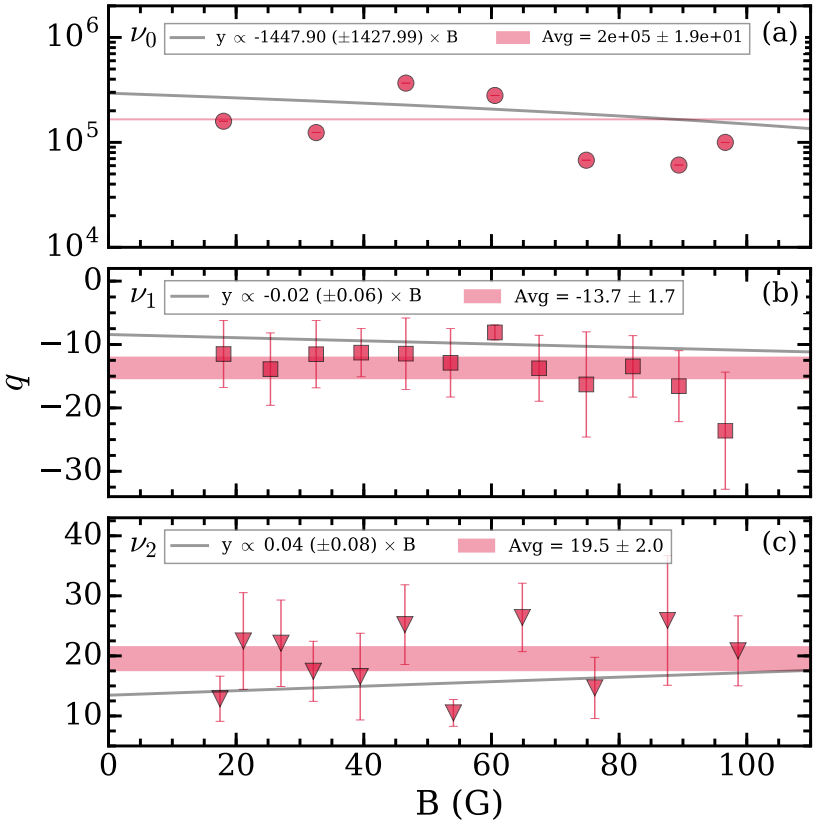

Figure 4.10: The measured Fano asymmetry parameter, q, for the ν_0 (a), ν_1 (b), and ν_2 (c) transitions as a function of the magnetic field B. The horizontal shaded bars represents the average value of q and the line represent a linear fit to the data.

The experiment performed in Brandeis [83] was done in a 50 G field region and the measured lineshapes do not appear asymmetric. The experiments in Michigan [84] and Mainz [85] were performed in a magnetic field free region and the lineshapes also do not appear asymmetric. All three measurements, however, had broader lineshapes ($\approx$ 85-100 MHz) and lower statistics. Aside from the presence of the magnetic field in the excitation region another difference between our measurement and the previous experiment [85] is the detection scheme. Previously, the Lyman-α photons, emitted after the transition to the 2^3P_J states, were detected, whereas we detected the 1^3S_1 annihilation gamma-rays to observe the microwave

transition.

It is known that in experimental schemes where fluorescence radiation is detected to observe a transition to the excited state, the coupling between the incident photon ν_L (driving the transition to the excited state) and the emitted photon ν_S (due to the radiative decay of the excited state) can lead to significant quantum interference (QI) effects and line centre shifts [94]. A simplified schematic of a fluorescence detection scheme is shown in figure 4.11. In the work by Beyer and co-workers involving 2S-4P transition in hydrogen, the fluorescence radiation (Lyman-γ) from the 4P-1S radiative decay was detected to quantify the 2S-4P transition [94]. Geometric dependence of the interference effects, due to the radiation coupling, was reported and a Fano-Voigt lineshape model was used to account for these effects. Instead of detecting ν_S, depletion in the initial state can also be monitored to quantify the transition to the excited state. Interference effects are expected to be absent for this method.

In the Ps fine structure measurements, microwave radiation (ν_L) drives the stimulated emission to the 2^3P_J state and a 243 nm Lyman-α photon (ν_S) is emitted during the radiative decay to the ground state. The Lyman-α radiation can be detected to observe the fine structure transition and was the method employed in the previous experiments [83–85]. Interference effects due to ν_L and ν_S coupling may have been present in those experiments but line distortions were not reported, possibly due to the statistics of the measurements. Instead of the fluorescence 243 nm photon, we detected the gamma-ray photons from the ground state annihilation to observe the microwave transition. As the gamma-ray photons are decoupled from the incident microwave radiation, we are not sensitive to this type of quantum interference effect.

Quantum interference effects from neighbouring off-resonance states have also been found to shift line centres and Hessels and co-workers have studied this type of interference extensively [121, 125, 126]. The presence of a nearby state provides an off-resonant transition pathway that can interfere with a resonant transition. The

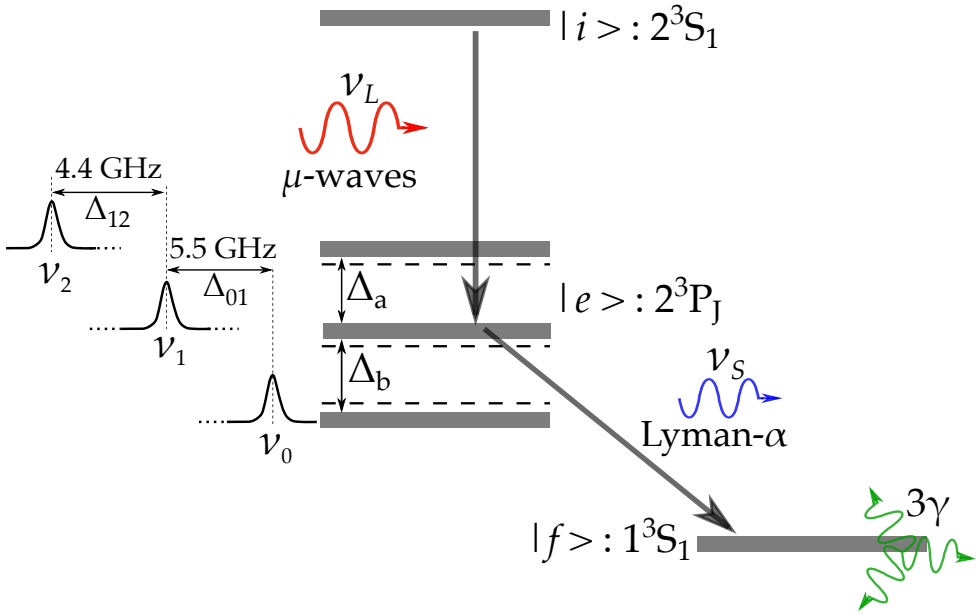

Figure 4.11: Schematic of the transition where the incident radiation ν_L takes the initial state $|i\rangle$ to the excited state $|e\rangle$. A photon ν_S is emitted when the excited state radiatively decays to the final state $|f\rangle$. The transition lineshapes and the separation of the line centers are illustrated beside the excited state levels. The Ps ground state annihilates into three gamma-ray photons. The presence of the neighboring 2^3P_J states (separated by Δ_{01} or Δ_{12}) can lead to interference and shift in the resonant frequency. The shift of the resonance due to nearby states are indicated by the dashed lines.

amplitude of the transition to the off-resonant state may be small, but can have a significant affect on the resonant transition. The main resonance is pulled away from its line centre because it sits on the tail of the perturbing off-resonant state. This process may not necessarily result in an asymmetric lineshape, but shifts in line centre can still occur [127]. A "rule of thumb" gives an estimate for the error obtained when fitting a Lorentzian to a lineshape affected by QI effects. For a resonant transition to a particular state, with another electric-dipole-allowed transition to a second state separated by Δ as shown in figure 4.11, the expected shift ($\Delta\nu$) in the main transition due to QI may be approximated by $\Delta\nu \approx \Gamma_0^2/2\Delta$, assuming both transitions have the same linewidth Γ_0 [121].

The $2^3S_1(0) \rightarrow 2^3P_0(0)$ and $2^3S_1(0) \rightarrow 2^3P_2(0)$ transitions both have natural linewidths of 50 MHz and are separated by $\Delta_{01} + \Delta_{12} \approx 10$ GHz as shown in figure 4.11. The shift in the ν_0 resonance frequency due to the interference from the ν_2

off-resonant pathway is then expected to be $\approx$ 130 kHz. This is more than an order of magnitude smaller than the $\approx$ 2.8 MHz shift seen in the ν_0 resonance frequency (figure 4.6). The $2^3S_1(0)\rightarrow 2^3P_1(0)$ is forbidden and therefore, not expected to shift the ν_0 line centre. Similarly, the $2^3S_1(\pm 1)\rightarrow 2^3P_1(\pm 1)$ and $2^3S_1(\pm 1)\rightarrow 2^3P_2(\pm 1)$ transitions are separated by 4.4 GHz. Then, the expected shift in the ν_1 resonance due to the off-resonant ν_2 pathway will be $\approx$ 300 kHz, which is also too small to account for the 2-4 MHz shift, for both Lorentz and Fano cases, as seen in figure 4.7. The ν_2 resonance is expected to be similarly shifted by $\approx$ 300 kHz due to the nearby 2^3P_0 and 2^3P_1 states. Similarly, the symmetric ν_0 lineshape is consistent with the fact that the corresponding ν_1 transition (i.e., $M_J = 0 \rightarrow M_J = 0$) is suppressed

Figure 4.12 shows the result of calculations performed to verify the estimates made by the "rule of thumb". The calculation is based on the open-source Quantum Toolbox in Python (QuTiP) software [128].

Since only the transitions satisfying $\Delta M_J = 0$ were expected due to the linear polarisation of the microwave radiation field, spectral lineshape for each of the $2^3S_1 \rightarrow 2^3P_2$ transition was calculated with a set of four basis states. The four basis states were (1) the initial 2^3S_1 state, (2) the excited 2^3P_J state to which the transition was driven, (3) the perturbing off-resonant $2^3P_{J'}$ state, and (4) the final 1^3S_1 state. An atom is prepared in an initial state and a diagonal matrix (H_0) describes the energy four basis states. The interaction of the atom with the microwave field is described by another matrix, $H(t)$, and the off-diagonal elements of $H(t)$ represent the Rabi frequency (Ω_{Rabi}) of the transition to the excited state. The loss from the excited state is facilitated through radiative decays ($\tau_{\text{rad.}}$) to the final state. The evolution of the system interacting with the microwave field is then evaluated by the time-dependent Schrodinger equation and the expectation values of each state is calculated by a Lindblad master equation solver [129]. By taking the final expectation value of loss from the initial state at the end of the interaction period, a lineshape as a function of the microwave frequency can be generated.

Both Lorentz and Fano functions are fitted to the generated lineshapes shown

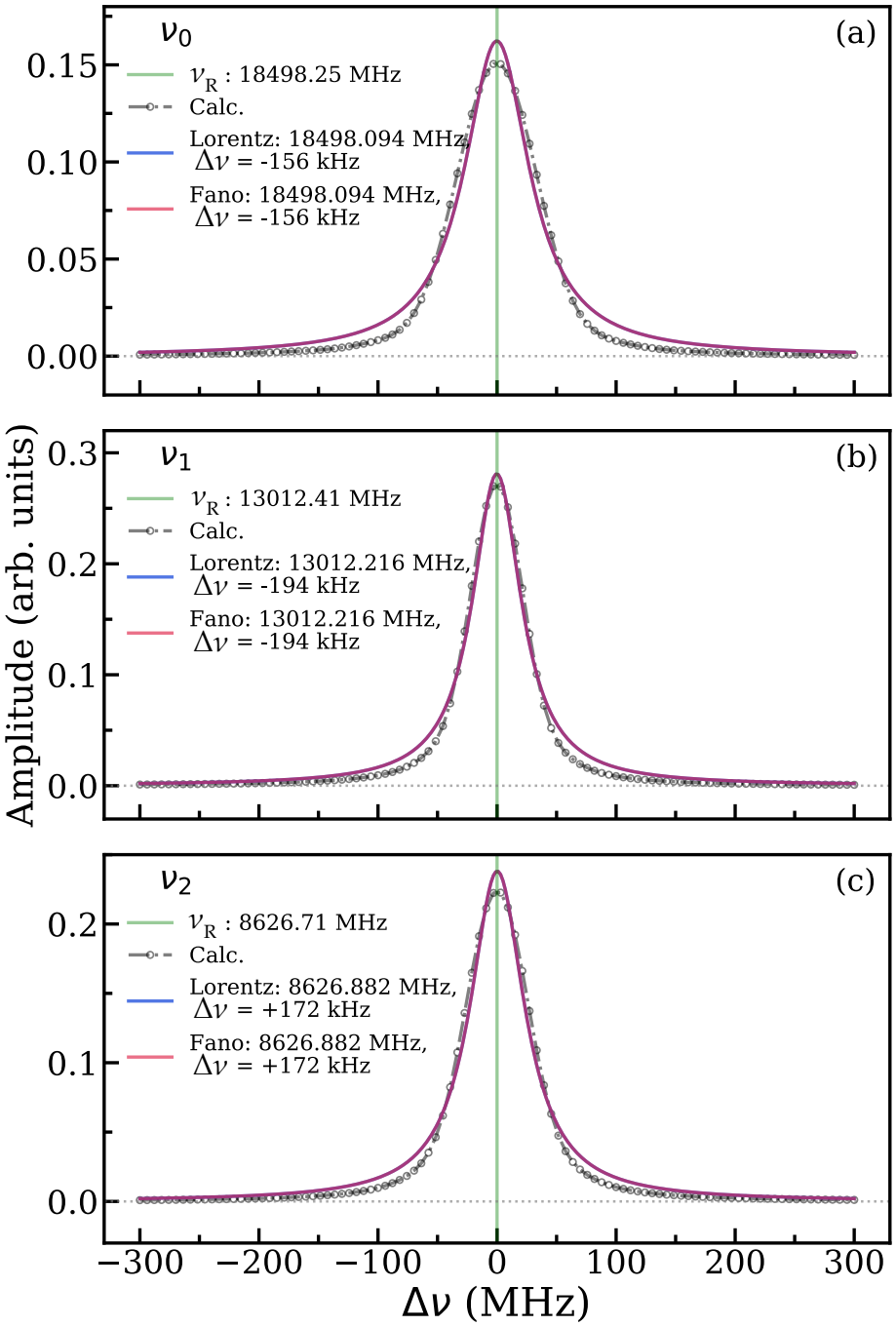

Figure 4.12: Calculated lineshapes showing the shift in the resonance frequency due to far-detuned off-resonance states. The lineshapes are fitted with Lorentz and Fano functions, and both functions yield identical results due to the lack of asymmetry. The ν_0 and ν_1 resonance are pulled by the ν_2 resonance and results in a negative shift as shown in (a) and (b). The ν_2 resonance (c) is shifted positively. The width of the lineshapes are $\approx$ 60 MHz. The green vertical lines represent the theoretical resonance frequency (ν_R) of each transition.

in figure 4.12 to calculate the shift ($\Delta\nu$) of the line centre from the theoretical resonances, ν_R (Table. 2.1). The lineshapes are not asymmetric ($q > 10^6$) and thus, both functions yield the same centroids. The shift in the ν_0 resonance (figure 4.12(a)) due to the perturbing 2^3P_2 state is $\approx$ -160 kHz, which is similar to the"rule of thumb" expected shift. The shift is negative as ν_0 resonance is being pulled towards a lower frequency off-resonance state. The shift in the ν_1 resonance, shown in figure 4.12(b), due to the perturbing 2^3P_2 state is $\approx$ -200 kHz, and is the negative direction similar to the ν_0 shift. The shift of the ν_2 line centre due to the 2^3P_0 and 2^3P_1 states is shown in figure 4.12(c). The individual shifts due to the two perturbing off-resonant transitions are weight averaged according to their transition strengths and the total shift amounts to $\approx$ +170 kHz. Because the ν_2 resonance is being pulled towards higher frequency states, the shift is positive.

All these shifts in ν_J transitions are similar to the estimate made by the rule of thumb, and are too small to explain the $\approx$ 2-4 MHz shifts observed. As the states are separated by $\Delta > 80\Gamma_0$ (Γ_0 = natural linewidth = 50 MHz), calculated lineshapes are not asymmetric. Decreasing the separation of states can generate asymmetric lines as the individual Lorentzians begin to overlap with each other. These results suggest that the frequency shifts and asymmetry observed in the measured lineshapes are not caused by the quantum interference effects between the resonant and nearby off-resonant transitions.

4.4 Evaluation of Systematic Effects

4.4.1 Doppler Shifts

Due to the low mass of Ps, even atoms with energies of order 50 meV have large speeds which result in significant Doppler broadening of the 1S-2P lineshapes. To measure this Doppler spread (i.e., the velocity spread) of the Ps atoms emitted from the silica target, the $1^3S_1 \rightarrow 2^3P_J$ transition lineshape was measured as a function of the UV laser wavelength. As the laser was propagating in the x direction, only

the x velocity distribution was measured. The distribution in the y direction of the ground state atoms will be identical to the x distribution. The 100 GHz bandwidth of the UV laser covered all the 2^3P_J states during the excitation. The mean radiative lifetime of the 2^3P_J states ($\tau_{rad.}$ = 3.19 ns) means that the natural linewidth of this transition is also 50 MHz.

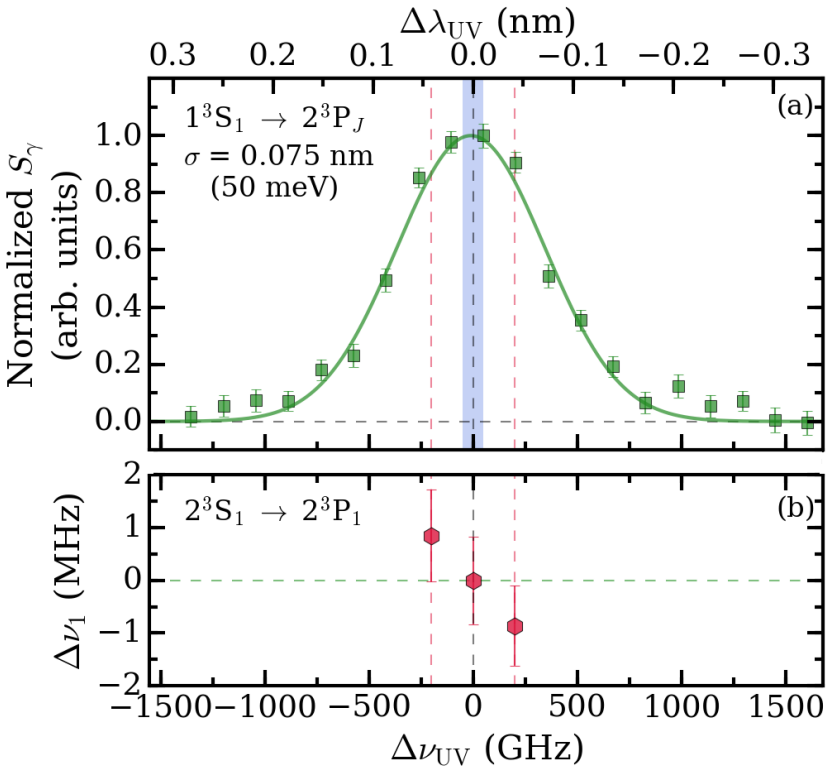

Figure 4.13: (a) An example of a Doppler broadened lineshape of the $1^3S_1 \rightarrow 2^3P_J$ transition centred around 243 nm. (b) Relative shift in the $2^3S_1 \rightarrow 2^3P_1$ transition as a function of UV detuning. The dashed vertical line in (a) indicates the resonance wavelength (243.01 nm) and the shaded bar indicates the 100 GHz bandwidth of the UV laser.

An example of a Doppler profile scan is shown in figure 4.13(a). It can be seen that, due to the large speeds of the Ps atoms, the transition linewidth is much wider than the 50 MHz natural width. The example $1^3S_1 \rightarrow 2^3P_J$ lineshape was fitted with a Gaussian function, which yielded a Doppler width of $\approx$ 500 GHz. This Doppler profile is the full velocity distribution (v_x) of the ground state atoms in the direction of the laser and the v_y distribution will be similar. The rms transverse speed, v_x^{rms}, of the Ps atoms is calculated from the width (σ) of the Doppler profile and the centre

wavelength (λ_0) as $v_x^{rms} = \sigma c/\lambda_0 \approx 9.3\times10^4$ m/s.

The velocity distribution of the Ps atoms after laser excitation (with UV wavelength tuned to resonance) is shown in figure 4.14. The full 500 GHz v_x distribution was filtered to $\approx$ 100 GHz by the bandwidth of the UV laser, which was propagating in the x direction. The v_y distribution was unaffected by laser selection and therefore, is equivalent to the Doppler profile shown in figure 4.13(a). The v_z distribution has been measured previously via time-of-flight (TOF) spectroscopy of Rydberg atoms with similar speeds from the same silica target guided in a multi-ring electrostatic guide [6]. Since the UV laser dominated the distribution of excited state atoms, 2^3S_1 and Rydberg atoms are expected to have identical distributions. In addition, the transverse and longitudinal speeds were found to be comparable [6, 16].

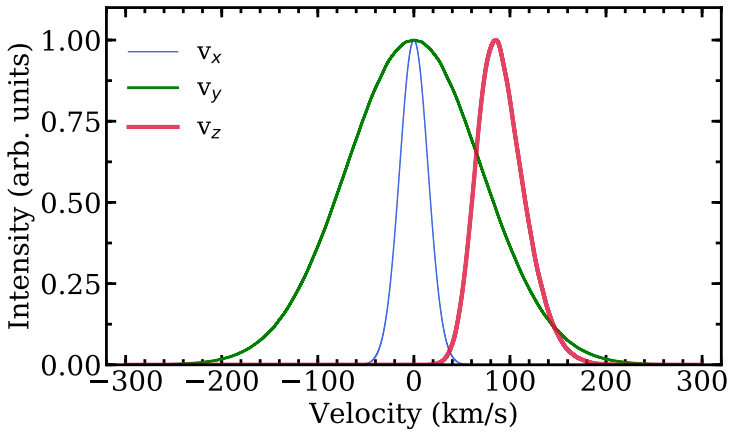

Figure 4.14: Velocity distribution of Ps atoms after laser excitation. Since the ground state v_x and v_y are similar, the excited state v_y distribution is a representation of the Doppler distribution, and the v_x distribution was dictated by the 100 GHz laser bandwidth. The v_z distribution was obtained from the TOF measurement of Rydberg atoms with similar v_y distribution as explained in the text.

When the UV laser was tuned to the resonance wavelength (λ_{UV} = 243.01 nm) to drive the $1^3S_1 \rightarrow 2^3S_1$ transition, the 100 GHz bandwidth of the laser only selected atoms with speeds of 10^6 cm/s in the direction of the laser. The resulting Doppler broadening of the ν_J transitions was expected to be less than 2 MHz. The transverse angular distribution after the laser selection is symmetric: therefore, the

laser bandwidth only results in Doppler broadening.

While the use of slow atoms eliminated most of the systematic effects that were present in the previous experiments, the possible misalignment of the laser relative to the waveguide axis could have resulted in Doppler shifts. Figure 4.15 shows an example illustration of the possible UV laser and waveguide misalignment. The UV laser position was measured at the entry and exit viewports (VP1 and VP2), 510 mm apart, of the target chamber. The misalignment, in either $\pm z$ direction, was estimated to be no more than the width of the laser beam (≈ 3 mm). This gave a maximum laser misalignment angle, $\theta_{\mathrm{UV}} \approx \pm 0.3°$.

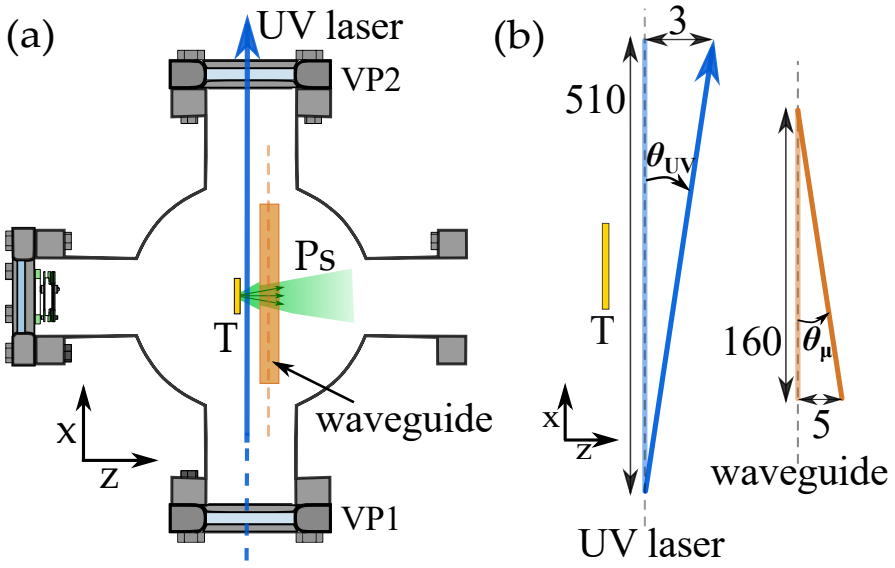

Figure 4.15: (a) Top view of the target chamber, showing the laser viewports (VP1 and VP2) which were used to align the UV laser to the SiO_2 target (T). (b) An enlarged representation of possible laser and waveguide misalignment relative to their axis (dashed line). The laser misalignment was expected to be less than $\theta_{\mathrm{UV}} \approx 0.3°$, and the waveguide misalignment was expected to be less than $\theta_\mu \approx 1.8°$. The total possible misalignment was therefore, estimated to be less than $\pm 2.0°$. The schematic in both (a) and (b) are not drawn to scale.

It was also possible for the waveguide to be slightly off axis. During the waveguide installation, the position of the guide was inspected from above as illustrated in figure 4.15(a). A misalignment of ≈ 5 mm would have been noticeable during the installation: therefore, we estimate the possible misalignment of the waveguide to be less than $\theta_\mu \approx \pm 1.8°$. The compounded possible misalignment between the

laser and the waveguide was then expected to be no more than $\pm 2°$.

Such misalignment can lead to excitation of ground state atoms either going towards or away, on average, from the microwave antenna. The resulting Doppler shift ($\nu_J \times v_z \sin(\theta)/c$) from $\pm 2°$ misalignment was then calculated to be no larger than 215, 150, and 100 kHz for the ν_0, ν_1, and ν_2 transitions respectively.

Figure 4.13(b) shows the ν_1 transition frequencies measured when the UV laser was detuned away from the λ_{UV} = 243.01 nm resonance wavelength by $\pm$ 200 GHz. This had a similar effect as that of laser-waveguide misalignment, i.e., generating 2^3S_1 atoms that were, on average, travelling either towards or away from the microwave antenna. Because the UV laser and microwave radiation were travelling in opposite directions as shown in figure 3.16, we expected the shift in the ν_1 transition to be $\Delta\nu_1 = \nu_1 \Delta\nu_{UV}/\nu_{UV} = \pm$ 2 MHz for $\Delta\nu_{UV} = \mp$ 200 GHz detuning. The observed shift was $\approx$1 MHz, but within the statistical limits of 2 MHz. In reality, however, the UV-waveguide misalignment would have been much lower than the demonstrated UV detuning of $\Delta\nu_{UV} = \pm$ 200 GHz. The effect from second order Doppler shifts is expected to be $\nu_J \times v_x^2/2c^2$ = 1, 0.7, and 0.5 kHz for the ν_0, ν_1, and ν_2 transitions respectively.

4.4.2 Motional Stark Shifts

Ps atoms that are not moving parallel to a magnetic field can experience motional Stark shifts [98]. Although the UV laser selected atoms with small transverse speeds in the direction of the laser, atoms had large speeds in the y direction. An extreme case scenario can be considered: for atoms moving with speed 10^7 cm/s perpendicular to a 100 G magnetic field, the induced motional electric field ($\vec{F} = \vec{v} \times \vec{B}$) will be $\approx$ 10 V/cm.

In reality, as most of the atoms had lower transverse speeds, and were not travelling completely perpendicular to the magnetic field, the motional Stark shifts was much lower. The angular distribution of Ps atoms emitted from SiO_2 was approximated as a cosine distribution [115], which has been found to match well to the

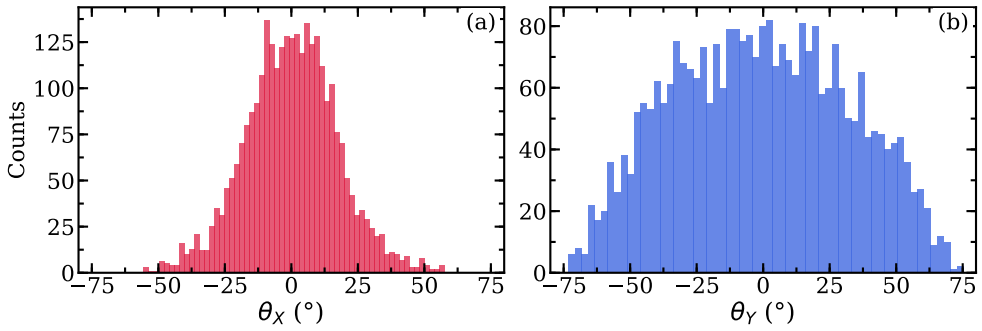

Figure 4.16: Simulated angular distribution of Ps emitted from SiO_2 in the x (a) and y (b) direction. The narrower distribution in x direction was a consequence of laser bandwidth selection as explained in the text.

measured distributions. The angular distributions in the x and y direction generated by a Monte-Carlo simulation are shown in figure 4.16. The x distribution is narrower than the y distribution due to the UV laser bandwidth selection. Most of the atoms were expected to be emitted within $\pm$ 55° in the y direction and thus, the motional Stark fields cannot be as large as estimated earlier. From figure 4.16 the average angle of emission in the y direction is calculated to be $\theta_{avg} \approx 27°$. The motional electric field due to atoms travelling with speed v_y^{rms} ($\approx v_x^{rms}$) = 9.3×10^4 m/s at θ_{avg} will then be 4.2 V/cm, which will cause a maximum Stark shift of $\approx$ +130 kHz.

The induced motional electric field is perpendicular to and linear in B. The Stark shift, however, has a quadratic dependence on the motional electric field, and therefore is proportional to B^2. As a result, any motional Stark shifts were also extrapolated to zero and did not contribute to the systematic error.

4.4.3 Stray Electric Fields

Although the waveguide was constructed out of solid aluminium and tungsten mesh (both being grounded during measurement) the presence of small stray DC electric fields due to impurities and patch potentials in the waveguide was possible. These kind of stray fields have been extensively studied and were reported to be limited to $\approx$ 100 mV [130, 131]. Rydberg atoms are highly sensitive to electric fields [43] and have been used to probe stray fields [132]. Stray fields generated

by surface impurities and imperfections on coplanar waveguide, designed to study He Rydberg-Rydberg transitions, were found to scale with the inverse square of the distance from the surface [133]. This provides a reasonable estimation of the magnitude of the stray fields that can be generated by bare metal surfaces.

Based on previous study of stray electric fields using Rydberg atoms [133], we estimate the dependence of the stray electric fields on distance to be no larger than $F_{\text{Stray}} \approx 3\times10^{-5}/d^2$ V/m. The calculated stray field strength as a function of distance is shown in figure 4.17(a). The estimated fields at a distance of $d = 100$ μm from the grids is ≈ 30 V/cm. At the centre of the WR-51 guide, $d = 3.25$ mm, the fields are estimated to be only 28 mV/cm. The average stray field across the WR-51 guide is then estimated to be 0.91 V/cm, which amounts to a Stark shift of +5.9, +6.3, and +6.5 kHz in the ν_0, ν_1, and ν_2 transitions respectively as shown in figure 4.17(b).

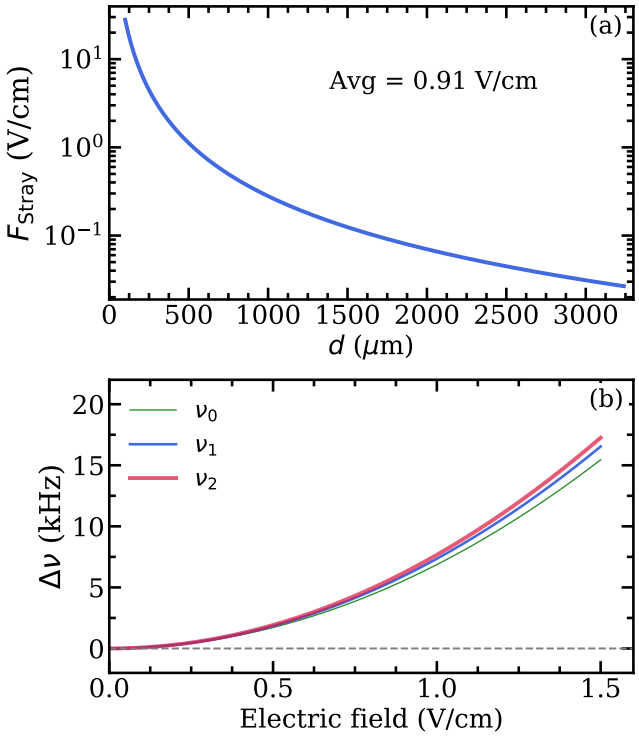

Figure 4.17: (a) Estimated magnitude of the stray electric fields as a function of distance from the grids. (b) Stark shift in the ν_J transitions as a function of electric field.

The WR-51 guide used in the ν_0 transition measurement is the narrowest and

is expected to have the higher mean stray fields than the other two waveguides. Therefore, 1 V/cm is taken to be the upper estimate of the stray field magnitude across all waveguides. In reality, the stray field magnitude is expected to be lower as the transitions are likely to happen away from the waveguide surfaces and near the middle of the waveguide where the field strength is lower. The maximum Stark shift in the ν_J transitions due to stray field of 1 V/cm is approximated to be $< +10$ kHz.

4.4.4 ac Stark Shifts

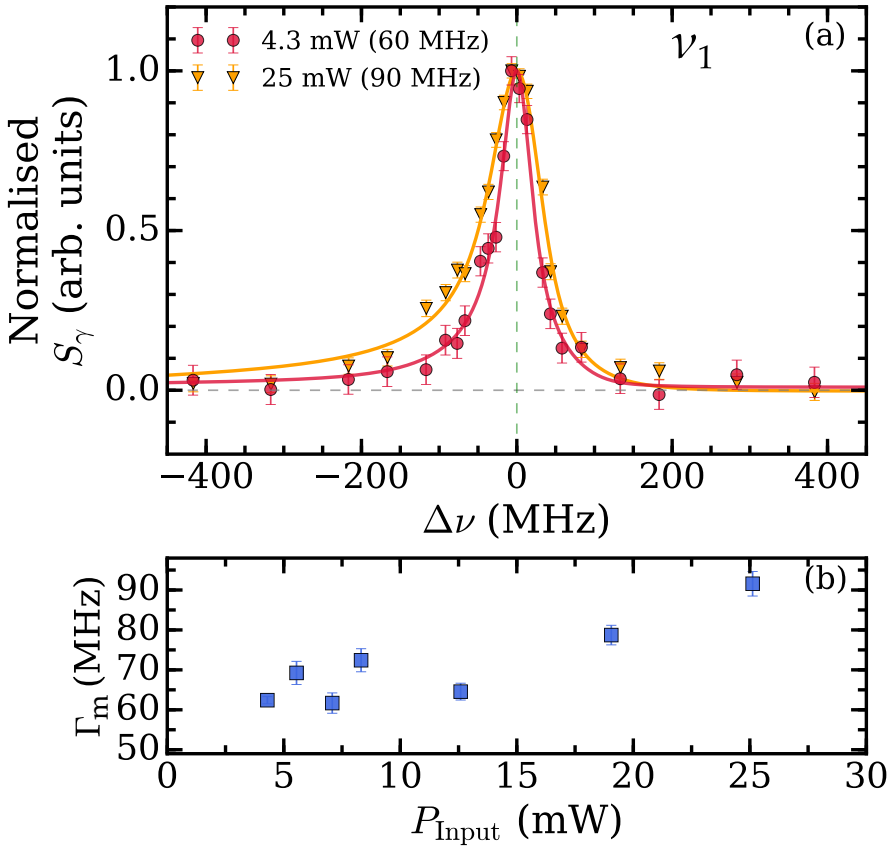

Figure 4.18: $2^3S_1 \rightarrow 2^3P_1$ transition lineshape (a), and the FWHM (b) as a function of the microwave power measured in a magnetic field of 82 G.

High powers of microwave radiation can induce ac Stark shifts and an accompanying line broadening would also be observed [93], as shown in figure 4.18(a). For $P_{\text{Input}} \approx 25$ mW, the linewidth is ≈ 90 MHz as shown in figure 4.18(b). As shown earlier in figure 4.2, the microwave radiation induced signal appears to be

saturated after $P_{\text{Input}} \approx 20$ mW and therefore, we estimate $P_{\text{Input}} \approx 25$ mW as the saturation intensity.

For 25% of this saturation intensity, $P_{\text{Input}} \approx 5$ mW, the measured linewidths (Γ_{m}) are ≈ 60 MHz, slightly wider than the natural linewidth ($\Gamma_0 = 50$ MHz), and was observed to be independent of power below 10 mW input. The microwave field strength at 5 mW is calculated to be 4.1 V/cm, which can create an ac Stark shift of +6.88, +6.78, and +7.79 kHz in the ν_0, ν_1, and ν_2 transitions respectively. Therefore, the ac Stark shift in all three transitions is estimated to be no larger than +10 kHz.

The magnitudes of the systematic uncertainties are summarised in table 4.1. The Stark shifts are in the positive direction only, but the total contribution is given in both directions (i.e, $\pm$) and is a conservative estimate.

Contribution	σ (kHz)		
	ν_0	ν_1	ν_2
Laser misalignment	$\pm$ 215	$\pm$ 150	$\pm$ 100
Second order Doppler	$\pm$ 1	$\pm$ 0.7	$\pm$ 0.5
Motional Stark	N/A	N/A	N/A
Stray electric fields	<+10	<+10	<+10
ac Stark	<+10	<+10	<+10
Total	$\pm$ 235	$\pm$ 170	$\pm$ 120

Table 4.1: List of systematic uncertainties in the $\nu_J = 2^3\text{S}_1 \rightarrow 2^3\text{P}_J$ ($J = 0, 1, 2$) transitions.

4.5 Results and Discussion

After taking the systematic effects into account, the resonance frequency of the ν_J transitions in the Ps $n = 2$ fine structure are summarised in table 4.2, where the statistical and systematic uncertainties have been added in quadrature. The current theoretical calculations [72] are also stated.

The ν_0 lineshapes are not asymmetric and therefore, both Lorentz and Fano functions yield similar values of ν_{R}. The measured ν_0 resonance frequency, however, is in disagreement with theory by ≈ 2.8 MHz (4.5σ). Fano profiles fits to

the ν_1 and ν_2 lineshapes indicate asymmetric lineshapes and as a result, the true resonance frequency of these transitions cannot be properly determined until the asymmetry is understood. The extracted ν_R values from Lorentz and Fano fits are different due to the asymmetric nature of the lineshapes. Furthermore, ν_R values from both methods are in disagreement with theoretical calculations by 2-4 MHz as summarised in table 4.2.

ν_J	Theory (MHz)	Exp: Lorentz (MHz)	Exp: Fano (MHz)	$\Delta\nu_L$ (MHz)	$\Delta\nu_F$ (MHz)
ν_0	18 498.25 ± 0.08	18 501.02 ± 0.62	18 501.09 ± 0.66	2.77	2.84
ν_1	13 012.41 ± 0.08	13 008.41 ± 0.55	13 014.13 ± 0.60	4	1.72
ν_2	8 626.71 ± 0.08	8 628.28 ± 0.37	8 624.68 ± 0.37	1.57	2.03

Table 4.2: Comparison of the current measurements, for both Lorentz (L) and Fano (F) fit results, and theoretical calculations of the Ps $n = 2$ fine structure intervals. The experimental uncertainties have been added in quadrature. The last two columns indicates the discrepancy between the theory and measurement (for Lorentz and Fano fits) in MHz. The theoretical values are from Ref. [72].

Shifts in line centre due to the interference effects considered in section 4.3 are too small to account for the observed shifts, and the systematic effects outlined in section 4.4 do not amount to the discrepancy seen in the ν_0 resonance frequency. Our measurements have improved upon the precision of the previous experiment [85] by a factor of ≈3-7 for the three transitions. Comparison with the previous measurements is presented in figure 4.19. The current ν_0 resonance frequency is in agreement with the value reported in Ref. [85] and the two results have been combined to calculate the average as indicated by the vertical dashed line in figure 4.19(a). As the resonance frequency of the ν_1 and ν_2 transitions are not properly determined, results from both Lorentz and Fano fits are presented. The Fano profile was only utilised to quantify the asymmetry in the ν_1 and ν_2 lineshapes, and it may be the case that the frequency at the position of the peak of the Fano profile is closer to the true resonance frequency than the Fano ν_R. Therefore, the frequency at the peak of the Fano lineshape is also shown in figures 4.19(b) and (c).

The two most precise measurements [80, 82] of the Ps hyperfine interval ($\Delta E_{\mathrm{hfs}}^{\mathrm{Ps}}$) were found to be in disagreement with theoretical calculations [75] by ≈

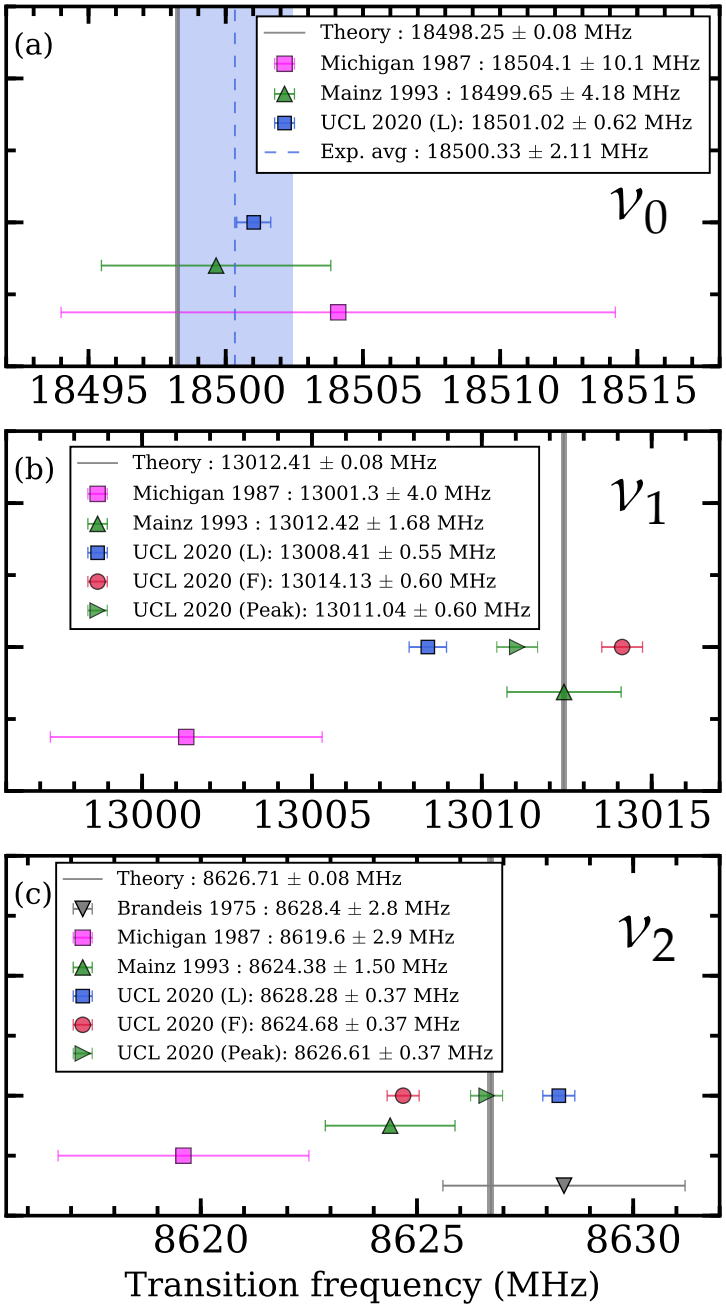

Figure 4.19: Comparison of the previous and the present measurements against theory for the (a) ν_0, (b) ν_1, and (c) ν_2 transitions. The current ν_0 resonance frequency has been combined with the result from Ref.[85] to calculate the average as indicated by the vertical dashed line in (a). Results from Lorentz (L) and Fano (F) line profile fits as well as the frequency at the peak position (Peak) of the Fano fits are shown for the current measurements of ν_1 and ν_2 intervals. The theoretical calculation is indicated by the vertical solid line in all panels. The statistical and systematic uncertainties have been added in quadrature.

4σ, as mentioned earlier in section 1.3.2. The HFS experiments relied on the use of N_2 buffer gas to produce positronium inside a microwave cavity. Several measurements were performed at high gas pressures and then extrapolated to zero pressure to find the true HFS interval frequency, which disagreed with theory. Effects from non-thermal Ps, which were also present in the now resolved 'ortho-positronium lifetime puzzle' [36], are believed to the source of the disagreement. An experiment designed to account for non-thermalised Ps effects was performed [81] and found to be in agreement with theory, but disagreed with previous experiments by 2.6σ. The precision of the new experiment was, however, smaller by a factor of $\approx$ 3 compared to previous measurements, and more precise and independent measurements are needed to properly understand the HFS interval issue.

The non-uniformity of the static magnetic field was also believed to be another source of the disagreement. This magnitude of this effect was estimated to contribute 3 ppm in the work done by Ishida and colleagues. A direct measurement of $\Delta E_{\mathrm{hfs}}^{\mathrm{Ps}}$ has also been performed [134], but the precision of the experiment (800 ppm) is not yet comparable to the more precise measurements. High power (over 20 kW) of microwave radiation is required as the transition is strongly suppressed. Better measurements which include high intensity positron beam, Ps production in vacuum as opposed to gas chamber, and higher microwave powers are expected to improve the precision of the direct HFS measurement. If measurements of $\Delta E_{\mathrm{hfs}}^{\mathrm{Ps}}$, both direct and indirect, are performed with comparable precision to theoretical calculations and disagreement still persists, then it could indicate a contribution from new physics.

The systematic errors that dominated the $\Delta E_{\mathrm{hfs}}^{\mathrm{Ps}}$ are either negligible or absent in our experiments. We utilised a SiO_2 film to produce Ps atoms, which were emitted into vacuum. Therefore, the Stark effect due to Ps production in gas cells are absent. Stark effects could be generated by stray fields, but are not expected to contribute to more than +10 kHz shift, and therefore are not the source of the disagreement. The variation of the magnetic field in the waveguide was found to be less than $\pm$

1 G at both ends of the magnetic field range used in our measurements. Therefore, the static magnetic field was essentially uniform in the region encompassed by the Ps atoms and not expected to cause unknown Zeeman shifts.

Ps atoms were produced with near-thermal velocity in our measurements, which were significantly colder than the 2^3S_1 atoms utilised in the previous experiment [85]. Doppler and ac Stark effects were minimised as a result, but transit time broadening still contributed to $\approx$ 10 MHz broadening of the lineshapes. This effect only leads to broadening and not in shift of the line centre. As higher powers of radiation were needed in the previous experiment [85], linewidths were $\approx$ 85 MHz, but lineshapes did not appear asymmetric. Our measurements conducted at P_{Input} = 25 mW broadened the lineshape to $\approx$ 90 MHz, but were still asymmetric. The asymmetry parameter, q, did not exhibit any significant dependence on the magnetic field as shown in figure 4.10, suggesting that the asymmetry was not introduced by the magnetic field. Measurement in a field free region is required to investigate whether this is the case. A proper understanding of the asymmetry is warranted as it prevents the determination of the ν_1 and ν_2 transition frequencies.

The ν_0 lineshapes are not asymmetric, but exhibit a disagreement with theoretical calculations. This may be an indication that the source of the asymmetry and line centre shifts are not the same, while the former may also cause additional line shifts. Therefore, it may be necessary to account for both effects in future experiments.

4.6 Future Work

To investigate the disagreement of the ν_0 resonance frequency with theory, the asymmetry in the ν_1 and ν_2 lineshapes, and achieve a higher precision, a number of improvements to the next generation of fine structure measurements can be considered.

One difference between our method and the previous experiments is the pres-

ence of the axial magnetic field during the transition. This introduced Zeeman shifts in our measurements, which are particularly large for the ν_1 and ν_2 transitions. Several measurements at a range of applied magnetic field were taken to account for the Zeeman effect. In the next iteration the positron beam can be extracted out of the magnetic field using electrostatic lenses. This will reduce Zeeman shifts to negligible levels. An experiment involving two-stage extraction of electron plasmas to zero magnetic field and focussing through an Einzel lens demonstrated that approximately 55% of the electron plasma was extracted [135]. This technique can also be applied to positron beams, with the possibility of using re-moderation techniques to enhance the beam brightness [136].

Residual electric and magnetic fields can be probed with a Rydberg He beam. Atoms and molecules in highly excited or Rydberg states [43] are extremely sensitive to weak electromagnetic fields and therefore, can be utilised as electric field probes [132, 137]. Microwave spectroscopy of Rydberg He beam will be utilised to probe and characterise stray fields in the microwave guide by studying Stark and Zeeman effects on the fine structure of He Rydberg states [138]. This would be followed by the application of field cancellation techniques to minimise the residual fields in the microwave guide [138].

Construction of a He beam source is now underway in UCL. A schematic representation of what the Rydberg He probe experiment could look like is illustrated in figure 4.20. A supersonic source of metastable He, following the injection of electrons into a helium discharge, can be excited to Rydberg states with a laser [139]. The stray fields inside the waveguide can then be characterised with spectroscopy of the He* states, with the field ionisation plates and MCP providing a detection mechanism. The Ps forming target (SiO_2) is mounted on a *xyz* manipulator to allow the He beam entry into the waveguide.

Although Ps atoms emitted from SiO_2 films are divergent, the 100 GHz bandwidth of the UV laser only selects atoms with low transverse speeds. Doppler effects can still be present due to possible misalignment of the laser and the waveguide, and

currently contributes to the largest source of systematic error in our measurements. To evaluate this effect, a second microwave antenna can be added to the waveguide as shown in figure 4.20. Measurements with microwave radiation propagating in either direction (i.e., $+x$ or $-x$) will then be taken to obtain a Doppler free averaged value, thereby improving the precision. Utmost care will have to taken to ensure that the response of the individual antennas are as identical as possible to avoid unquantifiable frequency dependent effects.

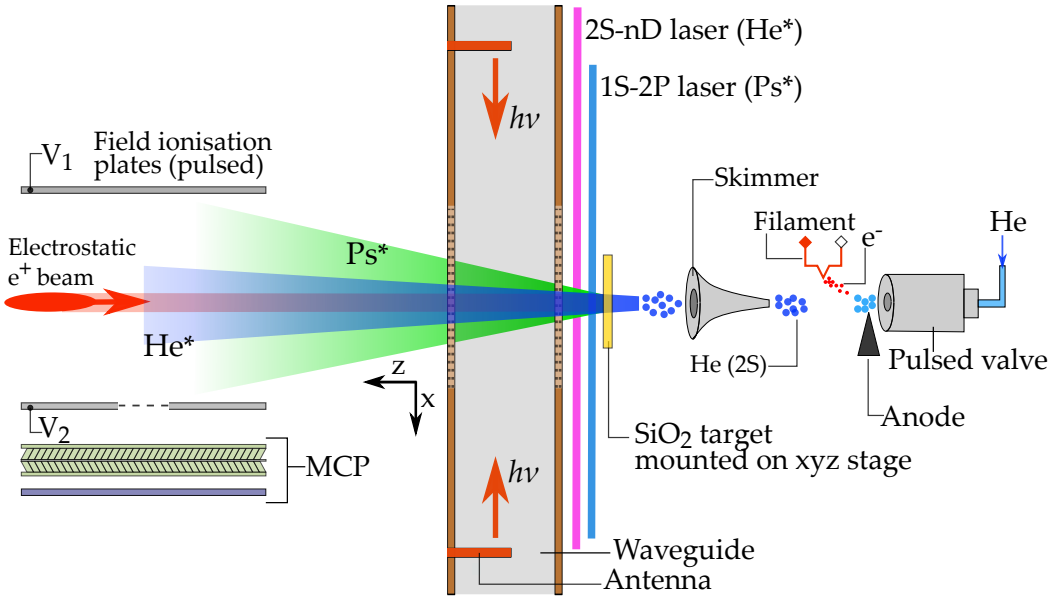

Figure 4.20: Schematic setup of a possible Rydberg He and Ps microwave spectroscopy experiment. With the SiO_2 retracted, Rydberg He can probe the waveguide. The gamma-ray detectors for Ps detection are not shown. Adapted from [33].

Porous SiO_2 films typically produce Ps atoms with energies of ≈ 50 meV. If the positrons are implanted with higher energy into the film or late atoms emitted from the film are excited, the Ps energy may be lower at ≈ 30 meV. Metals such as Ag and Cu can also be used to produce Ps atoms. Unlike in porous insulators, Ps formation cannot occur in the bulk of metals due to the high density of free electrons. Thermalised positrons can diffuse back to the surface of the metal and be trapped in a surface-state localised within a few angstroms outside the surface [140, 141]. The trapped positrons can interact with surface electrons and form Ps atoms. Efficient emission of Ps atoms with beam-Maxwellian distribution can be obtained [142–

144]. Oxygen treated Al has been shown to produce Ps atoms with energies of $\approx$ 10 meV [117] with efficiency of $\approx$ 12%. This technique, however, requires the Al target to be cleaned and held at cryogenic temperatures, which requires careful maintenance and handling.

Single photon excitation to produce Ps atoms in the metastable 2^3S_1 state is more efficient than producing excited states naturally [85], but a two-photon Doppler free excitation scheme [54] can offer greater efficiency. Implementation of a Doppler free excitation scheme is also underway in UCL and is expected to provide improved statistics in the next iteration of measurements. In this method, atoms in 1^3S_1 state are excited to the 2^3S_1 state with two streams of counter-propagating 486 nm light. The Doppler shift arising from the two photons are equal and opposite in magnitude: therefore, first order Doppler broadening will be eliminated. A drawback of this method is that the excitation laser is also capable of ionising the 2^3S_1 atoms if the light intensity is increased, thereby placing an upper limit on the excitation efficiency of $\approx$ 18% [145]. This scheme will be coupled with a SiO_2 target initially and several metal targets will also be tested. Statistics can be further improved by increasing the detection area range, either by using larger scintillators or adding more gamma-ray detectors.

All of these intended additions will provide a more precise measurement of the $n = 2$ fine structure intervals and offer more insight into the source of the asymmetry and disagreement with theoretical calculations. It may be the case that asymmetry in the lineshapes due to interference effects are not avoidable. In that case simulations that can provide corrections, or sophisticated lineshape models may be necessary [94, 126, 146]. Instead of using a single microwave pulse, techniques that utilise a pair of short pulses separated by some time interval, in which one can be in or out of phase with the other, have also been developed. This separated oscillatory fields (SOF) method [147, 148] was first introduced by Norman Ramsey and has the advantage of producing narrower resonance lines than a single pulse method. Shifts in line centre due to quantum interference effects are still observed

in the SOF methods, but are much smaller in magnitude than traditional single pulse methods [125, 127].

An extension of the SOF technique in which the frequencies of the two pulses are offset have also been developed and is known as the frequency-offset separated oscillatory fields (FOSOF) method [149]. The FOSOF method is insensitive to small variations introduced by frequency response of the system and has the added benefit that understanding of complicated lineshapes are not required. The obtainable precision in non FOSOF methods may be limited by the large number of parameters required to fit a lineshape to data and thus, can limit the knowledge of systematic effects which may be absorbed into the fit results. The FOSOF technique measures the phase difference between the signal and background to produce a straight-line 'lineshape' from which the resonance frequency can be extracted [150, 151]. The $n = 2$ triplet P fine structure in helium has been measured to a precision of 25 Hz (< 1 ppb) by utilising the FOSOF technique [150]. Ultimately, to achieve sub-kHz precision measurement of the Ps energy intervals, techniques such as SOF or FOSOF may need to be employed.

Chapter 5

Conclusions

As an entirely leptonic system, positronium is an excellent test-bed for QED studies through precision spectroscopy of its energy structure. The hyperfine structure intervals ($1^3S_1 \rightarrow 1^1S_0$), the $1^3S_1 \rightarrow 2^3S_1$ transition, and the fine structure intervals ($2^3S_1 \rightarrow 2^3P_J$, J = 0,1,2) have all been measured previously. Theoretical calculations of these transitions have been carried out to precision better than measurements. Most of these energies, including the $n = 2$ fine structure intervals have not been recently measured. It was therefore necessary to conduct new measurements in order to improve the experimental precision.

With that goal in mind, a new measurement of the $n = 2$ fine structure intervals was presented in this thesis. Positrons from a radioactive ^{22}Na source were accumulated in a Surko buffer-gas trap (section 3.3) allowing intense pulses of positrons to be injected into a mesoporous silica target (section 3.4). These targets produced ground state Ps atoms with energy around 50 meV which were then optically excited to the 2^3S_1 state (section 3.8) before entering a microwave guide. As the atoms travelled through the guide, the $\nu_J = 2^3S_1 \rightarrow 2^3P_J$ ($J = 0, 1, 2$) transitions were then driven with microwave radiation. Once the 2^3P_J radiated to the ground state, the change in the lifetime spectra recorded by the gamma-ray detectors were analysed to quantify the microwave induced signal (section 3.6). The use of slow Ps atoms to generate 2^3S_1 state, coupled with a more efficient detection scheme has yielded res-

onance frequency of 18501.02 $\pm$ 0.62 MHz for the ν_0 transition. While this result represents a $\approx$7 fold improvement in precision over the previous experiment [85], it is, however, in 4.5σ disagreement with the current theoretical value of 18498.25 $\pm$ 0.08 MHz as summarised in table 4.2 and figure 4.19. The ν_1 and ν_2 transition lineshapes, unlike the ν_0 lineshape, are asymmetric. The source of the asymmetry is not presently known and thus, prevents the determination of the resonance frequency of the transitions. The source of the asymmetry and the origin of the shift in the ν_0 interval are not expected to be the same as the ν_0 lineshape is not asymmetric.

To account for the observed disagreement and investigate the asymmetry, several possible improvements were outlined in section 4.6 and steps to implement these improvements have already been taken. As Ps is extremely well described by QED theory, any significant deviation from theory could be a possible indication of new physics. In this scenario, all possible sources of discrepancy should be investigated and it is expected that future iterations of the fine structure measurements will provide more precise and accurate answers. It is also important to perform independent measurements in order to understand and eliminate any systematic effects. Measurement of the $n = 2$ intervals presented here is a step towards conducting Ps experiments with precision comparable to theory [67].

Bibliography

[1] L. Gurung, T. J. Babij, S. D. Hogan, and D. B. Cassidy. Precision Microwave Spectroscopy of the Positronium $n = 2$ Fine Structure. *Phys. Rev. Lett.*, 125:073002, 2020.

[2] L. Gurung, T. J. Babij, J. Pérez-Ríos, S. D. Hogan, and D. B. Cassidy. Observation of asymmetric lineshapes in precision microwave spectroscopy of the positronium 2^3S_1-2^3P_j (J=1,2) fine structure intervals. *Phys. Rev. A*, (Accepted).

[3] L. Gurung, T. J. Babij, and D. B. Cassidy. Fast decay of 2^3S_1 positronium atoms in an MgO lined cavity. *EPJ Techniques and Instrumentation*, 8(1):3, 2021.

[4] R. E. Sheldon, T. J. Babij, B. A. Devlin-Hill, L. Gurung, and D. B. Cassidy. Measurement of the annihilation decay rate of 2^3S_1 positronium. *EPL*, 132(1):13001, 2020.

[5] L. Gurung, B. S. Cooper, S. D. Hogan, and D. B. Cassidy. Resonant shifts of positronium energy levels in MgO powder. *Phys. Rev. A*, 101:012701, 2020.

[6] M. H. Rayment, L. Gurung, R. E. Sheldon, S. D. Hogan, and D. B. Cassidy. Multiring electrostatic guide for Rydberg positronium. *Phys. Rev. A*, 100:013410, 2019.

[7] L. Gurung, A. M. Alonso, T. J. Babij, B. S. Cooper, A. L. Shluger, and D. B.

Cassidy. Positronium emission from MgO smoke nanocrystals. *Journal of Physics B: Atomic, Molecular and Optical Physics*, 52:105004, 2019.

[8] A. M. Alonso, L. Gurung, B. A. D. Sukra, S. D. Hogan, and D. B. Cassidy. State-selective electric-field ionization of Rydberg positronium. *Phys. Rev. A*, 98:053417, 2018.

[9] B. S. Cooper, J.-P. Boilot, C. Corbel, F. Guillemot, L. Gurung, L. Liszkay, and D. B. Cassidy. Annihilation of positronium atoms confined in mesoporous and macroporous SiO2 films. *Phys. Rev. B*, 97:205302, 2018.

[10] A. M. Alonso, B. S. Cooper, A. Deller, L. Gurung, S. D. Hogan, and D. B. Cassidy. Velocity selection of Rydberg positronium using a curved electrostatic guide. *Phys. Rev. A*, 95:053409, 2017.

[11] A. M. Alonso, S. D. Hogan, and D. B. Cassidy. Production of $2\,^3S_1$ positronium atoms by single-photon excitation in an electric field. *Phys. Rev. A*, 95:033408, 2017.

[12] A. M. Alonso, B. S. Cooper, A. Deller, and D. B. Cassidy. Single-shot positron annihilation lifetime spectroscopy with LYSO scintillators. *NIM A*, 828:163 – 169, 2016.

[13] A. M. Alonso, B. S. Cooper, A. Deller, S. D. Hogan, and D. B. Cassidy. Positronium decay from $n = 2$ states in electric and magnetic fields. *Phys. Rev. A*, 93:012506, 2016.

[14] A. M. Alonso, B. S. Cooper, A. Deller, S. D. Hogan, and D. B. Cassidy. Controlling Positronium Annihilation with Electric Fields. *Phys. Rev. Lett.*, 115:183401, 2015.

[15] B. S. Cooper, A. M. Alonso, A. Deller, T. E. Wall, and D. B. Cassidy. A trap-based pulsed positron beam optimised for positronium laser spectroscopy. *Review of Scientific Instruments*, 86:103101, 2015.

[16] A. Deller, B. S. Cooper, T. E. Wall, and D. B. Cassidy. Positronium emission from mesoporous silica studied by laser-enhanced time-of-flight spectroscopy. *New J. Phys.*, 17:043059, 2015.

[17] P. A. M. Dirac. The Quantum Theory of the Electron. *Proc. R. Soc. Lond. A: Math., Phys. and Eng. Sci.*, 117:610, 1928a.

[18] P. A. M. Dirac. The Quantum Theory of the Electron. Part II. *Proc. R. Soc. Lond. A: Math., Phys. and Eng. Sci.*, 118:351, 1928b.

[19] P. A. M. Dirac. A Theory of Electrons and Protons. *Proc. R. Soc. Lond. A: Math., Phys. and Eng. Sci.*, 126:360, 1930.

[20] P. A. M. Dirac. Quantised singularities in the electromagnetic field. *Proc. R. Soc. Lond. A: Math., Phys. and Eng. Sci.*, 133:60, 1931.

[21] C. D. Anderson. The Positive Electron. *Phys. Rev.*, 43:491–494, 1933.

[22] S. Mohorovičić. Möglichkeit neuer Elemente und ihre Bedeutung für die Astrophysik. *Astronomische Nachrichten*, 253:93–108, 1934.

[23] J. A. Wheeler. Polyelectrons. *Ann. N. Y. Acad. Sci.*, 48:219–238, 1946.

[24] A. E. Ruark. Positronium. *Phys. Rev.*, 68:278–278, 1945.

[25] M. Deutsch. Evidence for the Formation of Positronium in Gases. *Phys. Rev.*, 82:455–456, 1951.

[26] S. Berko and H. N. Pendleton. Positronium. *Annu. Rev. Nucl. Part. Sci.*, 30:543–581, 1980.

[27] A. Rich. Recent experimental advances in positronium research. *Rev. Mod. Phys.*, 53:127–165, 1981.

[28] C. Foot. *Atomic Physics*. Oxford master series in Physics. Oxford University Press, 2005.

[29] J. Pirenne. Ph.D Thesis, University of Paris, 1944.

[30] H. Hellwig, R. F. C. Vessot, M. W. Levine, P. W. Zitzewitz, D. W. Allan, and D. J. Glaze. Measurement of the Unperturbed Hydrogen Hyperfine Transition Frequency. *IEEE Transactions on Instrumentation and Measurement*, 19:200–209, 1970.

[31] V. B. Berestetski. On the spectrum of system consisting of a positron and electron. *J. Exp. Theor. Phys. (U.S.S.R.)*, 19:1130, 1949.

[32] R. A. Ferrell. The Positronium Fine Structure. *Phys. Rev.*, 84:858–859, 1951.

[33] D. B Cassidy. Experimental progress in positronium laser physics. *Eur. Phys. J. D*, 72, 2018.

[34] A. Ore and J. L. Powell. Three-Photon Annihilation of an Electron-Positron Pair. *Phys. Rev.*, 75:1696–1699, 1949.

[35] A. H. Al-Ramadhan and D. W. Gidley. New precision measurement of the decay rate of singlet positronium. *Phys. Rev. Lett.*, 72:1632–1635, 1994.

[36] R. S. Vallery, P. W. Zitzewitz, and D. W. Gidley. Resolution of the Orthopositronium-Lifetime Puzzle. *Phys. Rev. Lett.*, 90:203402, 2003.

[37] A. I. Alekseev. Two-Photon Annihilation of Positronium in the P-State. *Soviet Phys. JETP*, 7:826, 1958.

[38] A. I. Alekseev. Three-Photon Annihilation of Positronium in the P-State. *Soviet Phys. JETP*, 9:1312, 1959.

[39] P. Wallyn, W. A. Mahoney, Ph. Durouchoux, and C. Chapuis. The Positronium Radiative Combination Spectrum: Calculation in the Limit of Thermal Positrons and Low Densities. *Astrophysical Journal*, 465:473, 1996.

[40] P. A. M. Dirac. On the Annihilation of Electrons and Protons. *Math. Proc. Camb. Phil. Soc.*, 26:361, 1930.

[41] J. Shapiro and G. Breit. Metastability of 2s States of Hydrogenic Atoms. *Phys. Rev.*, 113:179–181, 1959.

[42] H. A. Bethe and E. E. Salpeter. *Quantum Mechanics of One- and Two-Electron Atoms*. Springer, Berlin, 1957.

[43] T. F. Gallagher. *Rydberg Atoms*. Cambridge Unvieristy Press, 1994.

[44] A. Deller, A. M. Alonso, B. S. Cooper, S. D. Hogan, and D. B. Cassidy. Measurement of Rydberg positronium fluorescence lifetimes. *Phys. Rev. A*, 93:062513, Jun 2016.

[45] K P Ziock, C D Dermer, R H Howell, F Magnotta, and K M Jones. Optical saturation of the 1^3S-2^3S transition in positronium. *Journal of Physics B: Atomic, Molecular and Optical Physics*, 23:329–336, 1990.

[46] C. N. Yang. Selection Rules for the Dematerialization of a Particle into Two Photons. *Phys. Rev.*, 77:242–245, 1950.

[47] L. Wolfenstein and D. G. Ravenhall. Some Consequences of Invariance under Charge Conjugation. *Phys. Rev.*, 88:279–282, 1952.

[48] K. F. Canter, A. P. Mills Jr., and S. Berko. Observations of positronium Lyman-α radiation. *Phys. Rev. Lett.*, 34:177–180, 1975.

[49] H. W. Kendall. Ph.D Thesis, M.I.T, 1954.

[50] V. W. Hughes. Positronium Formation in Gases. *Journal of Applied Physics*, 28:16–22, 1957.

[51] M. Leventhal. Search for positronium Lyman alpha-radiation from positrons stopped in inert gases. *Proc. Natl. Acad. Sci.*, 66:6–12, 1970.

[52] S. Chu and A. P. Mills Jr. Excitation of the positronium 1^3S_1 - 2^3S_1 two-photon transition. *Phys. Rev. Lett.*, 48:1333–1337, 1982.

[53] S. Chu, A. P. Mills Jr., and J. L. Hall. Measurement of the positronium 1^3S_1 - 2^3S_1 interval by Doppler-Free two-photon spectroscopy. *Phys. Rev. Lett.*, 52:1689–1692, 1984.

[54] M. S. Fee, A. P. Mills Jr., S. Chu, E. D. Shaw, K. Danzmann, R. J. Chichester, and D. M. Zuckerman. Measurement of the positronium 1^3S_1–2^3S_1 interval by continuous-wave two-photon excitation. *Phys. Rev. Lett.*, 70:1397–1400, 1993.

[55] K. P. Ziock, R. H. Howell, F. Magnotta, R. A. Failor, and K. M. Jones. First observation of resonant excitation of high-*n* states in positronium. *Phys. Rev. Lett.*, 64:2366–2369, 1990.

[56] C. M. Surko, M. Leventhal, and A. Passner. Positron Plasma in the Laboratory. *Phys. Rev. Lett.*, 62:901–904, 1989.

[57] D. B. Cassidy, P. Crivelli, T. H. Hisakado, L. Liszkay, V. E. Meligne, P. Perez, H. W. K. Tom, and A. P. Mills Jr. Positronium cooling in porous silica measured via Doppler spectroscopy. *Phys. Rev. A*, 81:012715, 2010.

[58] D. B. Cassidy, T. H. Hisakado, H. W. K. Tom, and A. P. Mills Jr. Efficient production of Rydberg positronium. *Phys. Rev. Lett.*, 108:043401, 2012.

[59] S. Aghion, C. Amsler, A. Ariga, T. Ariga, G. Bonomi, P. Bräunig, J. Bremer, R. S. Brusa, L. Cabaret, M. Caccia, R. Caravita, F. Castelli, G. Cerchiari, K. Chlouba, S. Cialdi, D. Comparat, G. Consolati, A. Demetrio, L. Di Noto, M. Doser, A. Dudarev, A. Ereditato, C. Evans, R. Ferragut, J. Fesel, A. Fontana, O. K. Forslund, S. Gerber, M. Giammarchi, A. Gligorova, S. Gninenko, F. Guatieri, S. Haider, H. Holmestad, T. Huse, I. L. Jernelv, E. Jordan, A. Kellerbauer, M. Kimura, T. Koettig, D. Krasnicky, V. Lagomarsino, P. Lansonneur, P. Lebrun, S. Lehner, J. Liberadzka, C. Malbrunot, S. Mariazzi, L. Marx, V. Matveev, Z. Mazzotta, G. Nebbia, P. Nedelec, M. Oberthaler, N. Pacifico, D. Pagano, L. Penasa, V. Petracek, C. Pistillo, F. Prelz, M. Prevedelli, L. Ravelli, L. Resch, B. Rienäcker, O. M. Røhne, A. Rotondi, M. Sacerdoti, H. Sandaker, R. Santoro, P. Scampoli, L. Smestad, F. Sorrentino, M. Spacek, J. Storey, I. M. Strojek, G. Testera, I. Tietje, S. Vamosi, E. Widmann, P. Yzombard, J. Zmeskal, and N. Zurlo. Laser excitation

of the $n = 3$ level of positronium for antihydrogen production. *Phys. Rev. A*, 94:012507, 2016.

[60] A. C. L. Jones, J. Moxom, H. J. Rutbeck-Goldman, K. A. Osorno, G. G. Cecchini, M. Fuentes-Garcia, R. G. Greaves, D. J. Adams, H. W. K. Tom, A. P. Mills Jr., and M. Leventhal. Focusing of a Rydberg positronium beam with an ellipsoidal electrostatic mirror. *Phys. Rev. Lett.*, 119:053201, 2017.

[61] D. B. Cassidy, S. H. M. Deng, R. G. Greaves, and A. P. Mills Jr. Accumulator for the production of intense positron pulses. *Review of Scientific Instruments*, 77:073106, 2006.

[62] T. E. Wall, A. M. Alonso, B. S. Cooper, A. Deller, S. D. Hogan, and D. B. Cassidy. Selective production of Rydberg-Stark states of positronium. *Phys. Rev. Lett.*, 114:173001, Apr 2015.

[63] A. Deller, A. M. Alonso, B. S. Cooper, S. D. Hogan, and D. B. Cassidy. Electrostatically Guided Rydberg Positronium. *Phys. Rev. Lett.*, 117:073202, August 2016.

[64] D. B. Cassidy and A. P. Mills Jr. The production of molecular positronium. *Nature*, 449:195–197, 2007.

[65] D. B. Cassidy, T. H. Hisakado, H. W. K. Tom, and A. P. Mills Jr. Optical spectroscopy of molecular positronium. *Phys. Rev. Lett.*, 108:133402, Mar 2012.

[66] P. M. Platzman and A. P. Mills Jr. Possibilities for Bose condensation of positronium. *Phys. Rev. B*, 49:454–458, Jan 1994.

[67] S. G. Karshenboim. Precision study of positronium: Testing bound state QED theory. *Int. J. Mod. Phys. A*, 19:3879–3896, 2004.

[68] M. S. Safronova, D. Budker, D. DeMille, Derek F. Jackson Kimball, A. Derevianko, and Charles W. Clark. Search for new physics with atoms and molecules. *Rev. Mod. Phys.*, 90:025008, Jun 2018.

[69] Henry Lamm. $p-$state positronium for precision physics: An ultrafine splitting at α^6. *Phys. Rev. A*, 96:022515, Aug 2017.

[70] Krzysztof Pachucki and Savely G. Karshenboim. Complete results for positronium energy levels at order $m\alpha^6$. *Phys. Rev. Lett.*, 80:2101–2104, Mar 1998.

[71] A. Czarnecki, K. Melnikov, and A. Yelkhovsky. Positronium Hyperfine Splitting: Analytical Value at o$(m\alpha^6)$. *Phys. Rev. Lett.*, 82:311–314, 1999.

[72] A. Czarnecki, K. Melnikov, and A. Yelkhovsky. Positronium S-state spectrum: Analytic results at o$(m\alpha^6)$. *Phys. Rev. A*, 59:4316–4330, 1999.

[73] J. Zatorski. O$(m\alpha^6)$ corrections to energy levels of positronium with non-vanishing orbital angular momentum. *Phys. Rev. A*, 78:032103, Sep 2008.

[74] Krzysztof Pachucki and Savely G. Karshenboim. Higher-order recoil corrections to energy levels of two-body systems. *Phys. Rev. A*, 60:2792–2798, Oct 1999.

[75] Bernd A. Kniehl and Alexander A. Penin. Order $\alpha^3 \ln(1/\alpha)$ corrections to positronium decays. *Phys. Rev. Lett.*, 85:1210–1213, Aug 2000.

[76] M. Baker, P. Marquard, A. A. Penin, J. Piclum, and M. Steinhauser. Hyperfine splitting in positronium to o$(\alpha^7 m_e)$: One photon annihilation contribution. *Phys. Rev. Lett.*, 112:120407, Mar 2014.

[77] Gregory S. Adkins, Minji Kim, Christian Parsons, and Richard N. Fell. Three-photon-annihilation contributions to positronium energies at order $m\alpha^7$. *Phys. Rev. Lett.*, 115:233401, Dec 2015.

[78] Gregory S. Adkins, Lam M. Tran, and Ruihan Wang. Positronium energy levels at order $m\alpha^7$: Product contributions in the two-photon-annihilation channel. *Phys. Rev. A*, 93:052511, May 2016.

[79] Martin Deutsch and Sanborn C. Brown. Zeeman effect and hyperfine splitting of positronium. *Phys. Rev.*, 85:1047–1048, Mar 1952.

[80] A. P. Mills Jr. Line-shape effects in the measurement of the positronium hyperfine interval. *Phys. Rev. A*, 27:262–267, Jan 1983.

[81] A. Ishida, T. Namba, S. Asai, T. Kobayashi, H. Saito, M. Yoshida, K. Tanaka, and A. Yamamoto. New precision measurement of hyperfine splitting of positronium. *Physics Letters B*, 734:338 – 344, 2014.

[82] M. W. Ritter, P. O. Egan, V. W. Hughes, and K. A. Woodle. Precision determination of the hyperfine-structure interval in the ground state of positronium. v. *Phys. Rev. A*, 30:1331–1338, 1984.

[83] A. P. Mills Jr., S. Berko, and K. F. Canter. Fine-structure measurement in the first excited state of positronium. *Phys. Rev. Lett.*, 34:1541–1544, Jun 1975.

[84] S. Hatamian, R. S. Conti, and A. Rich. Measurements of the 2^3S_1-2^3P_j (J=0,1,2) fine-structure splittings in positronium. *Phys. Rev. Lett.*, 58:1833–1836, May 1987.

[85] D. Hagena, R. Ley, D. Weil, G. Werth, W. Arnold, and H. Schneider. Precise measurement of $n = 2$ positronium fine-structure intervals. *Phys. Rev. Lett.*, 71:2887–2890, 1993.

[86] M. S. Fee, S. Chu, A. P. Mills Jr., R. J. Chichester, D. M. Zuckerman, E. D. Shaw, and K. Danzmann. Measurement of the positronium 1^3S_1–2^3S_1 interval by continuous-wave two-photon excitation. *Phys. Rev. A*, 48:192–219, Jul 1993.

[87] R.S. Conti, S. Hatamian, L. Lapidus, A. Rich, and M. Skalsey. Search for C-violating, P-conserving interactions and observation of 2^3S_1 to 2^1P_1 transitions in positronium. *Physics Letters A*, 177:43 – 48, 1993.

[88] R. Ley, D. Hagena, D. Weil, G. Werth, W. Arnold, and H. Schneider. Spectroscopy of excited state positronium. *Hyperfine Interactions*, 89:327–341, Dec 1994.

[89] D. W. Gidley, P. W. Zitzewitz, K. A. Marko, and A. Rich. Measurement of the vacuum decay rate of orthopositronium. *Phys. Rev. Lett.*, 37:729–732, Sep 1976.

[90] C. I. Westbrook, D. W. Gidley, R. S. Conti, and A. Rich. Precision measurement of the orthopositronium vacuum decay rate using the gas technique. *Phys. Rev. A*, 40:5489–5499, Nov 1989.

[91] J. S. Nico, D. W. Gidley, A. Rich, and P. W. Zitzewitz. Precision measurement of the orthopositronium decay rate using the vacuum technique. *Phys. Rev. Lett.*, 65:1344–1347, Sep 1990.

[92] O Jinnouchi, S Asai, and T. Kobayashi. Precision measurement of orthopositronium decay rate using SiO_2 powder. *Physics Letters B*, 572:117 – 126, 2003.

[93] W. Demtroder. *Laser Spectroscopy*. Springer, New York, 4 edition, 2008.

[94] A. Beyer, L. Maisenbacher, A. Matveev, R. Pohl, K. Khabarova, A. Grinin, T. Lamour, D. C. Yost, T. W. Hänsch, N. Kolachevsky, and T. Udem. The Rydberg constant and proton size from atomic hydrogen. *Science*, 358:79–85, 2017.

[95] R. Pohl, R. Gilman, G. A. Miller, and K. Pachucki. Muonic Hydrogen and the Proton Radius Puzzle. *Annual Review of Nuclear and Particle Science*, 63:175–204, 2013.

[96] G. S. Adkins and N. M. McGovern. Application of the effective interaction method to the relativistic Coulomb problem. *American Journal of Physics*, 73:759–770, 2005.

[97] Thomas Fulton and Paul C. Martin. Two-Body System in Quantum Electrodynamics. Energy Levels of Positronium. *Phys. Rev.*, 95:811–822, Aug 1954.

[98] S. M. Curry. Combined Zeeman and Motional Stark effects in the first excited state of positronium. *Phys. Rev. A*, 7:447–450, 1973.

[99] C. D. Dermer and J. C. Weisheit. Perturbative analysis of simultaneous Stark and Zeeman effects on n=1 - n=2 radiative transitions in positronium. *Phys. Rev. A*, 40:5526–5532, Nov 1989.

[100] V. W. Hughes, S. Marder, and C. S. Wu. Hyperfine structure of positronium in its ground state. *Phys. Rev.*, 106:934–947, 1957.

[101] G. Breit and I. I. Rabi. Measurement of nuclear spin. *Phys. Rev.*, 38:2082–2083, Dec 1931.

[102] H. Grotch and R. Kashuba. Magnetic interactions of one-electron atoms and of positronium. *Phys. Rev. A*, 7:78–84, 1973.

[103] K. F. Canter, P. G. Coleman, Griffith. T. C., and G. R. Heyland. Measurement of total cross sections for low energy positron-helium collisions. (positron backscattering from metal surface). *J. Phys. B*, 5:L167, 1972.

[104] A. P. Mills Jr. and E. M. Gullikson. Solid neon moderator for producing slow positrons. *Applied Physics Letters*, 49:1121–1123, 1986.

[105] R. Khatri, M. Charlton, P. Sferlazzo, K. G. Lynn, A. P. Mills Jr., and L. O. Roellig. Improvement of rare-gas solid moderators by using conical geometry. *Applied Physics Letters*, 57:2374–2376, 1990.

[106] J. R. Danielson, D. H. E. Dubin, R. G. Greaves, and C. M. Surko. Plasma and trap-based techniques for science with positrons. *Rev. Mod. Phys.*, 87:247–306, Mar 2015.

[107] T. J. Murphy and C. M. Surko. Positron trapping in an electrostatic well by inelastic collisions with nitrogen molecules. *Phys. Rev. A*, 46:5696–5705, 1992.

[108] J. P. Marler and C. M. Surko. Positron-impact ionization, positronium formation, and electronic excitation cross sections for diatomic molecules. *Phys. Rev. A*, 72:062713, 2005.

[109] R. G. Greaves and C. M. Surko. Inward transport and compression of a positron plasma by a rotating electric field. *Phys. Rev. Lett.*, 85:1883–1886, Aug 2000.

[110] A. P. Mills Jr. and G. H. Bearman. Time bunching of slow positrons for annihilation lifetime and pulsed laser photon absorption experiments. *Applied physics*, 22:273–276, 1980.

[111] L. Liszkay, C. Corbel, P. Perez, P. Desgardin, M.-F. Barthe, T. Ohdaira, R. Suzuki, P. Crivelli, U. Gendotti, A. Rubbia, M. Etienne, and A. Walcarius. Positronium reemission yield from mesostructured silica films. *Applied Physics Letters*, 92:063114, 2008.

[112] A. F. Makhov. *Sov. Phys. Solid State 2*, 1934, 1960.

[113] A. P. Mills Jr. and R. J. Wilson. Transmission of 1 - 6-kev positrons through thin metal films. *Phys. Rev. A*, 26:490–500, Jul 1982.

[114] Y. Nagashima, Y. Morinaka, T. Kurihara, Y. Nagai, T. Hyodo, T. Shidara, and K. Nakahara. Origins of positronium emitted from SiO_2. *Phys. Rev. B*, 58:12676–12679, 1998.

[115] J. Greenwood. The correct and incorrect generation of a cosine distribution of scattered particles for Monte-Carlo modelling of vacuum systems. *Vacuum*, 67:217 – 222, 2002.

[116] Y. Nagashima, M. Kakimoto, T. Hyodo, K. Fujiwara, A. Ichimura, T. Chang, J. Deng, T. Akahane, T. Chiba, K. Suzuki, B. T. A. McKee, and A. T. Stewart.

Thermalization of free positronium atoms by collisions with silica-powder grains, aerogel grains, and gas molecules. *Phys. Rev. A*, 52:258–265, 1995.

[117] A. P. Mills Jr., E. D. Shaw, M. Leventhal, R. J. Chichester, and D. M. Zuckerman. Thermal desorption of cold positronium from oxygen-treated Al(111) surfaces. *Phys. Rev. B*, 44:5791–5799, Sep 1991.

[118] D. B. Cassidy, S. H. M. Deng, H. K. M. Tanaka, and A. P. Mills Jr. Single shot positron annihilation lifetime spectroscopy. *Applied Physics Letters*, 88:194105, 2006.

[119] A. A. Annenkov, M. V. Korzhik, and P. Lecoq. Lead tungstate scintillation material. *NIM A*, A490:30–50, 2002.

[120] R. Ley, K. D. Niebling, R. Schwarz, and G. Werth. Evidence from $n = 2$ fine structure transitions for the production of fast excited state positronium. 23:1915–1921, 1990.

[121] M. Horbatsch and E. A. Hessels. Shifts from a distant neighboring resonance. *Phys. Rev. A*, 82:052519, Nov 2010.

[122] U. Fano. Effects of configuration interaction on intensities and phase shifts. *Phys. Rev.*, 124:1866–1878, Dec 1961.

[123] U. Fano and J. W. Cooper. Line profiles in the far-uv absorption spectra of the rare gases. *Phys. Rev.*, 137:A1364–A1379, Mar 1965.

[124] Lebedev M.V. Misochko, O.V. Fano interference at the excitation of coherent phonons: Relation between the asymmetry parameter and the initial phase of coherent oscillations. *J. Exp. Theor. Phys.*, 120:651–663, 2015.

[125] A. Marsman, M. Horbatsch, and E. A. Hessels. The Effect of Quantum-Mechanical Interference on Precise Measurements of the $n = 2$ triplet P Fine Structure of Helium. *Journal of Physical and Chemical Reference Data*, 44:031207, 2015.

[126] T. Udem, L. Maisenbacher, A. Matveev, V. Andreev, A. Grinin, A. Beyer, N. Kolachevsky, R. Pohl, D. C. Yost, and T. W. Hänsch. Quantum Interference Line Shifts of Broad Dipole-Allowed Transitions. *Annalen der Pshysik*, 531:1900044, 2019.

[127] A. Marsman, M. Horbatsch, and E. A. Hessels. Shifts due to neighboring resonances for microwave measurements of the 2 ^3p fine structure of helium. *Phys. Rev. A*, 86:012510, 2012.

[128] http://qutip.org.

[129] G. Lindblad. On the generators of quantum dynamical semigroups. *Communications in Mathematical Physics*, 4(2):119–130, 1976.

[130] T. W. Darling, F. Rossi, G. I. Opat, and G. F. Moorhead. The fall of charged particles under gravity: A study of experimental problems. *Rev. Mod. Phys.*, 64:237–257, Jan 1992.

[131] A. Härter, A. Krükow, A. Brunner, and J. Hecker Denschlag. Long-term drifts of stray electric fields in a paul trap. *Applied Physics B*, 114(1-2):275–281, Nov 2014.

[132] A. Osterwalder and F. Merkt. Using High Rydberg States as Electric Field Sensors. *Phys. Rev. Lett.*, 82:1831–1834, 1999.

[133] S. D. Hogan, J. A. Agner, F. Merkt, T. Thiele, S. Filipp, and A. Wallraff. Driving Rydberg-Rydberg transitions from a coplanar microwave waveguide. *Phys. Rev. Lett.*, 108:063004, Feb 2012.

[134] A. Miyazaki, T. Yamazaki, T. Suehara, T. Namba, S. Asai, T. Kobayashi, H. Saito, Y. Tatematsu, I. Ogawa, and T. Idehara. First millimeter-wave spectroscopy of ground-state positronium. *PTEP*, 2015:011C01, 2015.

[135] T. R. Weber, J. R. Danielson, and C. M. Surko. Electrostatic beams from tailored plasmas in a Penning–Malmberg trap. *Physics of Plasmas*, 17:123507, 2010.

[136] A. P. Mills Jr. Brightness enhancement of slow positron beams. *Applied Physics*, 23:189–191, 1980.

[137] Atreju Tauschinsky, Rutger M. T. Thijssen, S. Whitlock, H. B. van Linden van den Heuvell, and R. J. C. Spreeuw. Spatially resolved excitation of Rydberg atoms and surface effects on an atom chip. *Phys. Rev. A*, 81:063411, Jun 2010.

[138] A. Deller and S. D. Hogan. Microwave spectroscopy of the $1snp^3p_J$ fine structure of high Rydberg states in ^{4}He. *Phys. Rev. A*, 97:012505, Jan 2018.

[139] T. Halfmann, J. Koensgen, and K. Bergmann. A source for a high-intensity pulsed beam of metastable helium atoms. *Measurement Science and Technology*, 11:1510–1514, sep 2000.

[140] R. Paulin, R. Ripon, and W. Brandt. Positron diffusion in metals. *Phys. Rev. Lett.*, 31:1214–1218, Nov 1973.

[141] R. Nieminen and M. Manninen. Positron surface states in metals. *Solid State Communications*, 15:403 – 406, 1974.

[142] K. F. Canter, A. P. Mills Jr., and S. Berko. Efficient positronium formation by slow positrons incident on solid targets. *Phys. Rev. Lett.*, 33:7–10, Jul 1974.

[143] A. P. Mills Jr. and L. Pfeiffer. Desorption of surface positrons: A source of free positronium at thermal velocities. *Phys. Rev. Lett.*, 43:1961–1964, Dec 1979.

[144] A. P. Mills Jr. Thermal activation measurement of positron binding energies at surfaces. *Solid State Communications*, 31:623 – 626, 1979.

[145] M. Haas, U. D. Jentschura, C. H. Keitel, N. Kolachevsky, M. Herrmann, P. Fendel, M. Fischer, Th. Udem, R. Holzwarth, T. W. Hänsch, M. O. Scully, and G. S. Agarwal. Two-photon excitation dynamics in bound two-body Coulomb systems including ac Stark shift and ionization. *Phys. Rev. A*, 73:052501, May 2006.

[146] R. C. Brown, S. Wu, J. V. Porto, C. J. Sansonetti, C. E. Simien, S.M. Brewer, J. N. Tan, and J. D. Gillaspy. Quantum interference and light polarization effects in unresolvable atomic lines: Application to a precise measurement of the ^{6,7}Li D_2 lines. *Phys. Rev. A*, 87:032504, Mar 2013.

[147] N. F. Ramsey. A new molecular beam resonance method. *Phys. Rev.*, 76:996–996, Oct 1949.

[148] N. F. Ramsey. Experiments with separated oscillatory fields and hydrogen masers. *Rev. Mod. Phys.*, 62:541–552, Jul 1990.

[149] A. C. Vutha and E. A. Hessels. Frequency-offset separated oscillatory fields. *Phys. Rev. A*, 92:052504, Nov 2015.

[150] K. Kato, T. D. G. Skinner, and E. A. Hessels. Ultrahigh-precision measurement of the $n = 2$ triplet p fine structure of atomic helium using Frequency-Offset Separated Oscillatory Fields. *Phys. Rev. Lett.*, 121:143002, Oct 2018.

[151] N. Bezginov, T. Valdez, M. Horbatsch, A. Marsman, A. C. Vutha, and E. A. Hessels. A measurement of the atomic hydrogen Lamb shift and the proton charge radius. *Science*, 365:1007–1012, 2019.